SNAP-THROUGH BUCKLING OF SHALLOW ARCHES WITH NONUNIFORM STIFFNESS UNDER DYNAMIC AND QUASI-STATIC LOADINGS

A THESIS

Presented to

The Faculty of the Division of Graduate

Studies and Research

By

Ira Hammes Rapp, III

In Partial Fulfillment

of the Requirements for the Degree

Doctor of Philosophy

in the School of Engineering Science and Mechanics

Georgia Institute of Technology

March, 1974

SNAP-THROUGH BUCKLING OF SHALLOW ARCHES

WITH NONUNIFORM STIFFNESS UNDER

DYNAMIC AND QUASI-STATIC LOADINGS

Approved:

G. J. Simitses, Chairman

C. V. Smith

W. W. King

Date approved by Chairman: 2/25/74

ACKNOWLEDGMENTS

The author wishes to express his sincere appreciation to Professor G. J. Simitses, his advisor, for his enthusiasm and for his encouragement, guidance and advice throughout the author's doctoral studies. He also wishes to thank him and Dr. M. E. Raville for encouragement and assistance in acquiring the John Hertz Fellowship which supported this interesting field of research. Thanks is also extended to Professors C. V. Smith, W. W. King, M. P. Stallybrass, and D. J. McGill, who served on the thesis committee, for their constructive comments and advice.

The author also wishes to thank Mrs. Jackie Van Hook for typing the dissertation.

Special permission was received from the Division of Graduate Studies and Research to vary the numbering of the thesis illustrations for clarity of presentation.

Finally, he wishes to thank his fiancee for her understanding and devotion.

TABLE OF CONTENTS

TABLE OF CONTENTS (Continued)

LIST OF TABLES

LIST OF TABLES (Continued)

LIST OF ILLUSTRATIONS

LIST OF ILLUSTRATIONS (Continued)

LIST OF ILLUSTRATIONS (Continued)

LIST OF ILLUSTRATIONS (Continued)

NOMENCLATURE

a	= variable parameter, adjusts inertia distribution
a_1	= symmetric mode generalized coordinate ($r_1 = a_1 + e$)
a_2	= antisymmetric mode generalized coordinate
$A(x)$	= non-uniform stiffness cross-sectional area
A_u	= uniform stiffness cross-sectional area
$\bar{A}$	= ratio of non-uniform to uniform cross-sectional areas
A_o	= minimum allowable cross-sectional area
$DR_{(MP)}$	= dynamic ratio of the quasi-static loading to the loading of constant magnitude and infinite duration for minimum possible critical loadings
$DR_{(MG)}$	= dynamic ratio of the quasi-static loading to the loading of constant magnitude and infinite duration for minimum guaranteed loadings
e	= initial rise parameter, maximum w_o
e_u	= initial rise parameter specifically for uniform geometry
e_{nu}	= initial rise parameter specifically excluding uniform geometry
E	= Young's modulus
I	= Hamilton's integral
I_1	= arch end moment of inertia
I_2	= arch center moment of inertia
$I(x)$	= non-uniform stiffness moment of inertia
I_u	= uniform stiffness moment of inertia
$\bar{I}$	= ratio of non-uniform inertia to uniform inertia
IMP	= impulse per unit mass

NOMENCLATURE (Continued)

L	= length between arch supports
$\tilde{L}$	= Lagrangian
M	= bending moment
m	= exponent which relates inertia to area $[I(x) = \alpha A^m(x)]$
n	= exponent which distributes inertia $[I(x) = I_1(x/a)^n]$
P_E	= Euler buckling load (simply supported)
$\bar{P}$	= nondimensional axial loading, $\bar{P} = (L/\rho)^2 Q/\pi^2 E A_u$
q	= transverse uniform loading
q_1	= transverse half-sine loading, maximum magnitude
q_{1_c}	= loading at which the critical kinetic energy is reached at the zero-loading saddle point, finite duration loading
q_{1_n}	= transverse half-sine loading for uniform geometry
q_1	= transverse half-sine loading for nonuniform geometry
Q_{nu}	= axial loading due to displacement from initial position, $Q = e - q_1$
$R(x)$	= radius of curvature
t	= time, dimensional
T	= kinetic energy
T_o	= non-dimensional critical time (finite duration)
u	= axial displacement
$\hat{u}$	= admissible axial displacement functions
U_{s_T}	= stretching energy
U_{b_T}	= bending energy
U_{p_T}	= potential of external forces
U_T	= total potential energy

NOMENCLATURE (Continued)

$\hat{U}_T$ = total potential energy functional for admissible displacement functions

$U_T^{(p)}$ = pth variation of the total potential, $p = 1,2,3,\ldots,\infty$

V_u = uniform stiffness volume

V_{nu} = non-uniform stiffness volume

$\bar{V}$ = nonuniform to uniform volume ratio

w = transverse position of the deflected reference line, measured from the x-axis

w_o = initial transverse arch position of the reference line, measured from the x-axis

$\hat{w}$ = admissible transverse reference line position functions

x = axial coordinate

α = constant which relates inertia to cross-sectional area $[I(x) = \alpha A^m(x)]$

ϵ = small positive parameter

ϵ_x = strain in the axial direction at any material point

ϵ_{x_o} = strain in the axial direction of positions on the reference line

ϵ_E = Euler strain

κ_x = curvature of the shallow arch

λ = augmented critical loading functional

λ_1 = Lagrange multiplier

ξ = nondimensional longitudinal coordinate ($\xi = \pi x/L$)

ρ = ratio of arch center to arch end moment of inertia $[\rho = I_2/I_1 = (L/2a + 1)^n]$

σ = mass per unit volume

σ_x = axial stress

NOMENCLATURE (Continued)

τ	= nondimensional time
$( )^*$	= dimensional quantity
$( )'$	= total derivative for quasi-static loadings
$( )_{,}$	= partial derivative for dynamic loadings
$(\dot{})$	= non-dimensional time derivative

SUMMARY

The problem of snap-through buckling of shallow arches with non-uniform stiffness under both quasi-static and dynamic loadings is investigated. Analyses of different stiffness distributions are performed to show the possible weight savings or increase in load carrying capability realized over the uniform geometry arch. In addition, conditions are determined to achieve a maximum load (snap-through) carrying capability design for an arch of specified volume, initial shape and length. No attempt is made to find the desired stiffness distribution.

For quasi-static loadings the geometries considered are the half-sine pinned arch with two symmetric stiffness distributions. The cross-sectional area-moment of inertia relation is $I = \alpha A^m$ where α is a positive constant and $m = 1, 2, 3$. The analysis, for the entire range of rise parameters, is accomplished through a Ritz-type technique and it includes both symmetric as well as antisymmetric snapping. Since closed form solutions for non-uniform geometries can only be achieved for axisymmetric behavior and specific stiffness distributions, such analyses are used to provide a confidence factor for the approximate technique.

A weight savings assessment is made by comparing the weight of the non-uniform geometry arch to that of uniform geometry provided that they both have the same critical load (equal strength). Maximum weight savings up to 20 per cent are observed for the $m = 3$ geometry

depending upon the value of the rise parameter. The maximum weight savings observed for m = 2 are of the order of four to five per cent. For m = 1, the uniform arch is generally the strongest.

For dynamic loadings one particular inertia distribution is used since it yields the best strength for quasi-static loadings. The following three cases of dynamic loadings are considered with a half-sine spatial distribution:

1) Loading of constant magnitude and infinite duration,

2) Ideal impulse (Dirac-delta),

3) Loading of constant magnitude and finite duration.

The method employed is one which relates critical conditions to characteristics of the total potential surface. Results are computed for a complete range of initial rise parameters and nonuniformity parameters. In general, m = 3 is the best configuration for all dynamic cases. A 30 per cent maximum increase in load carrying capability is realized for the load of constant magnitude and infinite duration and a 20 per cent increase for the ideal impulse. For small finite duration times the increase is well above that realized for the infinite duration time.

The optimization problem has as its objective the maximization of the critical load (snap-through) for a fixed volume of material. To obtain the critical load Trefftz' criterion is used, which is based on setting the first variation of the second variation of the total potential equal to zero.

The equilibrium equations together with that obtained from Trefftz' criterion yield the critical loading (objective function).

Next, the augmented functional is formed for the constant volume constraint and extremized with respect to the cross-sectional area yielding an integrodifferential equation. The solution is obtained by satisfying the equilibrium equations simultaneously with the optimality condition subject to the constant volume constraint.

CHAPTER I

INTRODUCTION

1.1 Motivation

Structural members of elastic materials have diversified uses as modern structural elements. The need for easier handling of industrial structural components, the advent of spaceflight and the development of synthetic materials which lend themselves to new fabrication processes enforce the need for new technology. Thus, the requirement of minimum weight for such structures is of paramount importance. The proper choice of material distribution yields the best design for minimum weight.

Thin walled isotropic and orthotropic shallow panels are of importance in the above class of structures. Such structural elements are often subjected to both quasi-static and dynamic lateral loadings. It is important to know how the stiffness of the structure affects the response to such loads. One such response is snap-through buckling or oil-canning. Many authors have either theoretically or experimentally investigated uniform shallow arches under both quasi-static and dynamic loadings. For quasi-static loadings snap-through buckling is characterized by a visible and sudden jump from the prebuckled configuration to another nonadjacent or far equilibrium configuration. Although the quasi-static analysis is sufficient to enable one to calculate buckling loads when the load is applied slowly, there are other

problems of interest, such as loads which are applied with constant magnitude and finite duration (step loadings). If the walls of the structural panel or arch are sufficiently thin, snap-through can occur when this member is everywhere elastic, although inelastic effects can arise after buckling. Furthermore, large lateral displacements of these structural elements may cause adverse effects on the performance of the overall configuration. The snap-through load is often the basic load for establishing design criteria.

1.2. Objective

In this investigation the problem of snap-through buckling of low arches with non-uniform stiffness under both quasi-static and dynamic loadings is considered. In addition, parametric studies are performed to show the possible weight savings realized over the uniform geometry arch. This is accomplished by comparing the weights of uniform and nonuniform stiffness geometries of equal strength. "Equal strength" means that the buckling load for the two geometries is the same provided that the length and the initial rise are equal.

Finally, given a low arch of specified volume and length, optimality conditions are determined which lead to optimum stiffness distribution for maximum strength.

The analysis of nonuniform stiffness shallow arches under both quasi-static and dynamic loads is accomplished through an approximate (Ritz-type) technique. Since closed form solutions for nonuniform geometries can only be achieved for axisymmetric behavior and specific stiffness distributions, such analyses are used to provide a confidence

factor for the approximate technique. Also, exact solutions are available for a half-sine pinned low arch of uniform geometry under a half-sine spatial distribution of the load for both quasi-static and dynamic application. These solutions, through comparison, provide a check to the approximate solution.

The complete analysis, including comparisons, is presented through the following three tasks. The first task is to obtain a closed form solution to the pinned low arch loaded quasi-statically with a uniformly distributed transverse loading. The cross-sectional moment of inertia is taken to be $I(x) = I_1(x/a)^2$ as shown in Figure 2.1. The initial shape of the arch is taken to be parabolic. This task is presented in chapter two. The second task begins with an approximate solution to the above problem, assuming a two mode response. These two modes are taken to be symmetric and anti-symmetric with respect to the plane of structural symmetry. By comparing these results to those of task one a degree of confidence is established in the accuracy of the approximate solution. Included in the second task, the approximate solution is used to generate results for the following problems: Low half-sine pinned arches, with half-sine quasi-static loadings, and two different stiffness distributions, $I(x) = I_1\left(\frac{x}{a}\right)^2$ and $I(x) = I_1\left(\frac{x}{a}\right)^{1/2}$. Correlation of critical loadings for the different inertia cases and the constant volume condition is considered as a preliminary step towards optimization of low arches.

Finally, in task three (Chapter IV) the approximate technique is used to generate results for the low half-sine pinned arch, with $I(x) = I_1\left(\frac{x}{a}\right)^2$, under specified dynamic loadings applied with half-sine

spatial distributions. These dynamic loadings are the loading of constant magnitude and infinite duration, the ideal impulse and the loading of constant magnitude and finite duration. The first two dynamic cases can be thought of as idealizations of the following two categories of "blast" loadings, respectively:

1) "Blasts" of low decay rates and high decay times.

2) "Blasts" of high decay rates and low decay times.

In all three tasks the moment of inertia is related to the cross-sectional area by $I(x) = \alpha A^m(x)$ where α is an appropriate constant and m is taken to be one, two or three.

1.3. Historical Review

The analysis of shallow arches with uniform geometry has long been a problem of interest to many investigators. The design of rings and high arches with nonuniform stiffness has more recently received attention stemming from investigations of the optimum column. Following is a chronological list and brief discussion on relevant works.

Both quasi-static and dynamic loading applications of uniform shallow arches have been studied by various methods. The significance of snap-through buckling, in so far as it illustrates certain important features in more complicated buckling problems of plates and shells, was pointed out by Marguerre[1], who constructed a simplified mechanical model to demonstrate these features. Timoshenko[2] obtained an approximate solution to the problem of a low arch under a uniformly distributed load. Biezeno[3] considered the problem of a low circular

arch loaded laterally at the midpoint with a concentrated load. Kaplan and Fung[4] investigated the problem of pinned low arches of various initial shapes and spatial distributions of the lateral load. Their results show that a very shallow arch snaps through symmetrically, whereas a higher arch buckles asymmetrically. They also ran a limited number of experimental tests, and their data is in good agreement with their theoretical predictions. In 1962, Gjelsvik and Bodner[5] obtained an approximate solution to the problem of a shallow arch with a concentrated load at the midpoint of the arch and clamped boundaries. They also reported experimental results, and they showed good agreement between their experimental data and theoretical results. In 1965, Simitses[6] obtained solutions to the pinned and clamped low arch under a half-sine loading with an initial half-sine shape. Antisymmetric as well as symmetric modes of deformation were considered. The arch was shown to buckle antisymmetrically for sufficiently high initial rise parameters. Critical loads were calculated for a complete range of initial rise parameters. In 1966, Schreyer and Masur[7] obtained an exact solution to the problem of a clamped low circular arch under uniform pressure and concentrated load at the midpoint. Contrary to the results of Ref. [6], they showed that for the concentrated load case the arch snaps symmetrically regardless of the value of the initial rise parameter. In 1971, Dickie and Broughton[8] considered a more complete class of these problems. They concerned themselves with both symmetric and asymmetric buckling of low arches subject to radial transverse loadings

and possessing either pinned ends, clamped ends or a combination of both. The type of loadings considered were both center point, uniform radial, and linearly varying radial. Approximate series solutions were compared with experimental values.

The problem of snap-through buckling of low arches with uniform stiffness under dynamic loads has been treated by many investigators. Some relevant references are the works of Hsu, Kuo, and Lee[9], and Hoff and Bruce[10]. More recent works are those of Simitses[6], Lock[11], and Fulton and Barton[12]. In 1965, Ref. [6] followed an energy surface approach to determine critical loadings as does Ref. [10]; however, Ref. [11] and Ref. [12] use a different criterion for buckling. Lock[11] numerically integrated the equations of motion to determine stability criteria. In 1971, Fulton and Barton[12] investigated the same arch by a finite difference approach. Stability criteria for Ref. [11] and Ref. [12] consisted of examining peak values of the average displacement. The value of the load at which this peak displacement exhibited a sudden increase for a very small increase in loading was defined as the dynamic buckling load. Results for the symmetric mode were compared to that of Ref. [10]. The critical ideal impulse values were considerably lower than those of Ref. [10]. Antisymmetric mode results were plotted and correlated well with those of Ref. [11]; however, they yielded questionable "gaps in the dynamic buckling strength" as stated by Fulton and Barton[12]. Both Ref. [10] and Ref. [6] show higher critical values which increase monotonically with the initial rise parameter.

The study of structures for minimum weight started with Lagrange around 1770 when he arrived at an erroneous result. He determined that the strongest column should be one of constant circular cross-section. The correct result was achieved by Clausen et al.[13] in 1851 for simply supported columns with similar cross-sections. If the moment of inertia, I, and the area, A, are related by $I = \alpha A^m$, then similar sections are associated with $m = 2$. He determined that the best shaped column had a volume of $\sqrt{3}/2$ times the volume of the uniform cylindrical column of the same load carrying capability. This problem was generalized and completely solved by Keller[14] who determined that, of all simply-supported columns with convex and similar cross-sections, "the strongest column has an equilateral triangle as its cross-section and is tapered along its length, being thickest in the middle and thinnest at its ends. Its buckling load is 61.2 percent larger than that of a circular cylinder ... For a uniform column triangularizing was shown to increase the buckling load by 20.9 percent over that of a circular cylinder." This was further generalized by Tadjbakhsh and Keller[15] to four types of boundary conditions. Keller and Niordson[16] treated the problem of finding the height of the tallest column under its own weight. Taylor[17] recognized that the optimality relation between shape and displacement obtained by Tadjbakhsh and Keller[15] could be obtained directly by minimizing the potential energy of the system with a volume constraint superposed. Salinas[18] determined a general class of problems for which this procedure applied. Prager and Taylor[19] provided an exact solution for a simply-supported column for m equals

one. Closed form solutions for m equals three and a finite element displacement solution for m equals one, two and three for the column with elastic restraints have been obtained by Simitses et al.[20]. Treatment of the corresponding problem of determining that shape of a high circular arch which has the largest critical buckling pressure of all high circular arches of given radius, central angle, and volume has been performed by Wu[21]. Wu allowed only inextensional deformation for m equals three. The optimality condition was found to be the same as for a column with m equals three. Following this work, Budiansky et al.[22] have studied a class of such problems to include uniform radial loading and dead pressure loading or loadings which are constrained to remain parallel to their initial directions of application. Finally, a review of such works is discussed by Niordson and Pederson[23], Wasiutynski and Brandt[24], and Sheu and Prager[25].

CHAPTER II

QUASI-STATIC CLOSED FORM SOLUTION

2.1 Introduction

The shallow arch is an important member of a class of structures used in industry. It is advantageous in many cases to minimize the weight of such a structure. In order to find a least weight structure it is important to choose a method which leads to accurate results with a minimum of effort and time. To establish the validity of an approximate solution a degree of confidence must be confirmed by considering a closed form solution if possible. Ref. [3] outlines a procedure for a low arch with uniform geometry under a center point loading. The same method is used herein to determine critical uniform loadings for the symmetric shallow arch with the specified non-uniform stiffness $I(x) = I_1(x/a)^2$. Note that this expression is valid for $a \leq x \leq a + \frac{L}{2}$. The arch is initially parabolic, uniformly loaded and has simply supported ends as shown in Figure 2.1. The results obtained are compared to those of the approximate procedure in order to establish the degree of confidence.

2.2 Assumptions

The following assumptions apply to all subsequent quasi-static investigations:

a) The linearly elastic material of the shallow arch is homogeneous and isotropic.

b) The slope is everywhere small (shallowness), $\left(\frac{dw_o}{dx}\right)^2 \ll 1$.

c) The arch is thin. The thickness is much smaller than the typical arch dimension L, i.e. $h \ll L$.

d) Cross-sectional planes before deformation remain plane and normal to the deformed axis of the low arch after deformation.

e) The rate of load application is so small that it does not induce any appreciable dynamic effects in the response of the structure (static analysis).

f) The cross-section of the low arch possesses a plane of symmetry, and the loading is restricted to this plane. The possibility of lateral deflection is ignored.

g) The cross-sectional moment of inertia, $I(x)$, is related to the cross-sectional area, $A(x)$, by the relation $I(x) = \alpha A^m(x)$. In principle, m can have all positive values, thereby exhibiting a host of possible geometries. Results are only computed for m equals one, two and three which, for example, characterize a variable base and fixed height, variable base and height, and variable height and fixed base, respectively.

2.3 General Method of Approach

Equilibrium equations for the quasi-statically loaded arch with an initial parabolic shape are written on the deformed structure. From linear constitutive equations and nonlinear kinematic relations, due to finite rotations, the axial loading is related to deformations.

The transverse equilibrium equation is solved by introducing an exponential substitution to achieve the homogeneous solution and assuming a quadratic polynomial to acquire the particular solution for the axisymmetric behavior of the arch. The transverse and in-plane equilibrium equations are reduced to a single nonlinear inhomogeneous quadratic equation in the transverse loading as a function of the axial loading, initial rise parameter, and the structural geometry. From a plot of transverse loading versus axial loading, the transverse loading at which there is no increase for a small increase in the axial loading is defined as the critical snap-through loading. When the axial loading, corresponding to the critical transverse loading, reaches that of the 2nd buckling loading of a beam as a straight strut, then this is the lower bound of purely antisymmetric buckling since the strain energy of stretching for the curved member is shown to be equal to the strain energy of stretching for the member as a straight strut at this loading. The second buckling load can only be determined for uniform geometry. This lower bound corresponds to a particular initial rise parameter, e. The upper limit on e, for which the axisymmetric behavior is applicable, is estimated from the known value for uniform geometry. For rises less than this particular quantity buckling occurs at the limit point. An outline for the above procedure is described in Ref. [3] for a uniform geometry arch loaded by a center point loading.

2.4 Development of the Governing Relations

Let w_o and w denote the initial undeformed and deformed

configuration for the reference line of the low arch, respectively. Also, u represents the horizontal displacement of any point of the reference line. See Figure 2.1 for geometry and sign convention. Considering the above assumptions and notation one obtains the following kinematic relation which is nonlinear due to finite rotations:[27]

$$\epsilon_o = \frac{du}{dx} + \frac{1}{2}\left[\left(\frac{dw}{dx}\right)^2 - \left(\frac{dw_o}{dx}\right)^2\right] \tag{1}$$

Due to Assumption (b)

$$\epsilon = \epsilon_o + z\kappa_x \tag{2}$$

where ϵ_o is the reference line strain and z is the distance from the reference line. κ_x is the change in curvature of the reference line given by

$$\kappa_x = \frac{d^2w_o}{dx^2} - \frac{d^2w}{dx^2} \tag{3}$$

Denoting by Q and M the resultant axial force and resultant bending moment, respectively

$$Q^* = -\int_A \sigma_x \, dA$$

$$M = \int_A z\sigma_x \, dA$$

Use of Assumption (a) and Equation 2 yields

$$Q = -EA(x)\epsilon_o \tag{4}$$

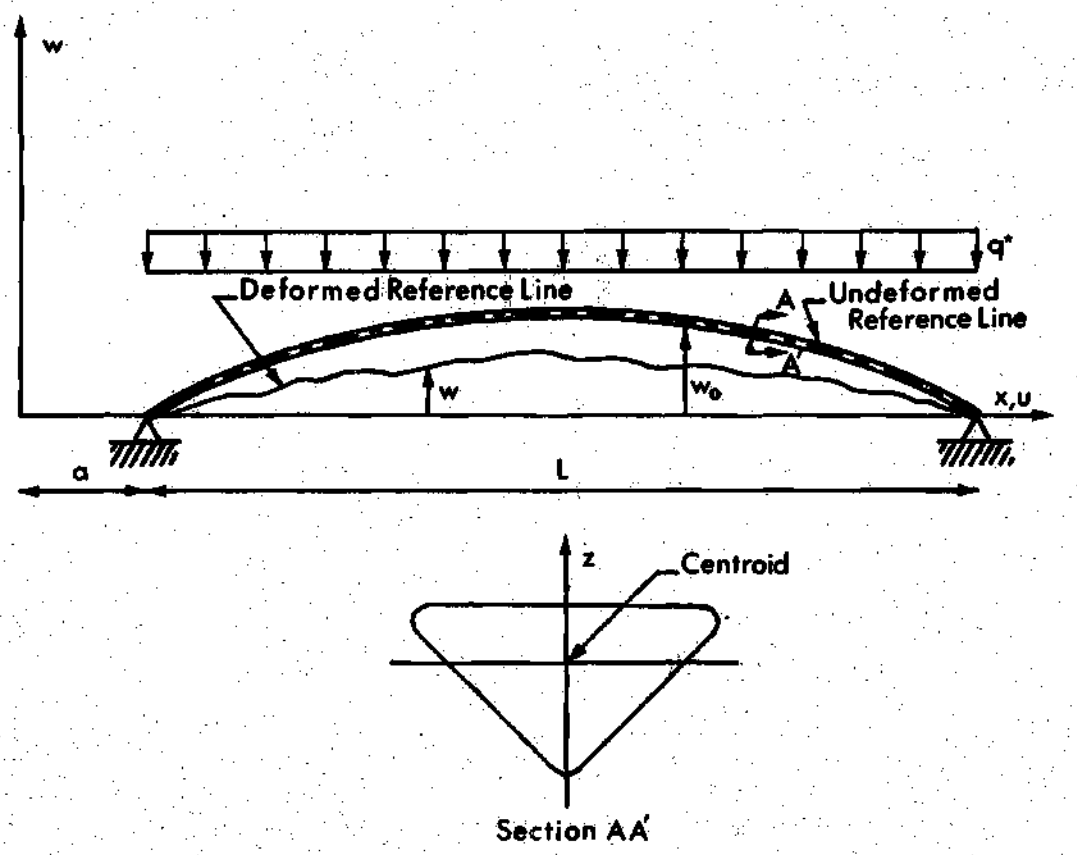

Figure 2.1. Geometry and Sign Convention for the Low Arch.

and

$$M = EI(x)\kappa_x \tag{5}$$

The equilibrium equations and proper boundary conditions for symmetric behavior are

$$\frac{d^2w}{dx^2} - \frac{d^2w_o}{dx^2} + \frac{Q^*w}{EI(x)} = q^* \frac{L(x-a)}{2EI(x)} - q^* \frac{(x-a)^2}{2EI(x)} \tag{6a}$$

$$\frac{dQ^*}{dx} = 0 \tag{6b}$$

$$w(a) = \frac{dw}{dx}\left(a+\frac{L}{2}\right) = 0 \tag{7}$$

Note that, because of the restriction of axisymmetric behavior, the domain of applicability of the governing equation is $a \le x \le a + \frac{L}{2}$. Consideration of the kinematic equation, Equation 1, integration of Equation 4 over the length between arch supports, use of the fact that the ends are immovable and the behavior is symmetric yields

$$\frac{2Q^*}{E}\int_a^{a+\frac{L}{2}} \frac{dx}{A(x)} + \int_a^{a+\frac{L}{2}} \left[\left(\frac{dw}{dx}\right)^2 - \left(\frac{dw_o}{dx}\right)^2\right]dx = 0 \tag{8}$$

2.5 Solution

The initial shape of the nonuniform arch is (see Figure 2.1)

$$w_o(x) = (4e^*/L^2)[x(2a+L-x) - a(a+L)] \tag{9}$$

where

$$e^* = w_{o_{max}} \quad . \tag{10}$$

With $I(x) = I_1(x/a)^2$ the governing differential equation, Equation 6a, becomes one with variable coefficients.

$$EI_1(x^2/a^2)\frac{d^2w}{dx^2} + Q^*w = q^*\frac{L(x-a)}{2} - \frac{q^*(x-a)^2}{2} - \frac{8e^*EI_1x^2}{a^2L^2} \tag{11}$$

The homogeneous equation can be reduced to

$$\frac{d^2w}{dz^2} - \frac{dw}{dz} + \frac{Q^*a^2}{EI_1}w = 0 \tag{12}$$

with constant coefficients by the exponential substitution $x/a = e^z$. The solution to Equation 12 (See Ref. [28]) is

$$w_c = \sqrt{e^z}\,(A \sin \beta z + B \cos \beta z) \quad . \tag{13}$$

The particular solution to Equation 11 is given by

$$w_p(x) = Cx^2 + Dx + F \tag{14}$$

where the constants C, D and F are

$$C = -(16EI_1e^* + a^2L^2q^*)/(2 + k^2)(2EI_1L^2)$$

$$D = a^2q^*(L + 2a)/2EI_1k^2$$

$$F = -a^3q^*(a + L)/2EI_1k^2$$

and $$k^2 = Q^* a^2 / EI_1$$

$$\beta = \sqrt{\left(k^2 - \frac{1}{4}\right)} .$$

The general solution, which is the sum of the particular and complementary solutions, involves two constants, A and B [see Equation (13)]. These constants are evaluated from the boundary conditions, Equations 7. These constants are:

$$A = \left\{-[C(2a + L) + D][2a(2a + L)]^{1/2} + [(a/kL)^2(8e^* + 2CL^2)]\left[2\beta \sin\left(\beta \ln \frac{2a+L}{2a}\right) - \cos\left(\beta \ln \frac{2a+L}{2a}\right)\right]\right\} \Big/ \left[\sin\left(\beta \ln \frac{2a+L}{2a}\right) + 2\beta\left(\cos \beta \ln \frac{2a+L}{2a}\right)\right]$$

$$B = a^2(8e^* k^2 EI_1 - q^* a^2 L^2)/(2 + k^2)(k^2 L^2 EI_1)$$

If the solution is substituted into Equation 8, then a nonlinear expression is obtained which relates q* and Q*.

From this equation one obtains a plot of transverse loading versus axial loading for any geometry desired. As an example see Figure 2.2 and Figure 2.3 for uniform geometry. Figure 2.2 represents curves for initial rise parameters ranging from no snapping to the upper bound for axisymmetric snap-through. The curves of Figure 2.3 represent solely axisymmetric buckling which is not the actual buckling mode realized for this range of initial rise parameters. Hence, the closed form solution is not applicable for this range. One similar curve is shown in Ref. [3] for the pinned arch under a center point

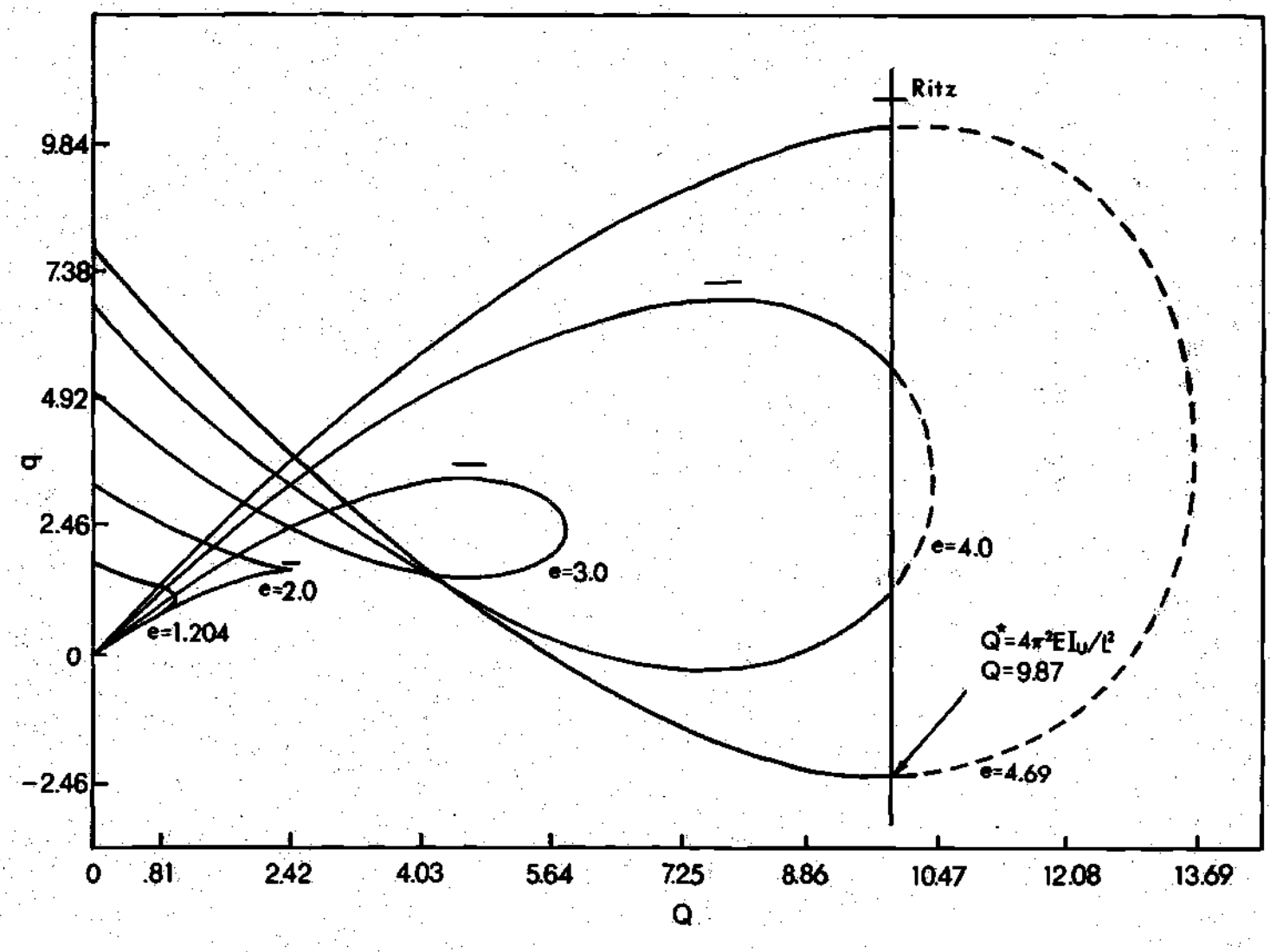

Figure 2.2 Nondimensional Transverse Loading versus Axial Loading.

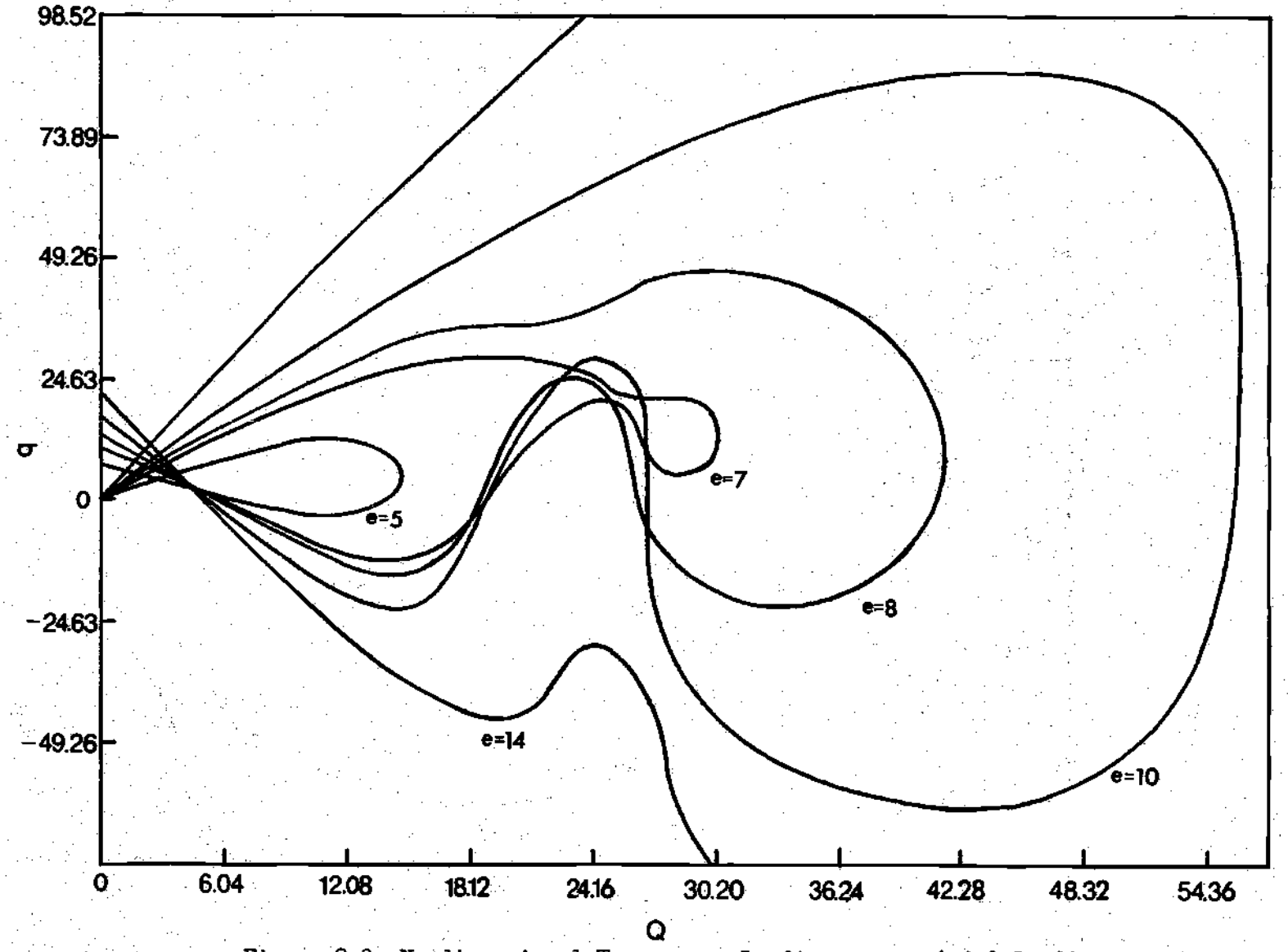

Figure 2.3 Nondimensional Transverse Loading versus Axial Loading.

loading. Critical loadings versus initial rise parameters for non-uniform stiffness and constant volume are plotted in Figure 2.4 through Figure 2.6. Exact values are given in Table 3.1 through Table 3.3. Note that critical loadings and initial rise parameters are given in a nondimensionalized form. The nondimensionalized parameters q and e are given by

$$q = q^*\rho_o/EA_u\epsilon_E^2 \ , \ Q = Q^*8L^2/4EI_u \quad \text{and} \quad e = e^*/\rho_o$$

where

$$\rho_o^2 = I_u/A_u,$$

A_u and I_u are the area and moment of inertia of the uniform geometry, ϵ_E is the Euler strain $(\pi\rho_o/L)^2$ and E is Young's modulus. Critical loadings are compared considering constant volume for each geometry. The constant volume condition becomes

$$\bar{V} = \frac{V_{nu}}{V_u} = \frac{V_{nu}}{\left(\frac{I_u}{\alpha}\right)^{\frac{1}{m}} L} = 1 \qquad (15)$$

where

$$V_u = A_u\, L$$

$$V_{nu} = \int_a^{\left(a + \frac{L}{2}\right)} A(x)dx$$

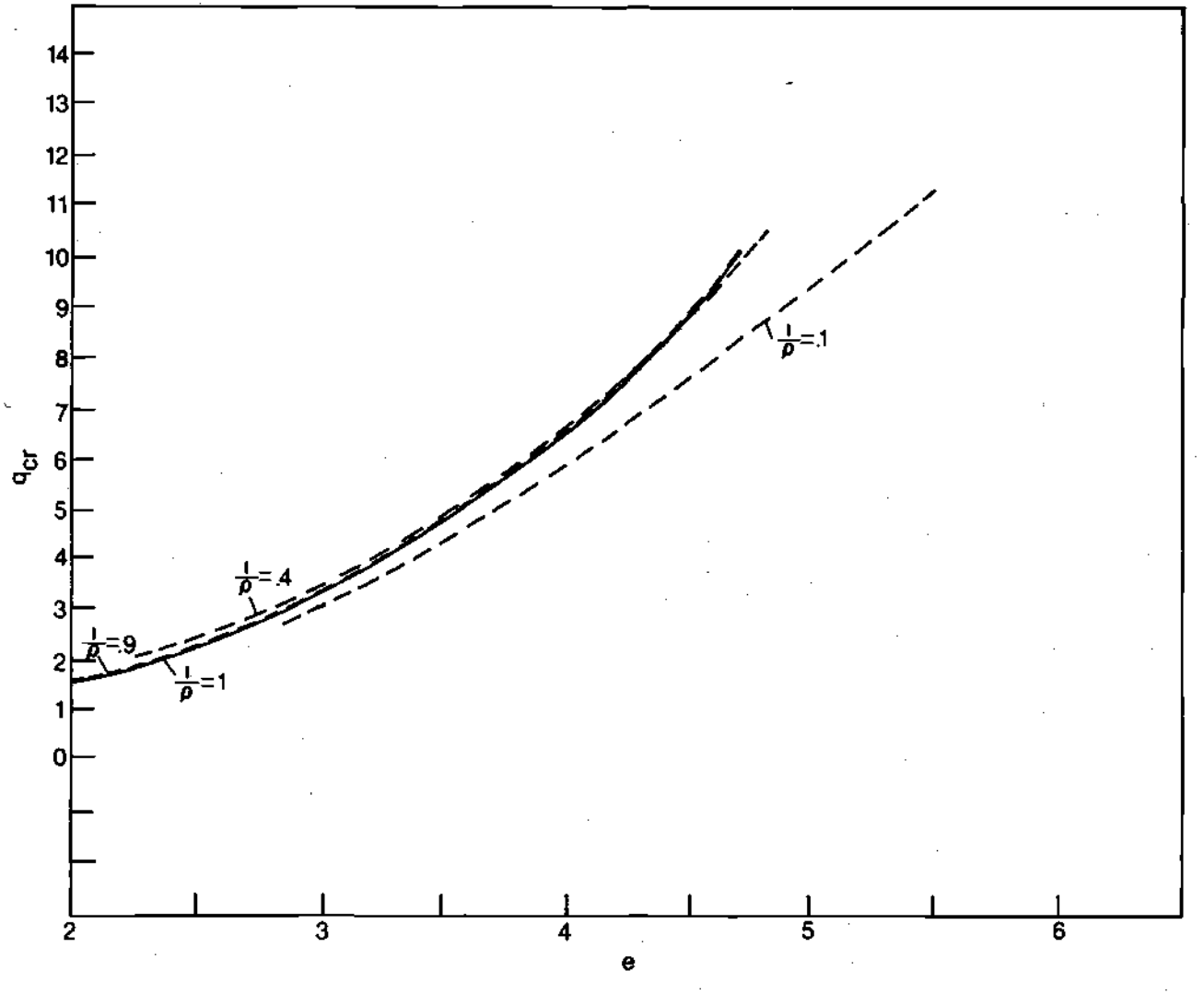

Figure 2.4 Nondimensional Critical Loading versus Initial Rise Parameters, m=1, n=2.

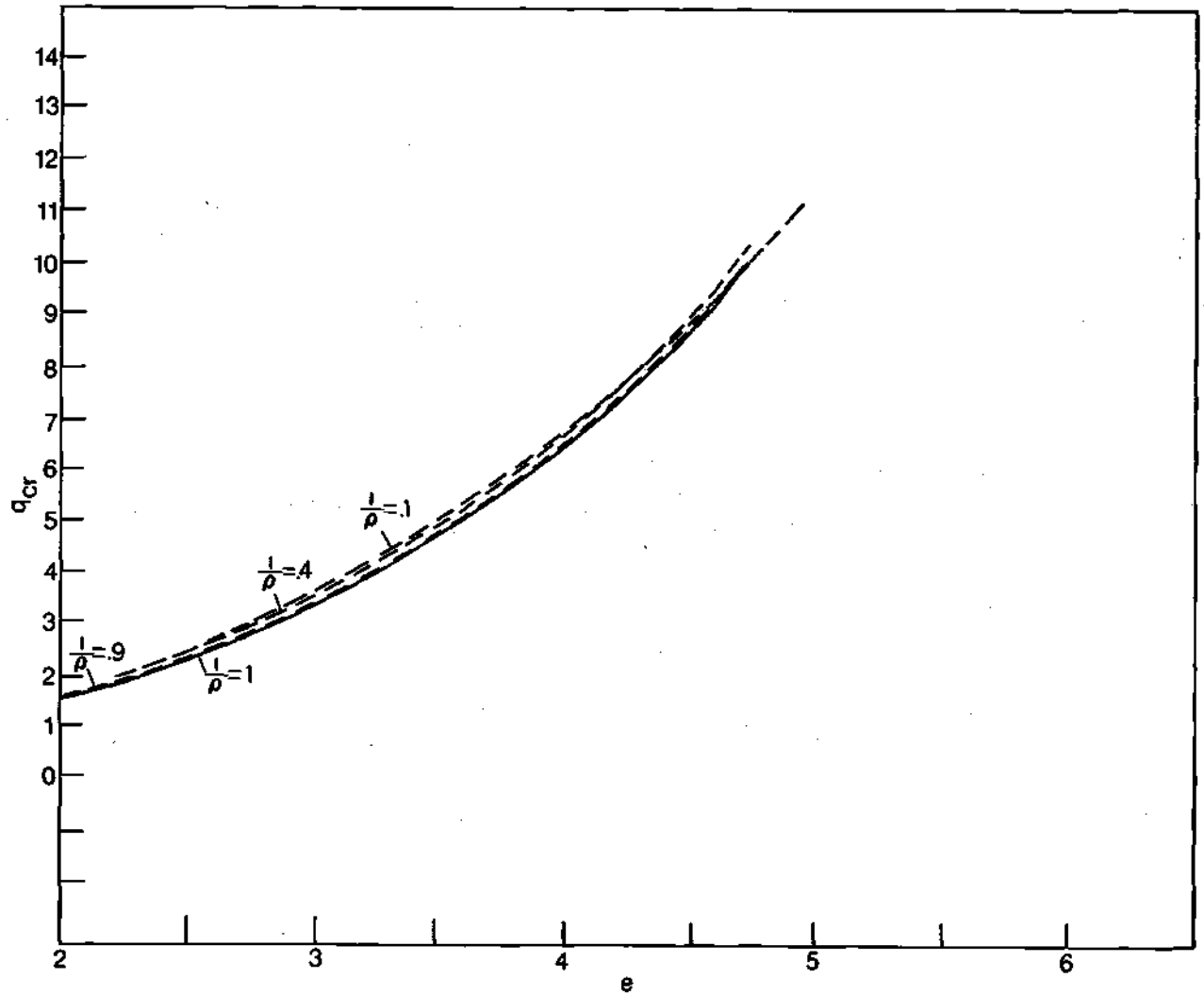

Figure 2.5 Nondimensional Critical Loading versus Initial Rise Parameters, m=2, n=2.

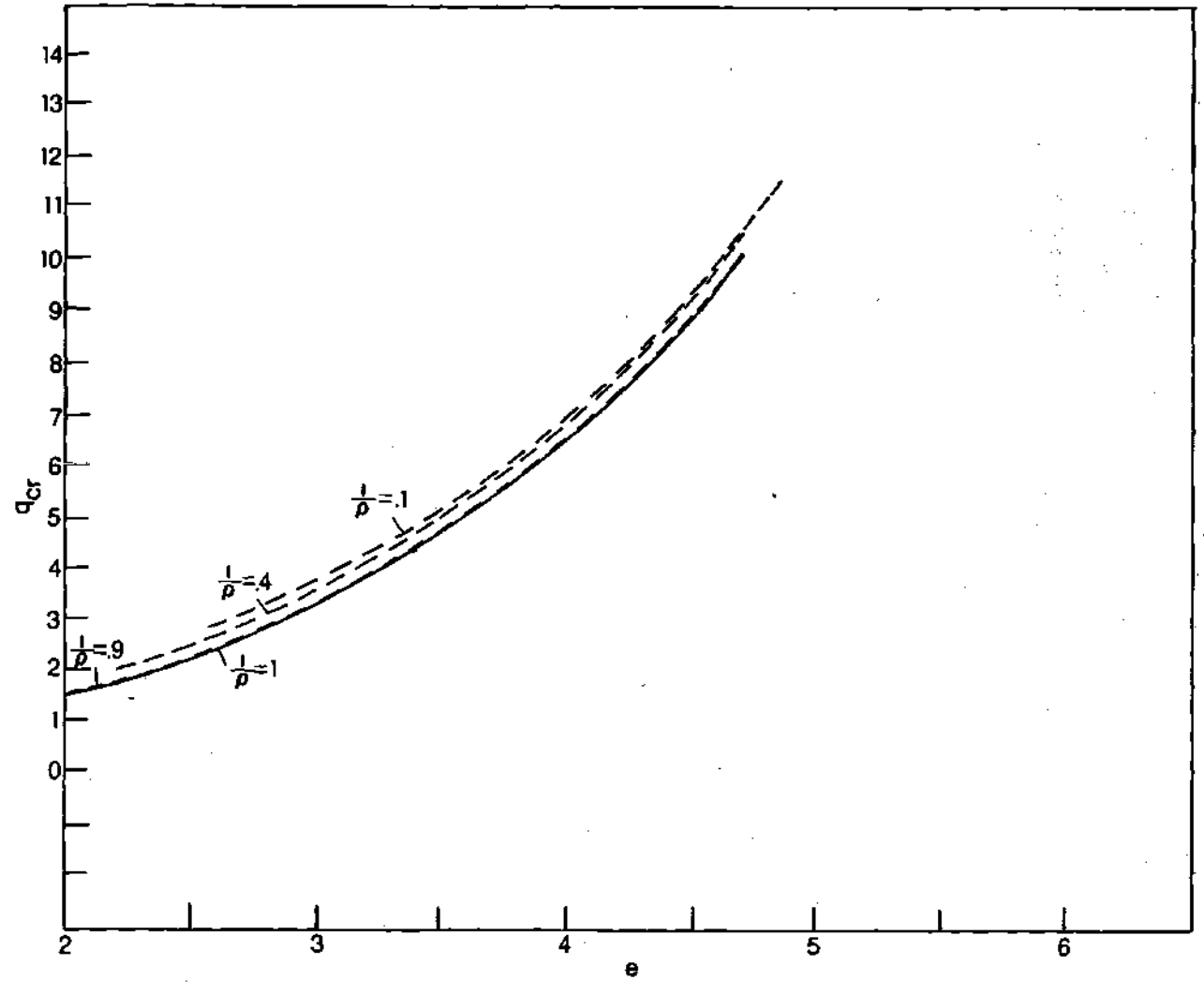

Figure 2.6 Nondimensional Critical Loading versus Initial Rise Parameters, m=3, n=2.

where

$$A(x) = \left[(I_1/\alpha)\left(\frac{x}{a}\right)^n\right]^{1/m}$$

Thus, one obtains

$$V_{nu} = \left(\frac{I_1}{\alpha}\right)^{\frac{1}{m}}\left[L/\left(1 + \frac{n}{m}\right)\right]\left[\left(\rho^{\frac{m+n}{mn}} - 1\right)/\left(\rho^{1/n} - 1\right)\right]$$

and

$$I_u = \frac{I_1\left(\rho^{\frac{m+n}{mn}} - 1\right)^m}{\left(1 + \frac{n}{m}\right)^m\left(\rho^{\frac{1}{n}} - 1\right)^m}$$

where $\rho = I_2/I_1$, I_1 and I_2 are the cross-sectional inertias at $x=a$ and $x = a + \frac{L}{2}$; respectively.

For $n=2$ one obtains

$$V_{nu} = I_1 L(\rho^{3/2} - 1)/3\alpha(\rho^{1/2} - 1) \qquad m = 1$$

$$V_{nu} = I_1^{1/2} L(\rho^{1/2} + 1)/2\alpha^{1/2} \qquad m = 2$$

$$V_{nu} = 3I_1^{1/3} L(\rho^{5/6} - 1)/5\alpha^{1/3}(\rho^{1/2} - 1) \qquad m = 3$$

and

$$I_u = I_1(\rho^{3/2} - 1)/3(\rho^{1/2} - 1) = \alpha A_u \qquad m = 1$$

$$I_u = I_1(\rho^{1/2} + 1)^2/4 = \alpha A_u^2 \qquad m = 2$$

$$I_u = 27I_1(\rho^{5/6} - 1)^3/125(\rho^{1/2} - 1)^3 = \alpha A_u^3 \qquad m = 3$$

Nondimensionalization is now possible for all nonuniform geometries considered.

Substitution of the above solution into the expression for the axial loading, Equation 8, and integration over the length yields the following nondimensional quadratic equation in the transverse loading where the A_i's are functions of the axial loading and structural geometry.

$$A_1 q^2 + A_2 q + A_3 = 0 \tag{16}$$

The A_i's are given by

$$\frac{A_1}{\pi^8 f^2} = \{[\sin(2\beta \ell n\gamma)](\rho^{\frac{1}{2}}-1)/4\beta\}\{(2k^2-1)\Gamma^2 + \beta\chi/[4(\rho^{\frac{1}{2}}-1)^4]$$

$$+ (1-2k^2)/[2^8(\rho^{\frac{1}{2}}-1)^8\theta]\} + k^2(\rho^{\frac{1}{2}}-1)\ell n\gamma[\Gamma^2 + 1/2^8(\rho^{\frac{1}{2}}-1)^8\theta]$$

$$+ \{[1 - \cos(2\beta \ell n\gamma)](\rho^{\frac{1}{2}}-1)/2\beta\}\{\beta\Gamma^2 - [\beta/2^8(\rho^{\frac{1}{2}}-1)^8\theta]$$

$$+ (1-2k^2)\chi/16(\rho^{\frac{1}{2}}-1)^4\} + \{\rho^{\frac{1}{2}}/[4(\rho^{\frac{1}{2}}-1)^3]\}$$

$$\cdot \{-\gamma^{\frac{1}{2}}[\cos(\beta \ell n\gamma)/16(\rho^{\frac{1}{2}}-1)^4k^2(2+k^2) + \Gamma \sin(\beta \ell n\gamma)]$$

$$+ 1/[16(\rho^{\frac{1}{2}}-1)^4k^2(2+k^2)]\} + \{\beta/[8(\rho^{\frac{1}{2}}-1)^3(2+k^2)^2]\}\{\gamma^{3/2}[[(2\Gamma$$

$$+ [(1+2k^2)/16(\rho^{\frac{1}{2}}-1)^4k^2\beta(2+k^2)]\cos(\beta \ell n\gamma) + \left((1+2k^2)\Gamma/\beta\right.$$

$$\left. - 1/8(\rho^{\frac{1}{2}}-1)^4k^2(2+k^2)\right)\sin(\beta \ell n\gamma)] - 2\Gamma$$

$$- (1+2k^2)/16(\rho^{\frac{1}{2}}-1)^4k^2\beta(2+k^2)\} + \rho/[128(\rho^{\frac{1}{2}}-1)^6k^2]$$

$$+ (\rho+\rho^{\frac{1}{2}}+1)/[(16)(24)(\rho^{\frac{1}{2}}-1)^6(2+k^2)^2]$$

$$- \rho^{\frac{1}{2}}(\rho^{\frac{1}{2}}+1)/[(16)(8)(\rho^{\frac{1}{2}}-1)^6k^2(2+k^2)]$$

$$\frac{A_2}{\pi^4 \text{eff}_1} = \{8(\rho^{\frac{1}{2}}-1)^3k^2\sin(2\beta\ell n\gamma)/\beta\}\{2(1-2k^2)\Gamma^2 - [\beta\chi/2(\rho^{\frac{1}{2}}-1)^4]$$

$$+ (2k^2-1)/[2^7(\rho^{\frac{1}{2}}-1)^8\theta]\} - [64k^2(\rho^{\frac{1}{2}}-1)^3\ell n\gamma]\{\Gamma^2$$

$$+ 1/[2^8(\rho^{\frac{1}{2}}-1)^8\theta]\} - \{32(\rho^{\frac{1}{2}}-1)^3k^2[1 - \cos(2\beta\ell n\gamma)]/\beta\}\{\beta\Gamma^2$$

$$- \beta/[2^8(\rho^{\frac{1}{2}}-1)^8\theta] + (1-2k^2)\chi/[16(\rho^{\frac{1}{2}}-1)^4]\}$$

$$+ [8\rho^{\frac{1}{2}}/(\rho^{\frac{1}{2}}-1)]\{\gamma^{\frac{1}{2}}[\cos(\beta\ell n\gamma)/16k^2(\rho^{\frac{1}{2}}-1)^4(2+k^2)$$

$$+ \Gamma\sin(\beta\ell n\gamma)] - 1/[16(\rho^{\frac{1}{2}}-1)^4k^2(k^2+2)]\}$$

$$- [4k^2\beta/(\rho^{\frac{1}{2}}-1)(2+k^2)^2]\Big\{\gamma^{3/2}\Big[\Big(2\Gamma$$

$$+ (1+2k^2)/16(\rho^{\frac{1}{2}}-1)^4k^2\beta(2+k^2)\Big)\cos(\beta\ell n\gamma)$$

$$+ \Big((1+2k^2)\Gamma/\beta - 1/[8k^2(\rho^{\frac{1}{2}}-1)^4(2+k^2)\Big)\sin(\beta\ell n\gamma)\Big] - 2\Gamma$$

$$- (1+2k^2)/[16(\rho^{\frac{1}{2}}-1)^4k^2\beta(2+k^2)]\Big\} - \{8\beta/(\rho^{\frac{1}{2}}-1)(2+k^2)^2\}$$

$$\cdot \Big\{\gamma^{3/2}\Big[-\Big(2\Gamma + (1+2k^2)/16(\rho^{\frac{1}{2}}-1)^4k^2\beta(2+k^2)\Big)\cos(\beta\ell n\gamma)$$

$$+ \Big(1/[8(\rho^{\frac{1}{2}}-1)^4k^2(2+k^2)] - (1+2k^2)\Gamma/\beta\Big)\sin(\beta\ell n\gamma)\Big]$$

$$+ 2\Gamma + (1+2k^2)/16(\rho^{\frac{1}{2}}-1)^4k^2\beta(2+k^2)\Big\}$$

$$+ (\rho+\rho^{\frac{1}{2}}+1)/[3(\rho^{\frac{1}{2}}-1)^4(2+k^2)^2] - \rho^{\frac{1}{2}}(\rho^{\frac{1}{2}}+1)/[2(\rho^{\frac{1}{2}}-1)^4k^2(2+k^2)]$$

$$\frac{A_3}{f_1^2 e^2} = [2^8 k^4 (\rho^{\frac{1}{2}}-1)^5 \sin(2\beta \ell n\gamma)/\beta]\{(2k^2-1)\Gamma^2 + \beta\chi/4(\rho^{\frac{1}{2}}-1)^4$$

$$+ (1-2k^2)/2^8(\rho^{\frac{1}{2}}-1)^8\theta\}$$

$$+ [(32)(\rho^{\frac{1}{2}}-1)^5 2^5 k^6 \ell n\gamma][\Gamma^2 + 1/2^8(\rho^{\frac{1}{2}}-1)^8\theta]$$

$$+ \{2^9(\rho^{\frac{1}{2}}-1)^5 k^4[1 - \cos(2\beta \ell n\gamma)]/\beta\}\{\beta\Gamma^2 - \beta/2^8(\rho^{\frac{1}{2}}-1)^8\theta$$

$$+ (1-2k^2)\chi/2^4(\rho^{\frac{1}{2}}-1)^4\} + [256(\rho^{\frac{1}{2}}-1)k^2\beta/(2+k^2)^2]\{\gamma^{3/2}[-(2\Gamma$$

$$+ (1+2k^2)/16(\rho^{\frac{1}{2}}-1)^4 k^2\beta(2+k^2))\cos(\beta \ell n\gamma)$$

$$+ (1/[8(\rho^{\frac{1}{2}}-1)^4 k^2(2+k^2)] - (1+2k^2)\Gamma/\beta)\sin(\beta \ell n\gamma)] + 2\Gamma$$

$$+ (1+2k^2)/[16(\rho^{\frac{1}{2}}-1)^4 k^2\beta(2+k^2)]\}$$

$$+ 32(\rho+\rho^{\frac{1}{2}}+1)/[3(\rho^{\frac{1}{2}}-1)^2(2+k^2)^2] - \frac{8}{3}$$

$$+ 4k^2(\rho^{\frac{1}{2}}-1)(\rho^{\frac{m-2}{2m}}-1)/[(-2/m)f_1^2 e^2]$$

where

$$\gamma = 1 + L/2a = \rho^{\frac{1}{2}} = (I_2/I_1)^{\frac{1}{2}}$$

$$\theta = k^4(k^2+2)^2$$

$$\Gamma = \{[\rho^{3/2}/(\rho^{\frac{1}{2}}-1)^5]^{\frac{1}{2}} + [2\beta\sin(\beta \ell n\gamma) - \cos(\beta \ell n\gamma)]/[4(\rho^{\frac{1}{2}}-1)^2]\}/$$

$$\{4(\rho^{\frac{1}{2}}-1)^2 k^2(2+k^2)[\sin(\beta \ell n\gamma) + 2\beta\cos(\beta \ell n\gamma)]\}$$

$$\chi = \{[\rho^{3/2}/(\rho^{\frac{1}{2}}-1)^5]^{\frac{1}{2}} + [2\beta\sin(\beta \ell n\gamma) - \cos(\beta \ell n\gamma)]/[4(\rho^{\frac{1}{2}}-1)^2]\}/$$

$$\{4(\rho^{\frac{1}{2}}-1)^2 k^4 (2+k^2)^2\}$$

$$f = \left(\rho^{\frac{m+2}{2m}}-1\right)^{\frac{3m-1}{2}} / \left[\left(1+\frac{2}{m}\right)^{\frac{3m-1}{2}} (\rho^{\frac{1}{2}}-1)^{\frac{3m-1}{2}}\right]$$

$$f_1 = \left(\rho^{\frac{m+2}{2m}}-1\right)^{\frac{m-1}{2}} / \left[\left(1+\frac{2}{m}\right)^{\frac{m-1}{2}} (\rho^{\frac{1}{2}}-1)^{\frac{m-1}{2}}\right]$$

$$k^2 = Q \frac{\left(\rho^{\frac{m+2}{2m}}-1\right)^m}{\left(1+\frac{2}{m}\right)^m \rho(\rho^{\frac{1}{2}}-1)^m (1-\rho^{-\frac{1}{2}})^2}$$

CHAPTER III

QUASI-STATIC APPROXIMATE SOLUTION

3.1 Introduction

The shallow pinned arch with $I(x) = I_1(x/a)^2$ under a uniformly applied loading is investigated and a closed form solution is reported in Chapter II. This chapter deals with the same problem using an approximate technique with a two-mode response. These two modes are symmetric and anti-symmetric with respect to the plane of structural symmetry. The anti-symmetric mode is shown to be the governing one in Ref. [6] and Ref. [10] for uniform geometry and sufficiently high initial rise parameters. In this chapter a degree of confidence is established for the approximate technique as applied to the above problem by comparing results with those of Chapter II. As a subsequent step, the approximate procedure is used for the half-sine arch with $I(x) = I_1(x/a)^{\frac{1}{2}}$ in order to more completely investigate the effect of nonuniformity on critical loadings. These two chosen inertia investigations may be thought of as a first step toward optimization of shallow arches under quasi-static loadings.

3.2 Governing Equations and Nondimensionalization

Occasion arises, as in Chapter II, when one compares critical nondimensional loadings for different nonuniform stiffnesses, constant volume and a specified nondimensional initial rise parameter. In addition to the nondimensionalization parameters of Chapter II, one

requires the following:

$$w(x) = \rho_o \, \eta(\xi)$$

$$x = (L/\pi)\xi$$

$$a_i = a_i^*/\rho_o, \quad i = 1,2; \text{ amplitudes of modes (Equation 21)}$$

$$U_T = 4U_T^*/P_E \epsilon_E L$$

where

$$\rho_o^2 = I_u/A_u$$

$$\epsilon_E = (\pi\rho_o/L)^2$$

$$P_E = \pi^2 E I_u/L^2$$

By the procedure established in Chapter II the following are determined for $n = \frac{1}{2}$:

$$V_{nu} = 2I_1 L(\rho^3-1)/3\alpha(\rho^2-1) \quad , \qquad m = 1$$

$$V_{nu} = 4I_1^{\frac{1}{2}} L(\rho^{\frac{5}{2}}-1)/5\alpha^{\frac{1}{2}}(\rho^{\frac{1}{2}}-1) \quad , \qquad m = 2$$

$$V_{nu} = 6I_1^{\frac{1}{3}} L(\rho^{\frac{7}{3}}-1)/7\alpha^{\frac{1}{3}}(\rho^2-1) \quad , \qquad m = 3$$

$$I_u = 2I_1(\rho^3-1)/3(\rho^2-1) = \alpha A_u \quad , \qquad m = 1$$

$$I_u = 16I_1(\rho^{\frac{5}{2}}-1)^2/25(\rho^2-1)^2 = \alpha A_u^2 \quad , \qquad m = 2$$

$$I_u = 6^3 I_1(\rho^{\frac{7}{3}}-1)^3/7^3(\rho^3-1)^3 = \alpha A_u^3 , \qquad m = 3$$

Knowing I_u and A_u and defining

$$g_m = (I_u/A_u)(L^2/I_1) = \left(\frac{\alpha}{I_1}\right)^{\frac{1}{m}} L^2 \frac{\left(\rho^{\frac{m+n}{mn}} - 1\right)^{m-1}}{\left(1+\frac{n}{m}\right)^{m-1}\left(\rho^{\frac{1}{n}}-1\right)^{m-1}}$$

and

$$h_m = I_u/I_1 = \left(\frac{I_1}{\alpha}\right)^{\frac{1}{m-1}} \left(\frac{g_m}{L^2}\right)^{\frac{m}{m-1}}$$

one can now nondimensionalize specified quantities in terms of the following parameters:

$$\left.\begin{aligned} g_1 &= \alpha L^2/I_1 \\ g_2 &= (\alpha L^4/4I_1)^{\frac{1}{2}}(1+\rho^{\frac{1}{2}}) \\ g_3 &= 9(\alpha L^6)^{\frac{1}{3}}(\rho^{\frac{5}{6}}-1)^2/25 I_1^{\frac{1}{3}}(\rho^{\frac{1}{2}}-1)^2 \end{aligned}\right\} \qquad n = 2$$

$$\left.\begin{aligned} g_1 &= \alpha L^2/I_1 \\ g_2 &= 4\alpha^{\frac{1}{2}} L^2(\rho^{\frac{5}{2}}-1)/5 I_1^{\frac{1}{2}}(\rho^2-1) \\ g_3 &= 36\,\alpha^{\frac{1}{3}} L^2(\rho^{\frac{7}{3}}-1)^2/49 I_1^{\frac{1}{3}}(\rho^2-1)^2 \end{aligned}\right\} \qquad n = \tfrac{1}{2}$$

$$h_1 = (\rho^{\frac{3}{2}}-1)/3(\rho^{\frac{1}{2}}-1)$$

$$h_2 = (\rho^{\frac{1}{2}}+1)^2/4 \qquad n = 2$$

$$h_3 = 27(\rho^{\frac{5}{6}}-1)^3/125(\rho^{\frac{1}{2}}-1)^3$$

$$h_1 = 2(\rho^3-1)/3(\rho^2-1)$$

$$h_2 = 16(\rho^{\frac{5}{2}}-1)^2/25(\rho^2-1)^2 \qquad n = \frac{1}{2}$$

$$h_3 = 6^3(\rho^{\frac{7}{3}}-1)^3/7^3(\rho^2-1)^3$$

In order to obtain the total potential energy one must develop certain relations. Letting the prime denote a total derivative with respect to ξ one acquires the following expression for Q^* (see Equation 8).

$$Q^* = -(P_E/2)\int_{\pi a/L}^{\pi(a+L)/L} [(\eta')^2 - (\eta_o')^2]d\xi / \int_{\pi a/L}^{\pi(a+L)/L} \frac{d\xi}{\bar{A}(\xi)} \qquad (17)$$

where $\bar{A}(\xi) = A(\xi)/A_u$

$$M = \rho_o P_E \bar{I}(\xi)[\eta_o'' - \eta''] \qquad (18)$$

where $\bar{I}(\xi) = I(\xi)/I_u$

Next, the in-plane equilibrium equation is used in order

to express the total potential solely in terms of the transverse position (w and consequently η) of the reference line points. Forming the dimensional potential energies one acquires

$$\left.\begin{aligned} U^*_{s_T} &= (P_E e_E L/8\pi)\left\{\int_{\pi a/L}^{\pi(a+L)/L} [(\eta')^2 - (\eta_o')^2]d\xi\right\}^2 \Big/ \int_{\pi a/L}^{\pi(a+L)/L} \frac{d\xi}{\bar{A}(\xi)} \\ U^*_{b_T} &= (P_E e_E L/2\pi)\int_{\pi a/L}^{\pi(a+L)/L} \bar{I}(\xi)[\eta_o'' - \eta'']^2\, d\xi \\ U^*_{p_T} &= (P_E e_E L/\pi)\int_{\pi a/L}^{\pi(a+L)/L} q(\xi)[\eta - \eta_o]d\xi \end{aligned}\right\} \quad (19)$$

where

$$U^*_T = U^*_{s_T} + U^*_{b_T} + U^*_{p_T}$$

Therefore, the nondimensional total potential becomes

$$\begin{aligned} U_T &= 4U^*_T/P_E e_E L \\ &= (1/2\pi)\left\{\int_{\pi a/L}^{\pi(a+L)/L} [(\eta')^2 - (\eta_o')^2]d\xi\right\}^2 \Big/ \int_{\pi a/L}^{\pi(a+L)/L} \frac{d\xi}{\bar{A}(\xi)} \\ &\quad + (2/\pi)\int_{\pi a/L}^{\pi(a+L)/L} \bar{I}(\xi)[\eta'' - \eta_o'']^2\, d\xi \\ &\quad + (4/\pi)\int_{\pi a/L}^{\pi(a+L)/L} q(\xi)[\eta - \eta_o]d\xi \end{aligned} \quad (20)$$

Page missing from thesis

$$\psi_{n=2} = (3-2\pi^2)/24\pi - \pi\rho/4(\rho^{\frac{1}{2}}-1)^2 + \pi\rho^{\frac{1}{2}}/4(\rho^{\frac{1}{2}}-1)$$

$$\psi_{n=\frac{1}{2}} = -16\sqrt{2}\,\pi\, D_2/(\rho^2-1)^{\frac{3}{2}}.$$

with

$$D_2 = (1/\pi^{\frac{3}{2}})\int_{\pi a/L}^{\pi\left(a+\frac{L}{2}\right)/L} \xi^{\frac{1}{2}}\sin^2 2\left[(L\xi/\pi) - a - \frac{L}{2}\right]\left(\frac{\pi}{L}\right)d\xi;$$

$$\varphi_{\substack{n=2\\m=1}} = \rho^{\frac{1}{2}} I_1/8\alpha L^2$$

$$\varphi_{\substack{n=2\\m=2}} = I_1^{\frac{1}{2}}(\rho^{\frac{1}{2}}-1)/8\alpha^{\frac{1}{2}}L^2 \ln \rho^{\frac{1}{2}}$$

$$\varphi_{\substack{n=2\\m=3}} = I_1^{\frac{1}{3}}(\rho^{\frac{1}{2}}-1)/24\alpha^{\frac{1}{3}}L^2(\rho^{\frac{1}{6}}-1)$$

$$\varphi_{\substack{n=\frac{1}{2}\\m=1}} = I_1(\rho+1)/\alpha L^2$$

$$\varphi_{\substack{n=\frac{1}{2}\\m=2}} = 3I_1^{\frac{1}{2}}(\rho^2-1)/2\alpha^{\frac{1}{2}}L^2(\rho^{\frac{3}{2}}-1)$$

$$\varphi_{\substack{n=\frac{1}{2}\\m=3}} = 5I_1^{\frac{1}{3}}(\rho^{\frac{1}{2}}-1)/3\alpha^{\frac{1}{3}}L^2(\rho^{\frac{5}{3}}-1)$$

and

$$\tilde{e} = \left(\sqrt{(128/\pi^4)(\rho+\rho^{\frac{1}{2}}+1)/[\rho+\rho^{\frac{1}{2}}+1 + (6/\pi^2)(\rho-1)]} \right) e$$

for all m values.

The equilibrium equations are

$$r_1[r_1^2 - (32/3\pi^2)e^2 + 4a_2^2]$$

$$+ (4\omega/\pi g_m \varphi)(\rho^{\frac{1}{2}}-1)^2(r_1-\tilde{e}) + qh_m/2g_m\varphi = 0 \qquad (23)$$

$$a_2[r_1^2 - (32/3\pi^2)e^2 + 4a_2^2 - 8\psi(\rho^{\frac{1}{2}}-1)^2/\pi g_m\varphi] = 0$$

Since, initially, a comparison with the exact solution is accomplished in order to obtain a measure of confidence for the approximate solution, a_2 is set identically equal to zero. Once the degree of confidence is established, the approximate solution is used to generate results for the entire range of initial rise parameters (antisymmetric buckling as well).

The equilibrium equation for symmetric response is:

$$r_1^3 - [(32/3\pi^2)e^2 - 4\omega(\rho^{\frac{1}{2}}-1)^2/\pi g_m\varphi]r_1 = \mathfrak{Q} \qquad (24)$$

where

$$\mathfrak{Q} = 4\omega\tilde{e}(\rho^{\frac{1}{2}}-1)^2/\pi g_m\varphi - qh_m/2g_m\varphi$$

It can be shown from Equation 24 that there is no snap-through buckling for (see Figure 3.6)

$$e < \sqrt{3\pi\omega(\rho^{\frac{1}{2}}-1)^2/8g_m\varphi} \quad .$$

Symmetric snapping (see Figure 3.7) terminates for (for details see Ref. [6] and Art. 3.4)

$$e = \sqrt{3\pi\psi(\rho^{\frac{1}{2}}-1)^2/4g_m\varphi}$$

The critical loading occurs at the limit point and becomes (see Fig. 3.8 and Ref. [6])

$$q_{cr} = (4/\pi h_m)\{(\pi g_m\varphi/3^{\frac{3}{2}})[(32/3\pi^2)e^2 - 4\omega(\rho^{\frac{1}{2}}-1)^2/\pi g_m\varphi]^{\frac{3}{2}} + 2\omega\tilde{e}(\rho^{\frac{1}{2}}-1)^2\} \qquad (25)$$

The above critical loadings for m=3, different ρ values, and all initial rise parameters corresponding to limit point instability are shown in Figure 3.2 through Figure 3.5. Critical loadings for all three m values are shown in Table 3.1 through Table 3.3. The discrepancy between the Ritz and closed form solutions is greatest for uniform geometry and decreases as the non-uniformity in geometry increases. It is noted in Figure 3.2 through Figure 3.5, for m=3, that the critical loadings predicted by the Ritz method are higher than those for the closed form solution. The worst discrepancy is for the lowest possible initial rise parameter and corresponds to approximately a 6.5 per cent error.

3.4 Shallow Half-Sine Arch with a Half-Sine Loading

Once confidence in the Ritz method is established with a two-

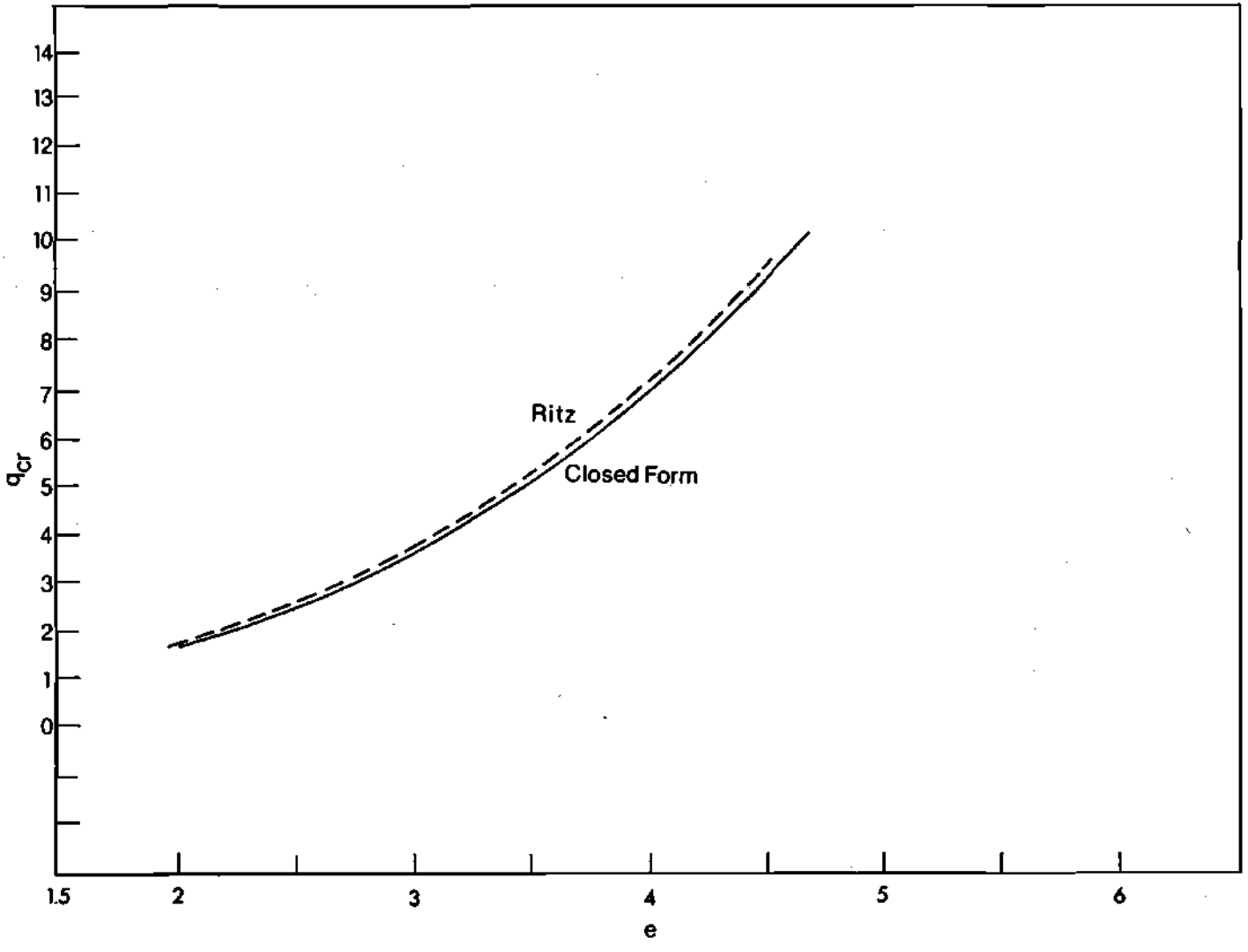

Figure 3.1 Nondimensional Critical Loading versus Initial Rise Parameters, Closed Form and Ritz Solutions, $I_1/I_2 = 1.0$.

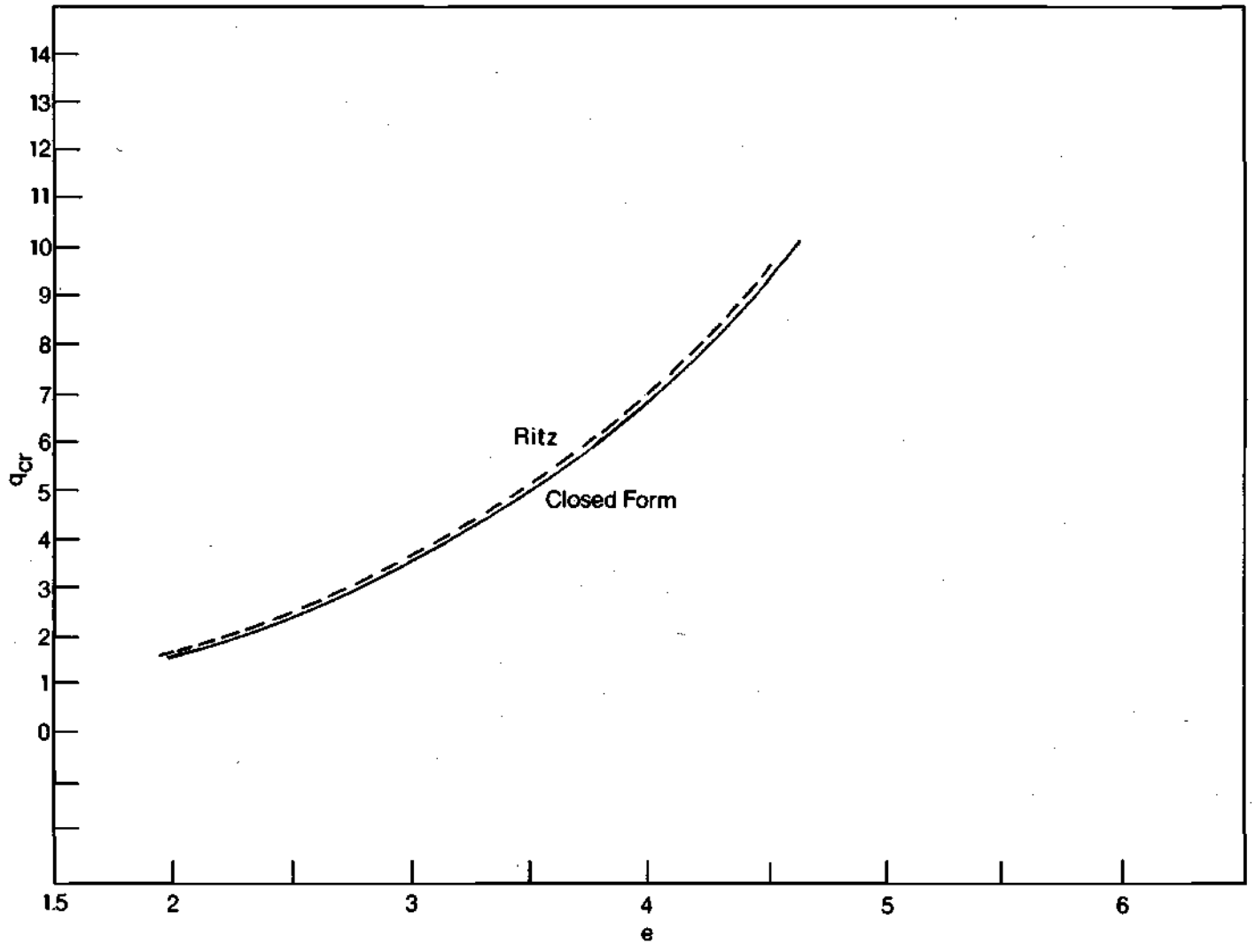

Figure 3.2 Nondimensional Critical Loading versus Initial Rise Parameters, Closed Form and Ritz Solutions, $I_1/I_2 = 0.9$, $m = 3$, $n = 2$.

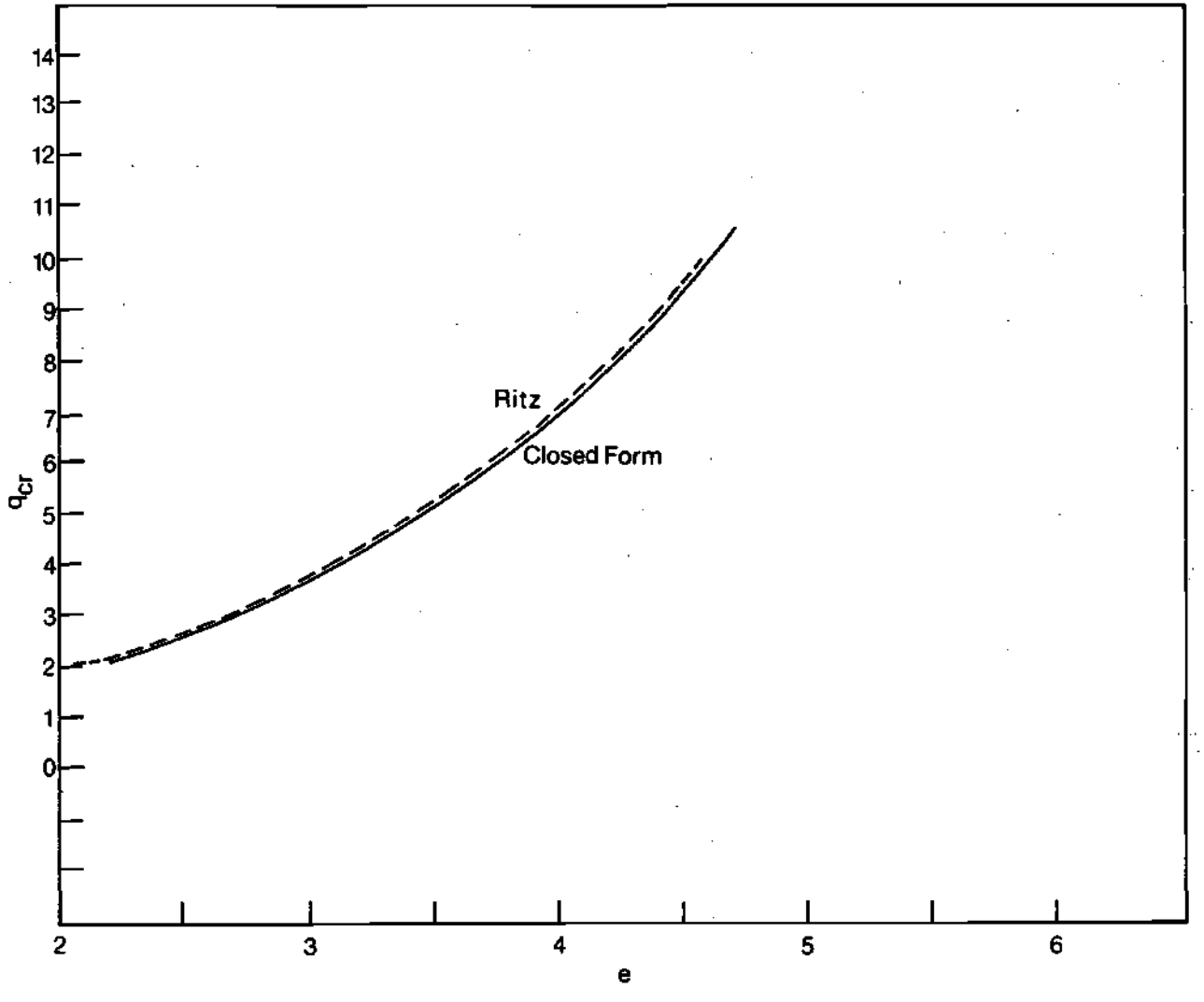

Figure 3.3 Nondimensional Critical Loading versus Initial Rise Parameters, Closed Form and Ritz Solutions, $I_1/I_2 = 0.4$, $m = 3$, $n = 2$.

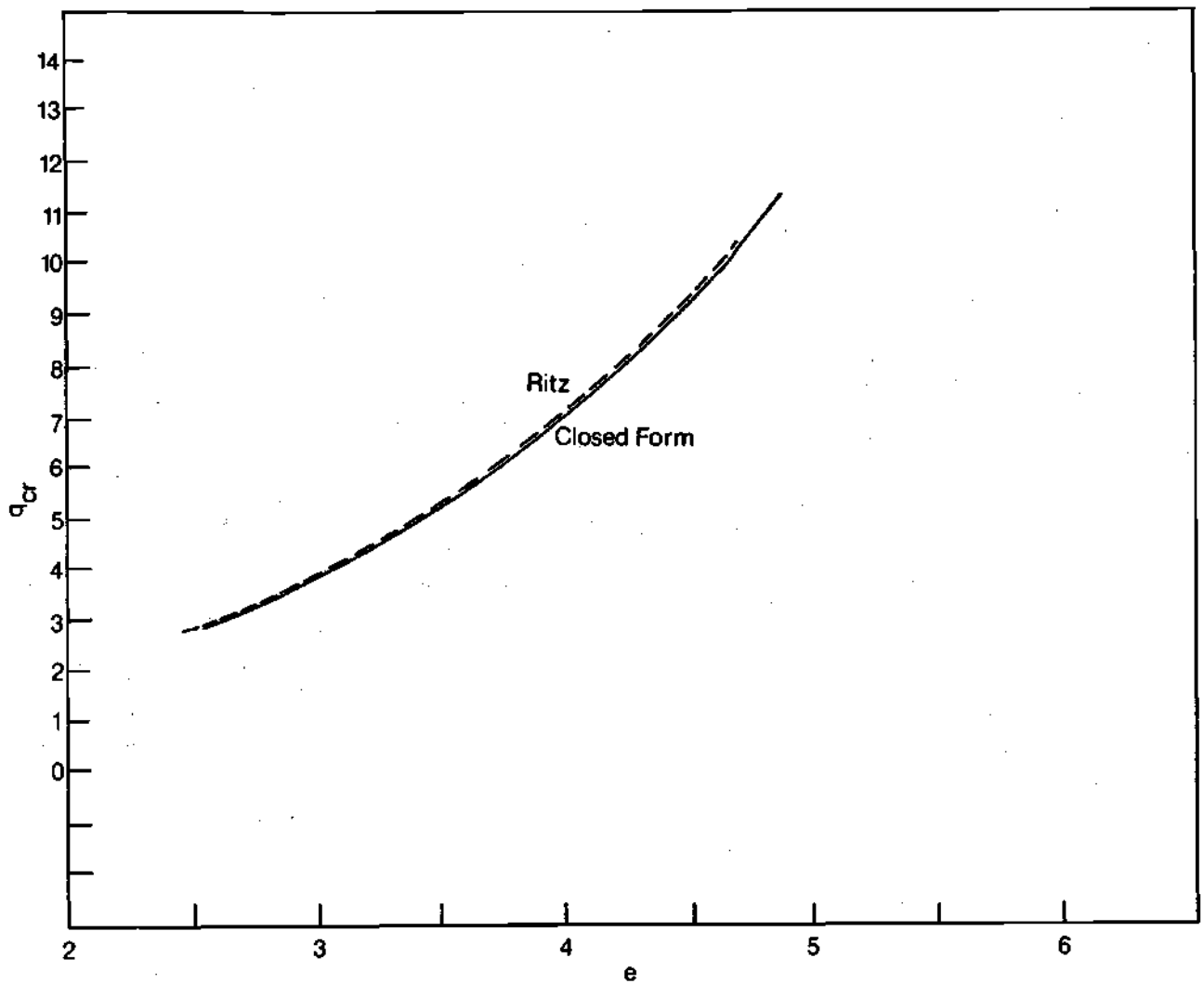

Figure 3.4 Nondimensional Critical Loading versus Initial Rise Parameters, Closed Form and Ritz Solutions, $I_1/I_2 = 0.1$, $m = 3$, $n = 2$.

Table 3.1 Critical Loadings and Initial Rise Parameters Shown in Figures 3.1 through 3.4, m=3, n=2.

I_1/I_2	Ritz		Closed Form	
	e	q_{cr}	e	q_{cr}
1.0	1.94	1.74	1.97	1.61
	3.00	3.71	3.00	3.48
	4.00	7.20	4.00	6.82
	4.51	9.64	4.69	10.20
0.9	1.94	1.75	1.97	1.62
	3.00	3.71	3.00	3.48
	4.00	7.20	4.00	6.82
	4.51	9.64	4.69	10.20
0.4	2.12	2.12	2.19	2.10
	3.00	3.80	3.00	3.69
	4.00	7.28	4.00	7.06
	4.52	9.85	4.69	10.58
0.1	2.46	2.85	2.54	2.78
	3.00	3.90	3.00	3.83
	4.00	7.19	4.00	7.19
	4.67	10.50	4.84	11.48

Table 3.2 Critical Loadings and Initial Rise Parameters, m=2, n=2.

I_1/I_2	Ritz		Closed Form	
	e	q_{cr}	e	q_{cr}
0.9	1.94	1.75	1.97	1.61
	3.00	3.71	3.00	3.48
	4.00	7.20	4.00	6.82
	4.51	9.64	4.69	10.20
0.4	2.12	2.11	2.22	1.99
	3.00	3.77	3.00	3.68
	4.00	7.22	4.00	6.98
	4.52	9.82	4.70	10.51
0.1	2.49	2.80	2.58	2.76
	3.00	3.73	3.00	3.82
	4.00	6.55	4.00	6.31
	4.73	10.31	4.91	11.27

Table 3.3 Critical Loadings and Initial Rise Parameters, m=1, n=2.

I_1/I_2	Ritz		Closed Form	
	e	q_{cr}	e	q_{cr}
0.9	1.94	1.75	1.97	1.61
	3.00	3.71	3.00	3.48
	4.00	7.20	4.00	6.82
	4.51	9.64	4.69	10.20
0.4	2.16	2.11	2.26	2.05
	3.00	3.64	3.00	3.61
	4.00	6.93	4.00	6.81
	4.60	9.82	4.79	10.50
0.1	2.77	2.86	2.85	2.82
	3.00	3.18	3.00	3.15
	4.00	5.80	4.00	6.07
	5.26	10.51	5.48	11.45

mode representation, the problem is now to investigate the pinned shallow half-sine arch under a half-sine loading for the two inertia distributions, $I(x) = I_1\left(\frac{x}{a}\right)^2$ and $I(x) = I_1\left(\frac{x}{a}\right)^{\frac{1}{2}}$, and all m values. The total potential for $n=2$ and $n=\frac{1}{2}$ becomes

$$\left.\begin{aligned} U_T(r_1,a_2) &= (g_m\varphi/h_m)(r_1^2-e^2+4a_2^2)^2 \\ &\quad + [8(\rho^{\frac{1}{2}}-1)^2/\pi h_m][(r_1-e)^2\omega - 8a_2^2\psi] + 2q_1(r_1-e),\ n=2 \\ \text{and} \\ U_T(r_1,a_2) &= (g_m\varphi/16h_m)(r_1^2-e^2+4a_2^2)^2 \\ &\quad + [(\rho^{\frac{1}{2}}-1)^2/2\pi h_m][(r_1-e)^2\omega - 8a_2^2\psi] + 2q_1(r_1-e),\ n=\tfrac{1}{2} \end{aligned}\right\} \quad (26)$$

The principle of the stationary value of the total potential leads to the following equilibrium equations for $n = 2$ and $n = \frac{1}{2}$, respectively:

$$\left.\begin{aligned} &r_1(r_1^2-e^2+4a_2^2) + (4\omega/\pi\varphi g_m)(\rho^{\frac{1}{2}}-1)^2(r_1-e) + q_1h_m/2g_m\varphi = 0 \\ &a_2[r_1^2-e^2+4a_2^2-8\psi(\rho^{\frac{1}{2}}-1)^2/\pi g_m\varphi] = 0 \end{aligned}\right\} \ n=2$$

$$\left.\begin{aligned} &r_1(r_1^2-e^2+4a_2^2) + (4\omega/\pi g_m\varphi)(\rho^{\frac{1}{2}}-1)^2(r_1-e) + 8q_1h_m/g_m\varphi = 0 \\ &a_2[r_1^2-e^2+4a_2^2-8\psi(\rho^{\frac{1}{2}}-1)^2/\pi g_m\varphi] = 0 \end{aligned}\right\} \ n=\tfrac{1}{2} \quad (27)$$

One defines $\bar{q}$ for $n = 2$ and $n = \frac{1}{2}$, respectively as

$$\bar{Q} = 4\omega e(\rho^{\frac{1}{2}}-1)^2/\pi g_m\varphi - q_1 h_m/2g_m\varphi \qquad n=2$$
$$\bar{Q} = 4\omega e(\rho^{\frac{1}{2}}-1)^2/\pi g_m\varphi - 8q_1 h_m/g_m\varphi \qquad n=\tfrac{1}{2} \tag{28}$$

The equilibrium equations for both n values become

$$\bar{Q} = [r_1^2-e^2+4a_2^2+4\omega(\rho^{\frac{1}{2}}-1)^2/\pi g_m\varphi]r_1$$
$$a_2[r_1^2-e^2+4a_2^2-8\psi(\rho^{\frac{1}{2}}-1)/\pi g_m\varphi] = 0 \tag{29}$$

There are two possible solutions to the equilibrium equations

i) $r_1 \neq 0$, $a_2 \equiv 0$

ii) $r_1 \neq 0$, $a_2 \neq 0$

Case i and ii correspond to purely symmetric and to symmetric and anti-symmetric modes for a given rise parameter range. Since $a_2 \equiv 0$ in case i, then

$$r_1^3 - [e^2 - 4\omega(\rho^{\frac{1}{2}}-1)^2/\pi g_m\varphi]r_1 = \bar{Q} \tag{30}$$

Thus, there is no possibility of snapping for (see Fig. 3.6)

$$e < \sqrt{4\omega(\rho^{\frac{1}{n}}-1)^2/\pi g_m\varphi}$$

All possible quasi-static equilibrium positions are depicted in Figure 3.5. Case ii is possible if

$$e \geq \sqrt{-8\psi(\rho^{\frac{1}{n}}-1)^2/\pi g_m\varphi}$$

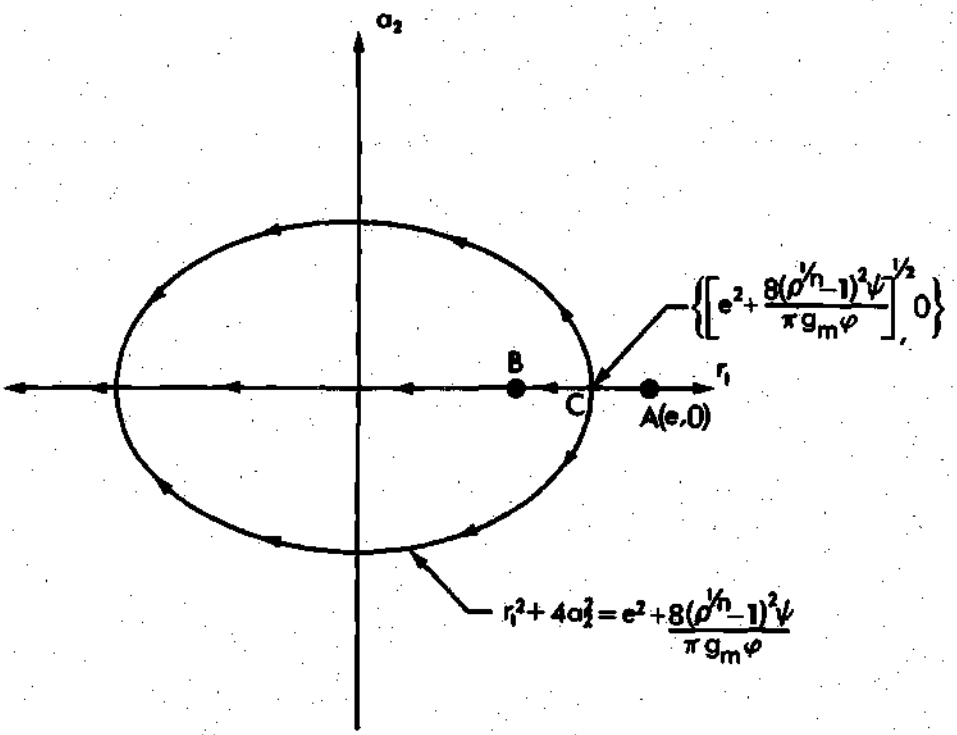

Figure 3.5 Quasi-Static Equilibrium Positions in the (r_1, a_2) Configuration Space.

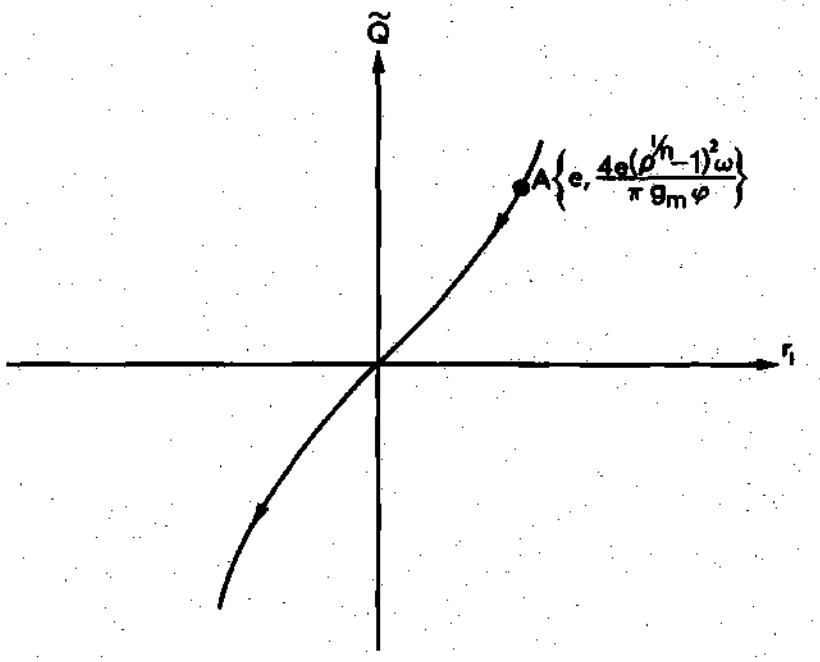

Figure 3.6 Load-Deflection Curve Corresponding to No Snap-Through Buckling, Very Shallow Arch.

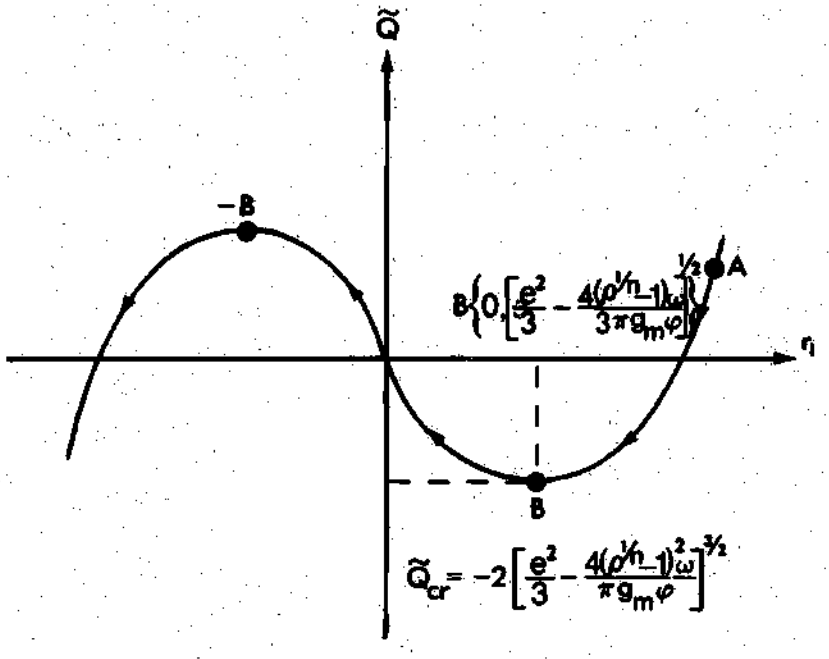

Figure 3.7 Load-Deflection Curve for Limit Point Instability.

When antisymmetric modes are possible, the expression for $\mathfrak{Q}$ and a_2 in terms of r_1 are given below (obtained from the equilibrium equations).

$$\mathfrak{Q} = r_1 4(\omega+2\psi)(\rho^{\frac{1}{n}}-1)^2/\pi g_m \varphi$$

$$4a_2^2 = e^2 + 8\psi(\rho^{\frac{1}{n}}-1)^2/\pi g_m \varphi - \pi^2 g_m^2 \varphi^2 \mathfrak{Q}^2/16(\rho^{\frac{1}{n}}-1)^4(\omega+2\psi)^2 \tag{31}$$

Figure 3.6 represents all possible positions of equilibrium. Figures 3.7 through 3.9 represent all of the possibilities of load-deflection paths depending upon the value of the rise parameter and the structural geometry. Examining all equilibrium configurations for infinitesimal disturbances, the sufficient conditions for stability (in the small) of quasi-static equilibrium positions are

$$\begin{vmatrix} \dfrac{\partial^2 U_T}{\partial r_1^2} & \dfrac{\partial^2 U_T}{\partial r_1 \partial a_2} \\ \dfrac{\partial^2 U_T}{\partial a_2 \partial r_1} & \dfrac{\partial^2 U_T}{\partial a_2^2} \end{vmatrix} > 0$$

The above conditions lead to the following two inequalities when buckling is governed by the symmetric mode (see Figures 3.7 and 3.8).

$$r_1^2 - [e^2/3 - 4\omega(\rho^{\frac{1}{n}}-1)^2/3\pi g_m \varphi] > 0$$

$$r_1^2 - [e^2 + 8\psi(\rho^{\frac{1}{n}}-1)^2/\pi g_m \varphi] > 0$$

Therefore, in Figures 3.7 and 3.8, the equilibrium positions from -B to B are unstable (in the small). When buckling is governed by the antisymmetric mode the conditions for stability become (see Figure 3.9)

$$r_1^2 + 2(\omega+2\psi)(\rho^{\frac{1}{n}}-1)^2/\pi g_m \psi > 0$$

$$\omega + 2\psi > 0$$

Therefore, the elliptic equilibrium positions of Figure 3.5 are unstable (in the small).

Critical loadings are determined for a complete range of initial rise parameters. The three critical ranges are as follows:

$$\alpha) \quad \text{If } \sqrt{4\omega(\rho^{\frac{1}{n}}-1)^2/\pi g_m \varphi} \; < e \leq \sqrt{-8\psi(\rho^{\frac{1}{n}}-1)^2/\pi g_m \varphi} \;,$$

as in Figure 3.7, the system will reach point B and snap through a symmetric mode only. The critical loading at the limit point, B, becomes

$$\tilde{Q}_{cr} = -(2/3^{\frac{3}{2}})[e^2 - 4\omega(\rho^{\frac{1}{n}}-1)^2/\pi g_m \varphi]^{\frac{3}{2}}$$

or, for n = 2,

$$q_{1_{cr}} = (4/\pi h_m)\{(\pi g_m \varphi/3^{\frac{3}{2}})[e^2 - 4\omega(\rho^{\frac{1}{n}}-1)^2/\pi g_m \varphi]^{\frac{3}{2}} + 2\omega e(\rho^{\frac{1}{n}}-1)^2\} \quad (32)$$

and one sixteenth of Equation 32 for $n = \frac{1}{2}$.

$$\beta) \quad \text{If } \sqrt{-8\psi(\rho^{\frac{1}{n}}-1)^2/\pi g_m \varphi} \; \leq e \; < \sqrt{-2(\omega+2\psi)(\rho^{\frac{1}{n}}-1)^2/\pi g_m \varphi} \;,$$

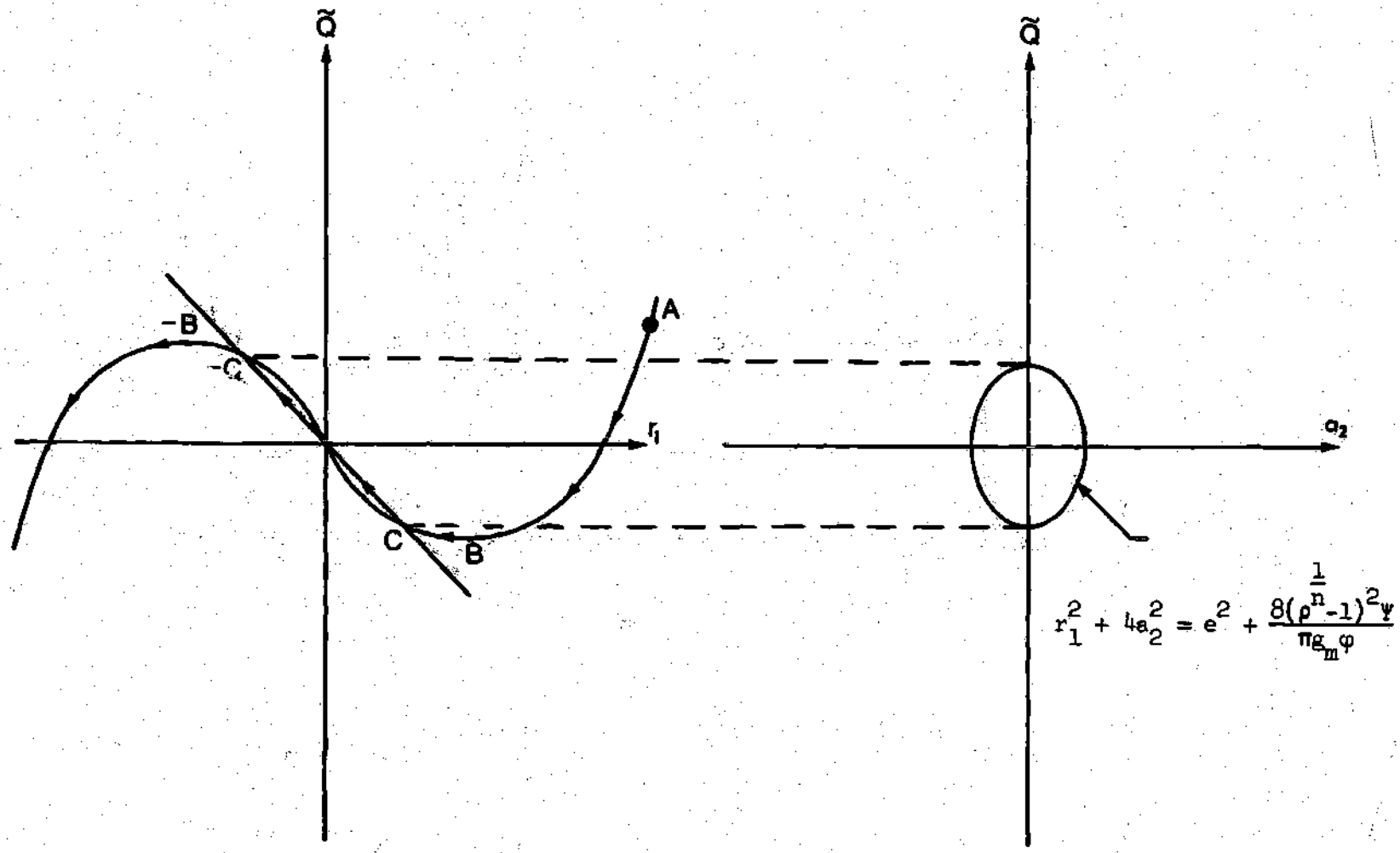

Figure 3.8 Load-Deflection Curve and Corresponding (r_1, a_2) Equilibrium Ellipse for Limit Point Instability, Transient Antisymmetric Mode.

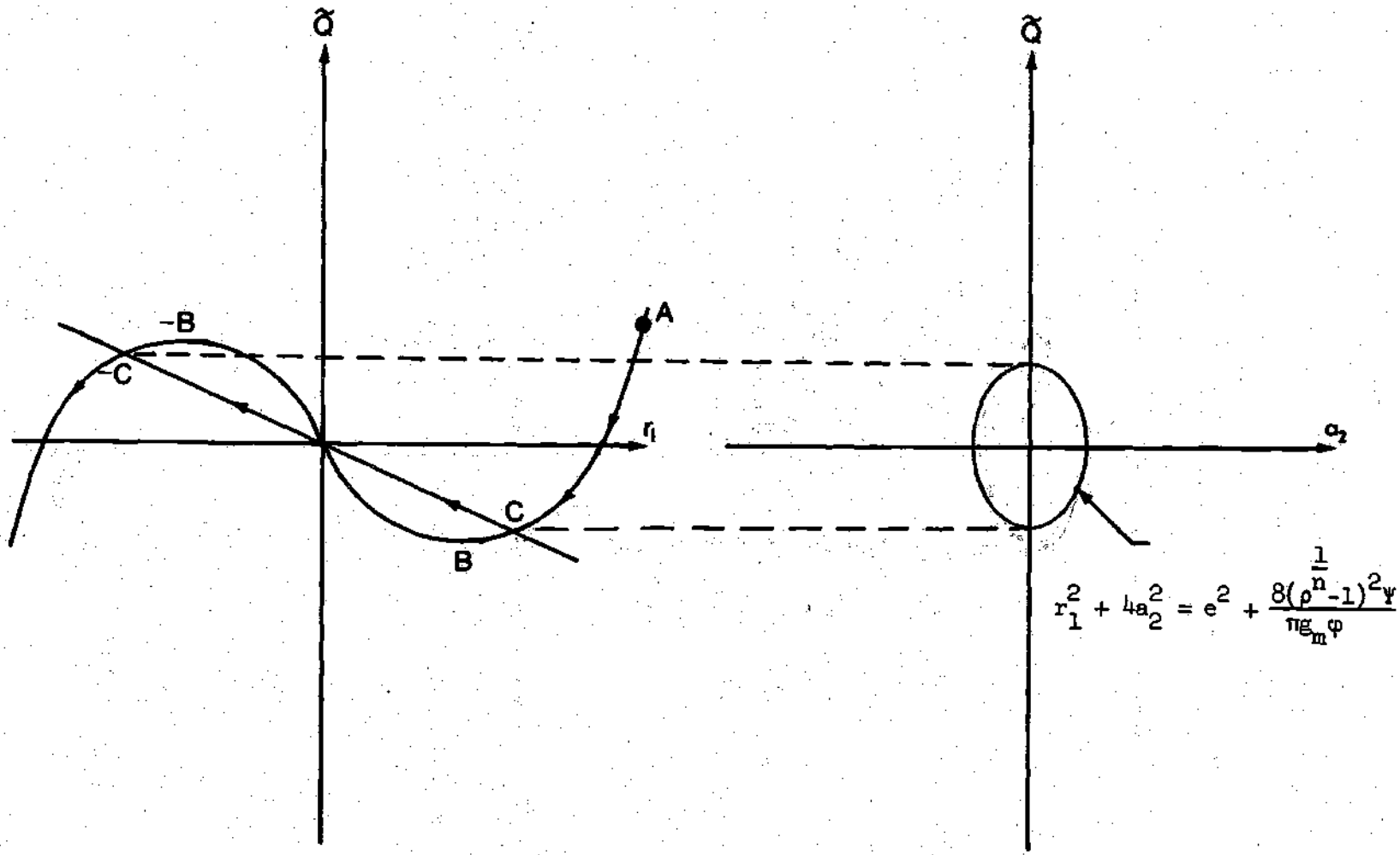

Figure 3.9 Load-Deflection Curve and Corresponding (r_1, a_2) Equilibrium Ellipse for Purely Antisymmetric Buckling.

as in Figure 3.8, the system will reach point B and snap-through initially by a symmetric mode. The critical loading is still that given in case α.

$$\gamma) \quad \text{If} \qquad e \geq \sqrt{-2(\omega+2\Psi)(\rho^{\frac{1}{n}}-1)^2/\pi g_m \varphi} \quad ,$$

as in Figure 3.9, the system will reach point C and snap-through in an antisymmetric mode. The critical loading is determined by the antisymmetric equilibrium equations, Equations 31, evaluated at the r_1 coordinate of point C. Thus, for n = 2,

$$q_{1_{cr}} = [8(\rho^{\frac{1}{n}}-1)^2/\pi h_m]\{-(\omega+2\Psi)[e^2 + 8\Psi(\rho^{\frac{1}{n}}-1)^2/\pi g_m \varphi] + \omega e\} \qquad (33)$$

and one sixteenth of the above for $n = \frac{1}{2}$.

Before discussing the results, it is shown that the ratio of non-dimensional critical loads is equal to the ratio of dimensional critical loads. The same is true for initial rise parameters. First, one must determine, through the nondimensionalization process, the dimensional critical loading ($q^*_{1_{cr}}$), for both uniform and nonuniform stiffnesses, as a function of the nondimensional critical loading ($q_{1_{cr}}$) and the volume of the structure.

$$V_{nu} = \frac{L}{\pi} \int_{\frac{\pi a}{L}}^{\frac{\pi}{L}(a+L)} A(\xi)d\xi = \frac{L}{\pi} \left[\int_{\frac{\pi a}{L}}^{\frac{\pi}{L}(a+L)} d\xi \right] \left[\frac{q^*_{1nu}}{q_{1nu}} \frac{L^2}{\pi^2 E \alpha^{\frac{3}{2}}} \right]^{\frac{2}{3m-1}}$$

Thus,

$$q^*_{lu} = \frac{E\pi^2}{L^2} \frac{\alpha^{\frac{3}{2}}}{L^{\frac{m+1}{2}}} V_u^{\frac{3m-1}{2}} q_{lu}$$

$$q^*_{lnu} = \frac{E\pi^2}{L^2} \frac{\alpha^{\frac{3}{2}}}{L^{\frac{m+1}{2}}} V_{nu}^{\frac{3m-1}{2}} q_{lnu}$$

Since $e\ \rho_o = e^*$ where $\rho_o^2 = I_u/A_u$

$$e^*_u = \frac{\alpha^{\frac{1}{2}}}{L^{\frac{m-1}{2}}} V_u^{\frac{m-1}{2}} e_u$$

and

$$V_{nu} = \frac{L}{\pi} \int_{\frac{n\pi a}{L}}^{\frac{\pi}{L}(a+L)} A(\xi)d\xi = \frac{L}{\pi} \left[\int_{\frac{n\pi a}{L}}^{\frac{\pi}{L}(a+L)} d\xi \right] \left[\frac{e^*_{nu}}{e_{nu}} \frac{1}{\alpha^{\frac{1}{2}}} \right]^{\frac{2}{m-1}}$$

Therefore,

$$e^*_{nu} = \sqrt{\frac{\alpha}{L^{m-1}}} V_{nu}^{\frac{m-1}{2}} e_{nu}$$

Equating non-uniform and uniform geometry volumes one obtains

$$\left(\frac{e^*_{nu}}{e_{nu}}\right)^{\frac{2}{m-1}} = \left(\frac{e^*_u}{e_u}\right)^{\frac{2}{m-1}}$$

$$\left(\frac{q^*_{1nu}}{q_{1nu}}\right)^{\frac{2}{3m-1}} = \left(\frac{q^*_{1u}}{q_{1u}}\right)^{\frac{2}{3m-1}}$$

Thus,

$$\frac{e^*_{nu}}{e^*_{u}} = \frac{e_{nu}}{e_{u}}$$

$$\frac{q^*_{1nu}}{q^*_{1u}} = \frac{q_{1nu}}{q_{1u}}$$

The generated data are presented graphically in Figures 3.10 through 3.22. First, for n = 2 and m = 1, 2 and 3, the data are shown in Figures 3.10 through 3.12 when buckling is governed by the symmetric mode. These results are also tabulated in Tables 3.3 through 3.5. It is seen that, for m = 1, nonuniform geometries realize a considerable decrease in load carrying capability over the uniform geometry, except for moderate nonuniformity. It should be noted that m = 1 is the case when only the base of the cross-sectional area is allowed to vary while retaining the same volume as the uniform arch. For m = 2, critical loadings are greater than for uniform geometry except for extreme nonuniformity. Apparently, so much material is forced towards the center of the arch, for extreme nonuniformity, that the overall resisting stiffness becomes less effective in carrying the applied loading. For m = 3, only the height varies while retaining constant volume. This distribution of material realizes the highest critical loadings which increase with increasing nonuniformity for

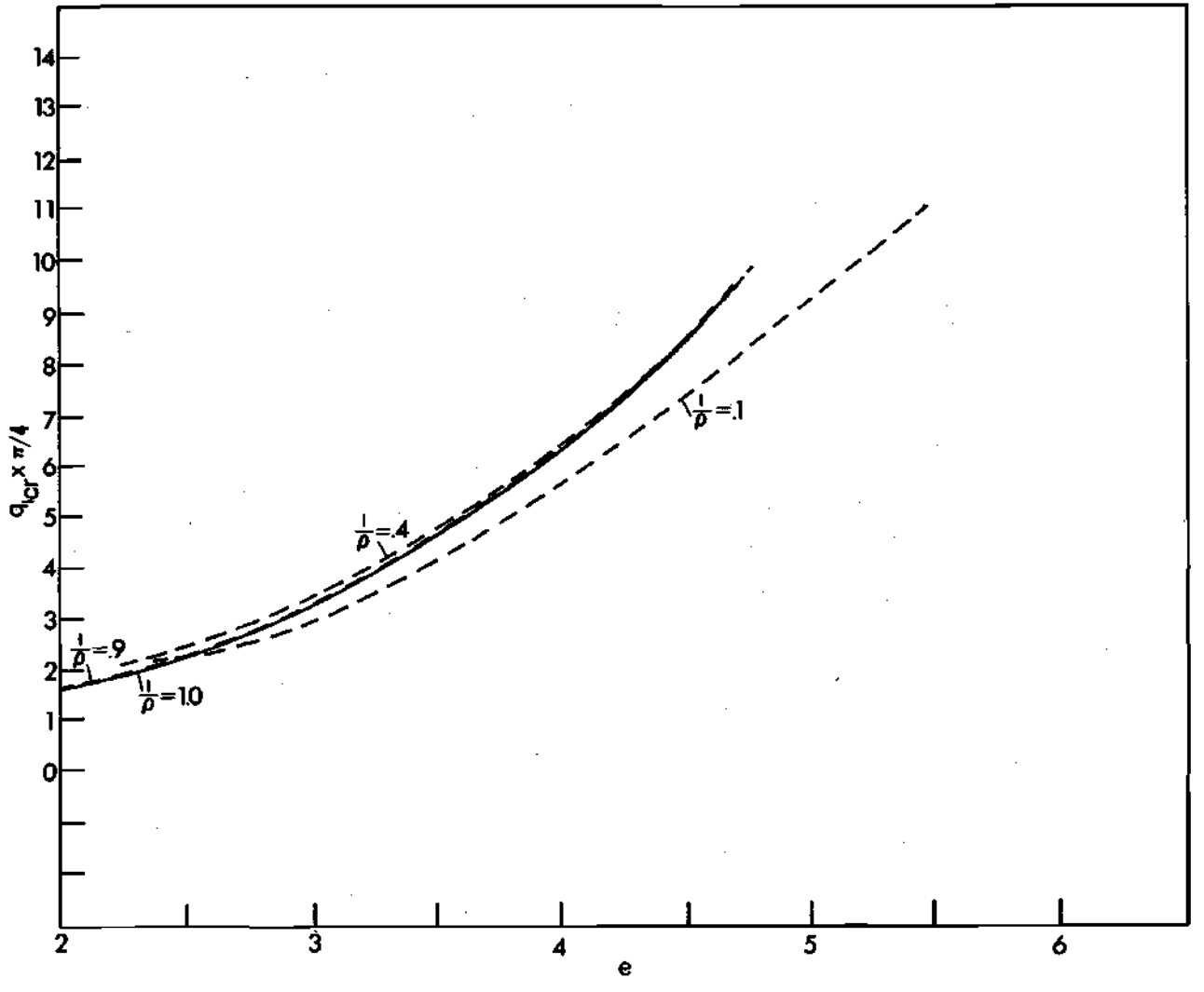

Figure 3.10 Nondimensional Critical Loadings versus Initial Rise Parameters, m = 1, n = 2.

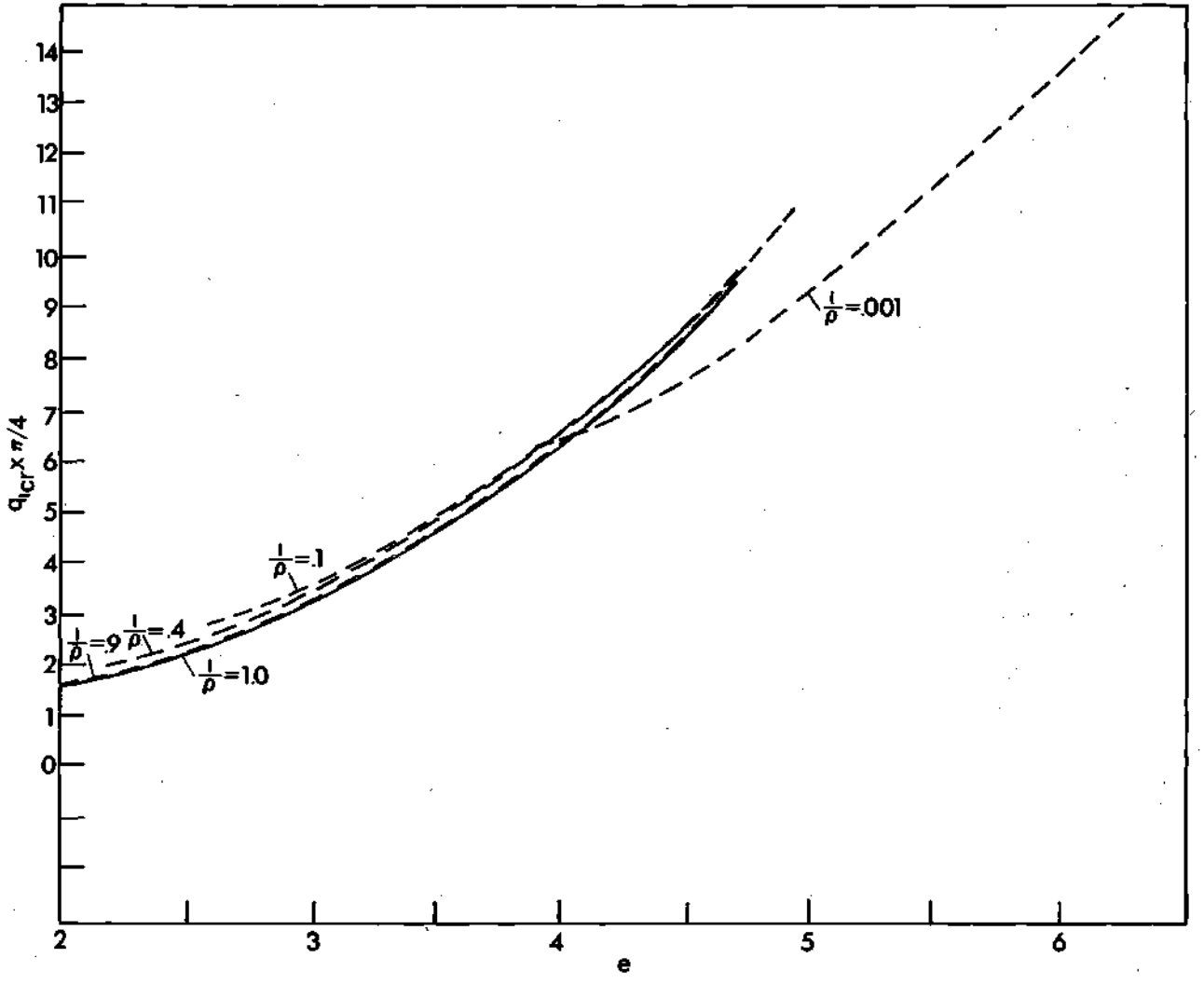

Figure 3.11 Nondimensional Critical Loadings versus Initial Rise Parameters, m = 2, n = 2.

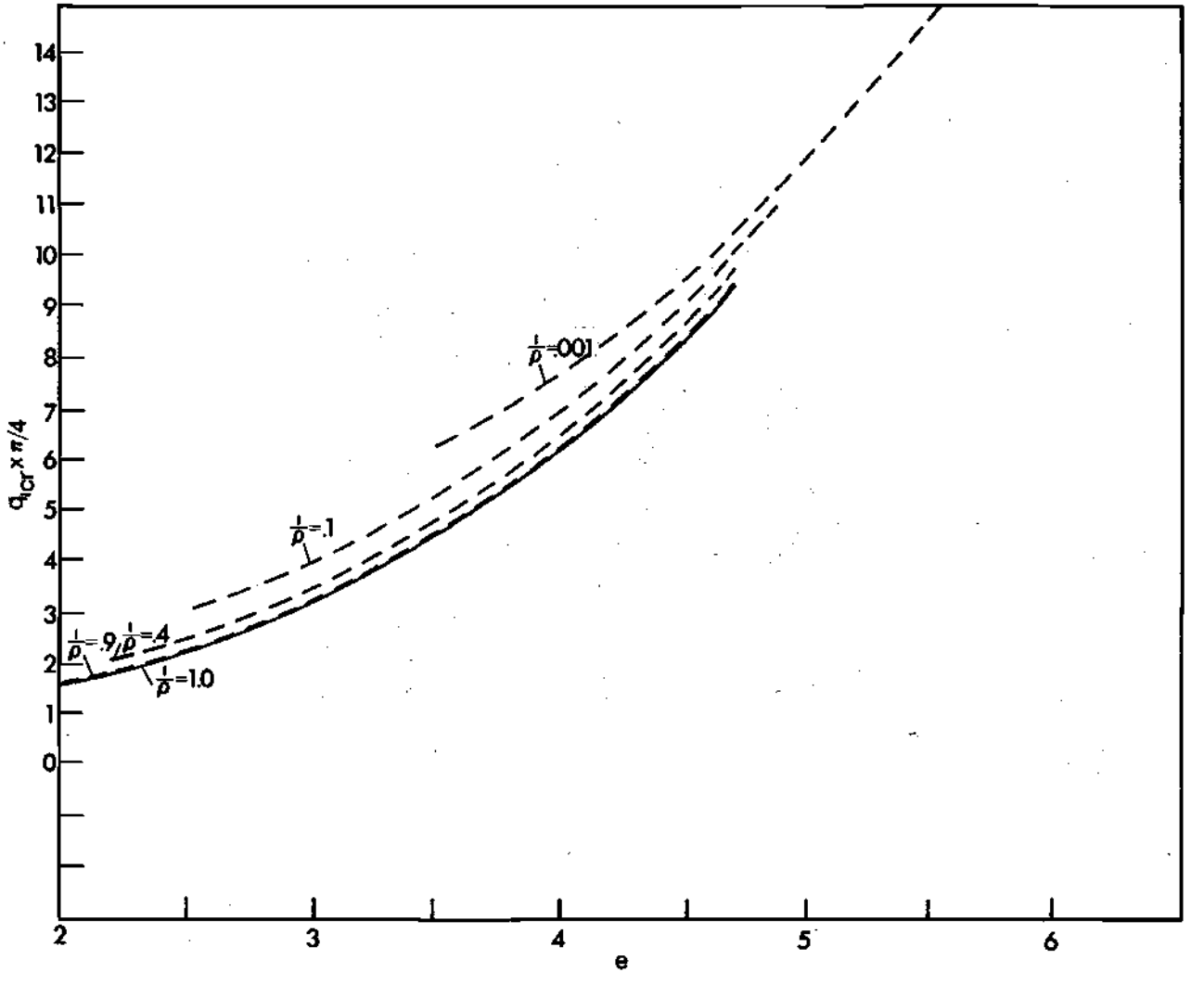

Figure 3.12 Nondimensional Critical Loading versus Initial Rise Parameters, m = 3, n = 2.

Table 3.4 Critical Loadings and Initial Rise Parameters Shown in Figure 3.10, m = 1, n = 2.

I_1/I_2	e	q_{cr}
1.0	2.00	1.57
	3.00	3.21
	4.00	6.29
	4.69	9.48
0.9	2.02	1.62
	3.00	3.22
	4.00	6.29
	4.69	9.47
0.4	2.25	2.08
	3.00	3.39
	4.00	6.34
	4.79	9.76
0.1	2.88	2.13
	3.00	2.83
	4.00	5.56
	5.47	11.04
0.001	8.32	8.16
	10.00	10.74
	12.00	15.30
	13.81	21.00

Table 3.5 Critical Loadings and Initial Rise Parameters Shown in Figure 3.11, m = 2, n = 2.

I_1/I_2	e	q_{cr}
1.0	2.00	1.57
	3.00	3.21
	4.00	6.29
	4.69	9.48
0.9	2.02	1.62
	3.00	3.22
	4.00	6.29
	4.68	9.44
0.4	2.21	2.08
	3.00	3.37
	4.00	6.49
	4.70	9.75
0.1	2.59	2.75
	3.00	3.50
	4.00	6.47
	4.92	10.82
0.001	3.89	6.28
	5.00	9.34
	6.00	13.48
	6.46	15.93

Table 3.6 Critical Loadings and Initial Rise Parameters Shown in Figure 3.12, m = 3, n = 2.

I_1/I_2	e	q_{cr}
1.0	2.00	1.57
	3.00	3.21
	4.00	6.29
	4.69	9.48
0.9	2.02	1.62
	3.00	3.22
	4.00	6.29
	4.69	9.48
0.4	2.20	2.09
	3.00	3.49
	4.00	6.58
	4.69	9.78
0.1	2.56	3.13
	3.00	3.99
	4.00	7.11
	4.86	11.03
0.001	3.52	6.29
	4.00	7.62
	5.00	12.09
	5.73	16.17

all initial rise parameters in this range.

Data are also generated for $n = \frac{1}{2}$ and m = 1, 2 and 3 as shown in Figures 3.13 through 3.15 when buckling is also governed by the symmetric mode. These data are tabulated in Tables 3.7 through 3.9. For m = 1 and 2, geometries with $n = \frac{1}{2}$ realize a better load carrying capability than those with n = 2. For m = 3, geometries with n = 2 realize the best load carrying capability.

For a certain range of initial rise parameters the antisymmetric mode governs buckling. Critical loadings versus initial rise parameters corresponding to this range are shown in Figures 3.16 through 3.21. Figures 3.16 through 3.18 correspond to n = 2 and m = 1, 2 and 3. For m = 1, as the nonuniformity increases the critical loadings, for the same initial rise parameter, become smaller. This is not the case when buckling is governed by the symmetric mode. For m = 2 and 3, as the nonuniformity increases the critical load carrying capability becomes greater. As is expected, geometries for m = 3 yield the best load carrying capability. A plot of critical loadings versus initial rise parameters is shown graphically in Figures 3.19 through 3.21 for $n = \frac{1}{2}$ and m = 1, 2 and 3, when buckling is governed by the antisymmetric mode. For all m values, the nonuniform geometry critical loadings are greater than those for uniform geometry and increase with increasing nonuniformity with the exception of low initial rise parameters for m = 1. The best load carrying capability is again realized for m = 3. Furthermore, for m = 3, geometries with n = 2 yield higher critical loadings than those with $n = \frac{1}{2}$.

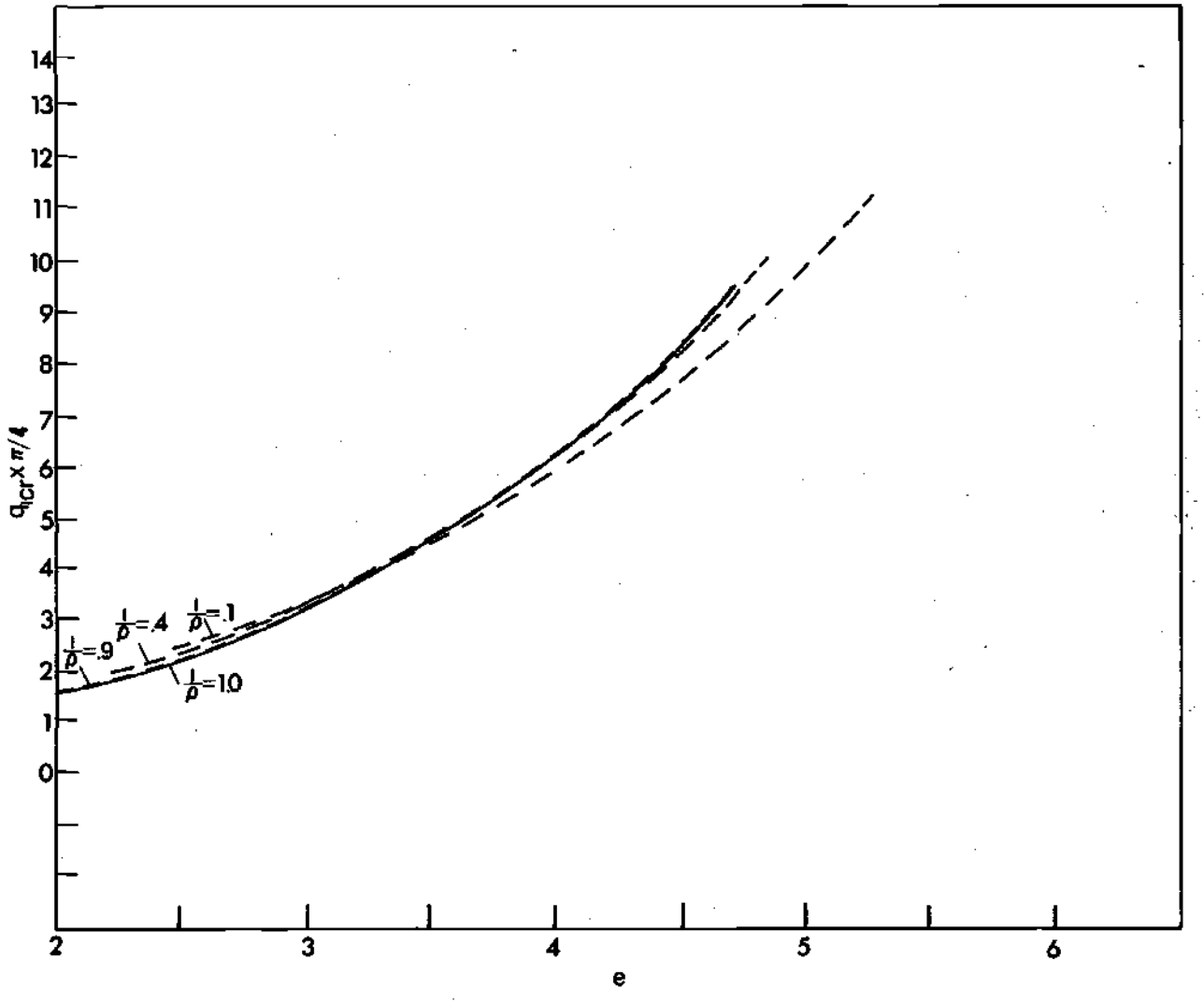

Figure 3.13 Nondimensional Critical Loadings versus Initial Rise Parameters, Limit Point, Ritz Solution, Initial Half-Sine Shape, m = 1, n = 1/2.

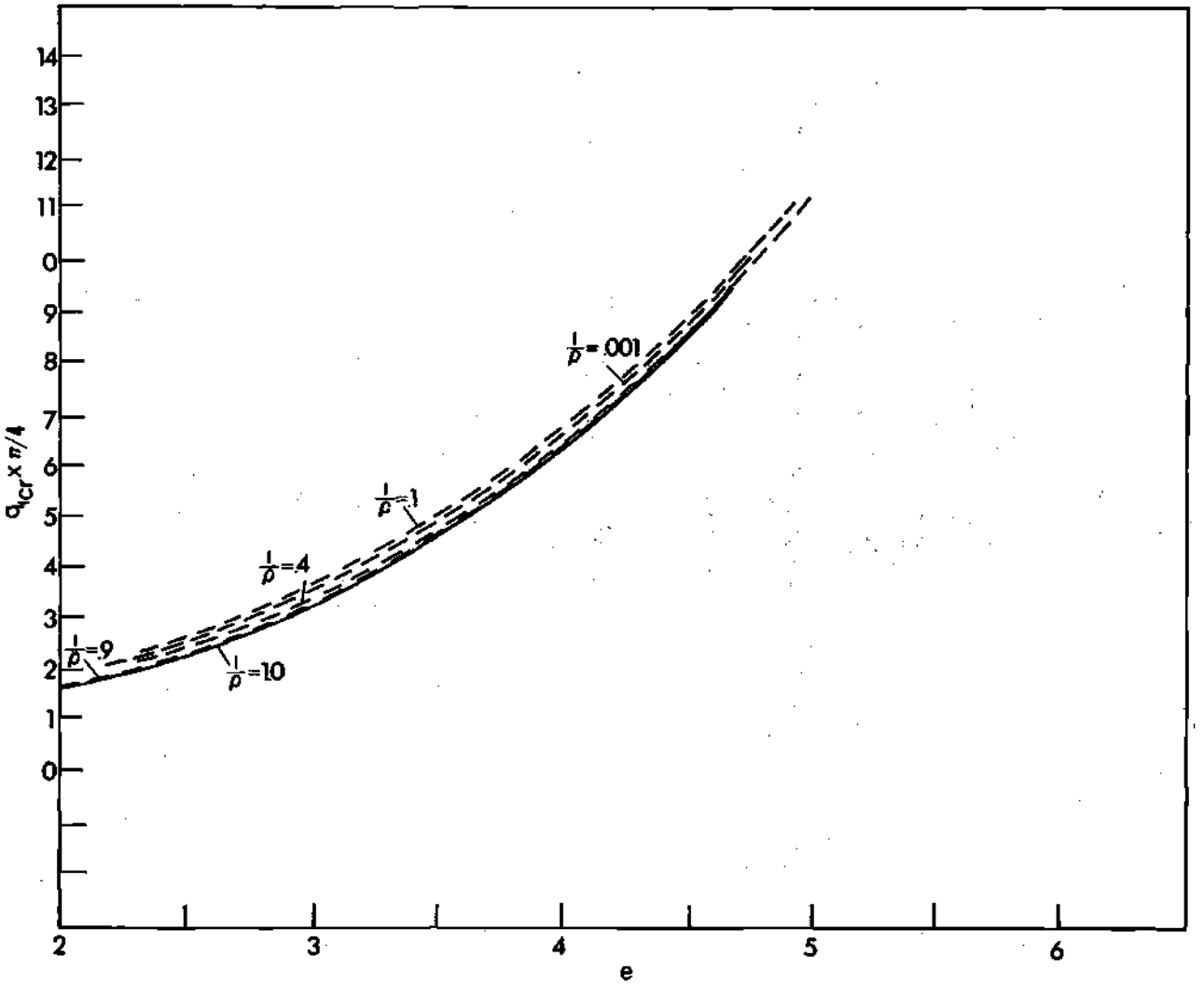

Figure 3.14 Nondimensional Critical Loading versus Initial Rise Parameters, Limit Point, Ritz Solution, Initial Half-Sine Shape, m = 2, n = 1/2.

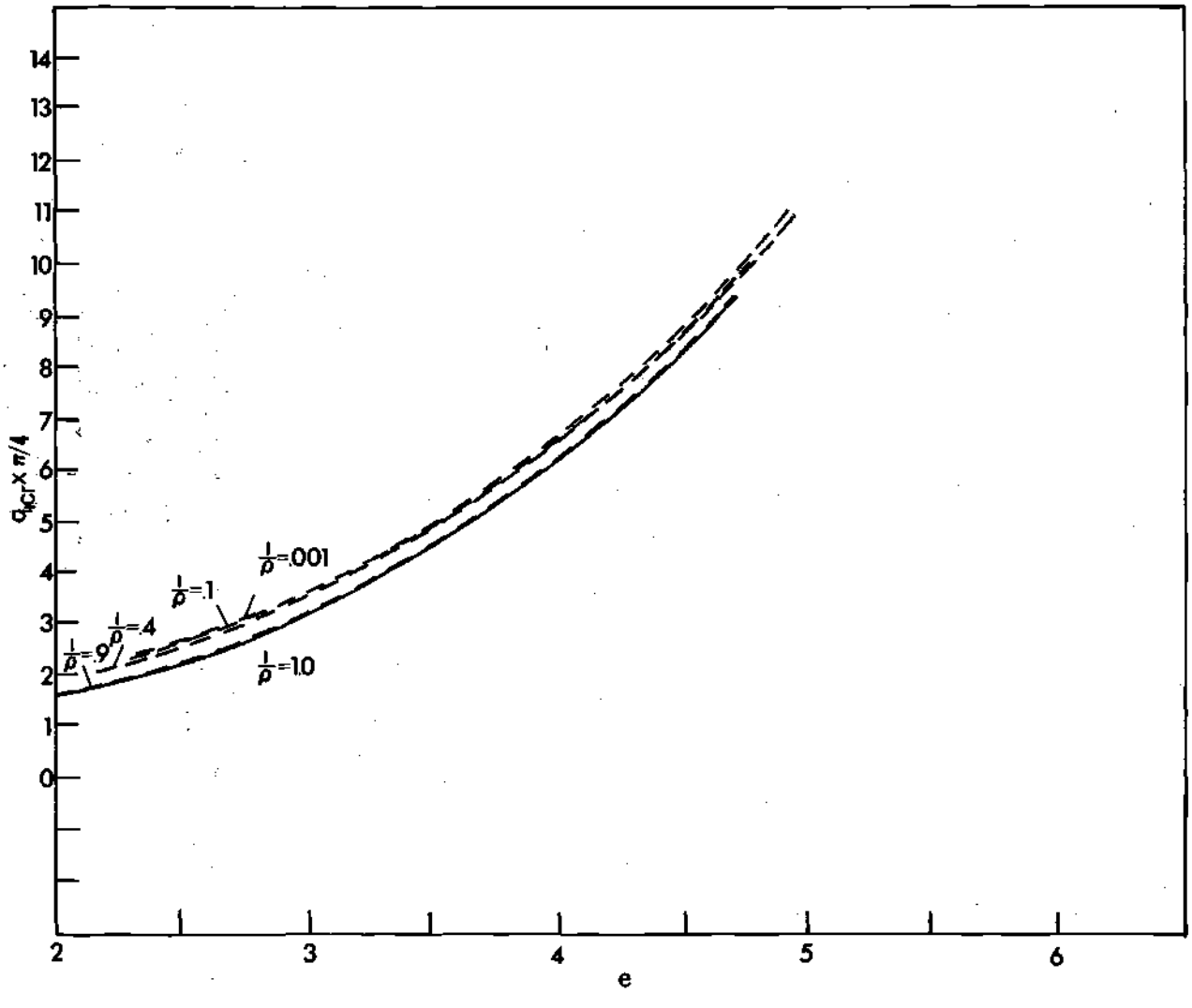

Figure 3.15 Nondimensional Critical Loading versus Initial Rise Parameters, Limit Point, Ritz Solution, Initial Half-Sine Shape, m = 3, n = 1/2.

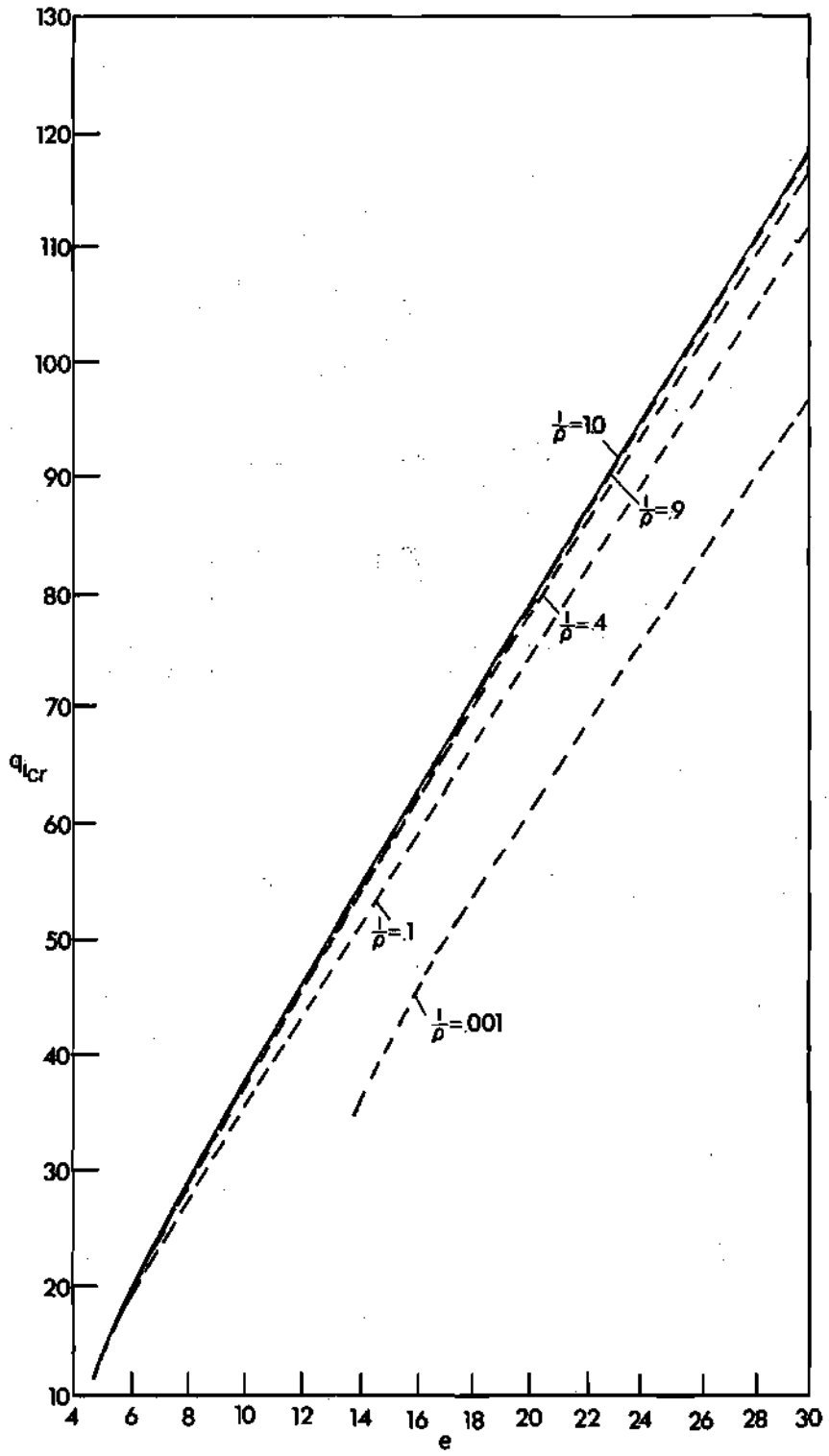

Figure 3.16 Nondimensional Critical Loading versus Initial Rise Parameters, m = 1, n = 2.

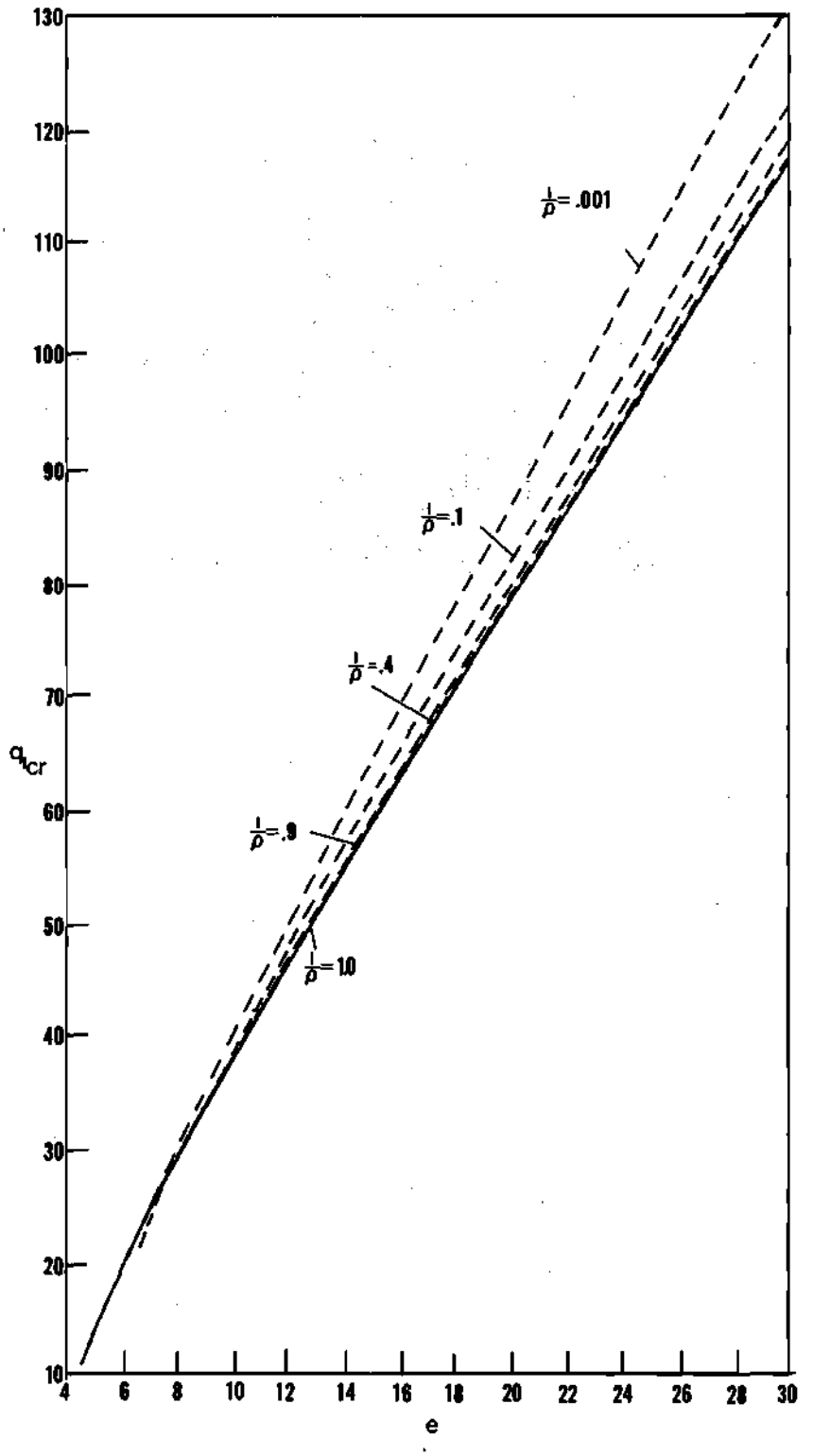

Figure 3.17 Nondimensional Critical Loading versus Initial Rise Parameters, m = 2, n = 2.

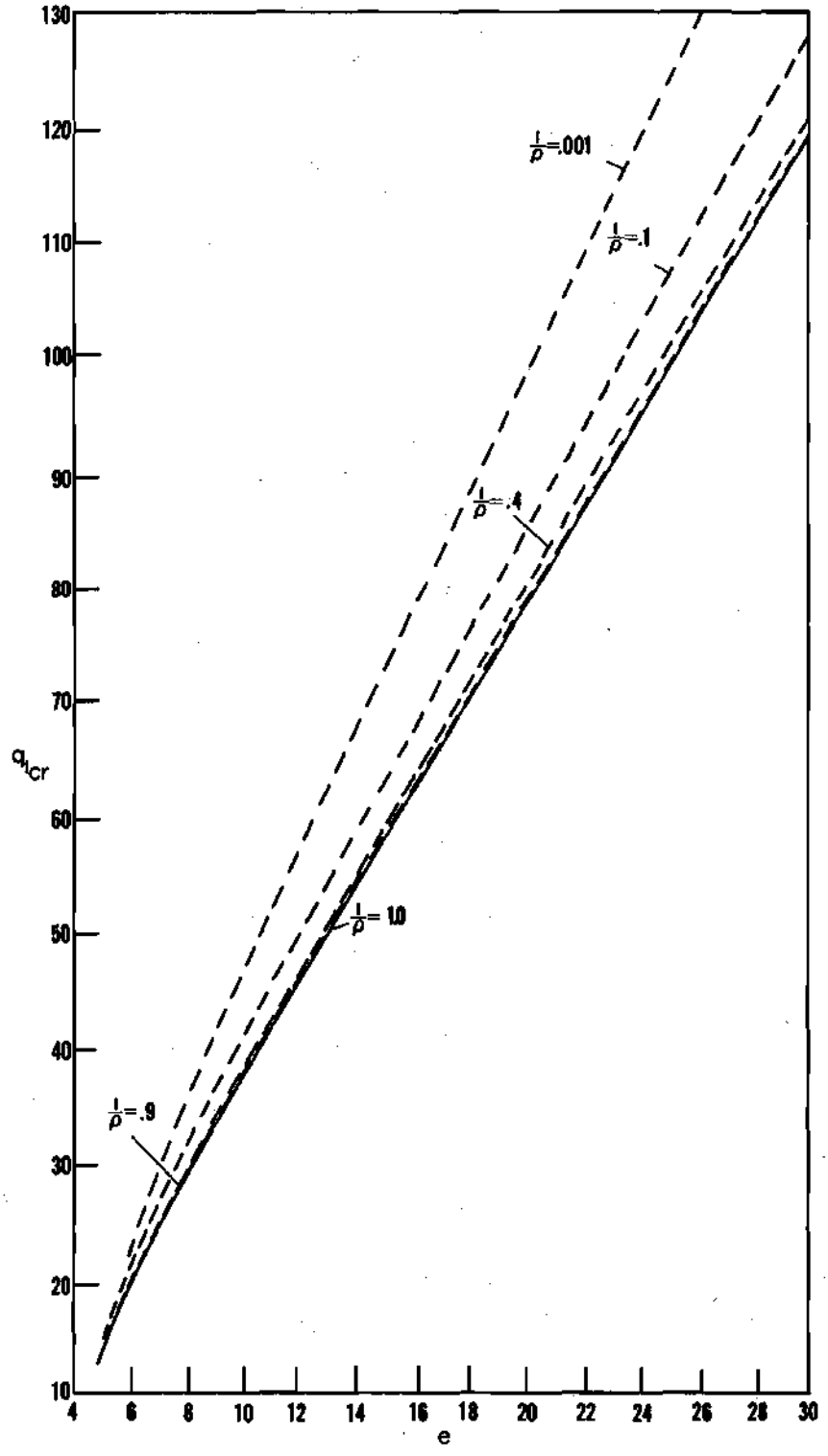

Figure 3.18 Nondimensional Critical Loading versus Initial Rise Parameters, m = 3, n = 2.

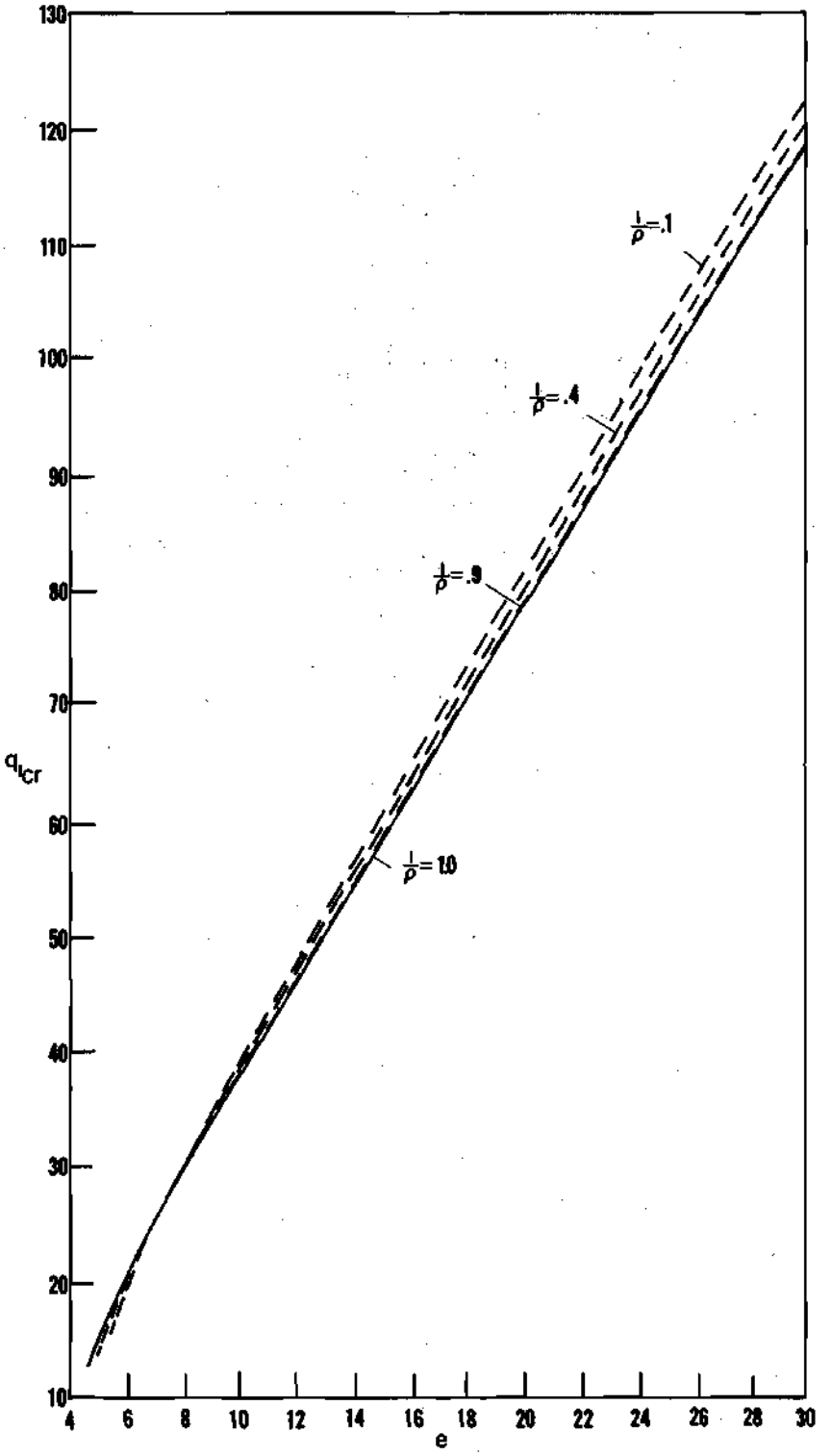

Figure 3.19 Nondimensional Critical Loading versus Initial Rise Parameters, m = 1, n = 1/2.

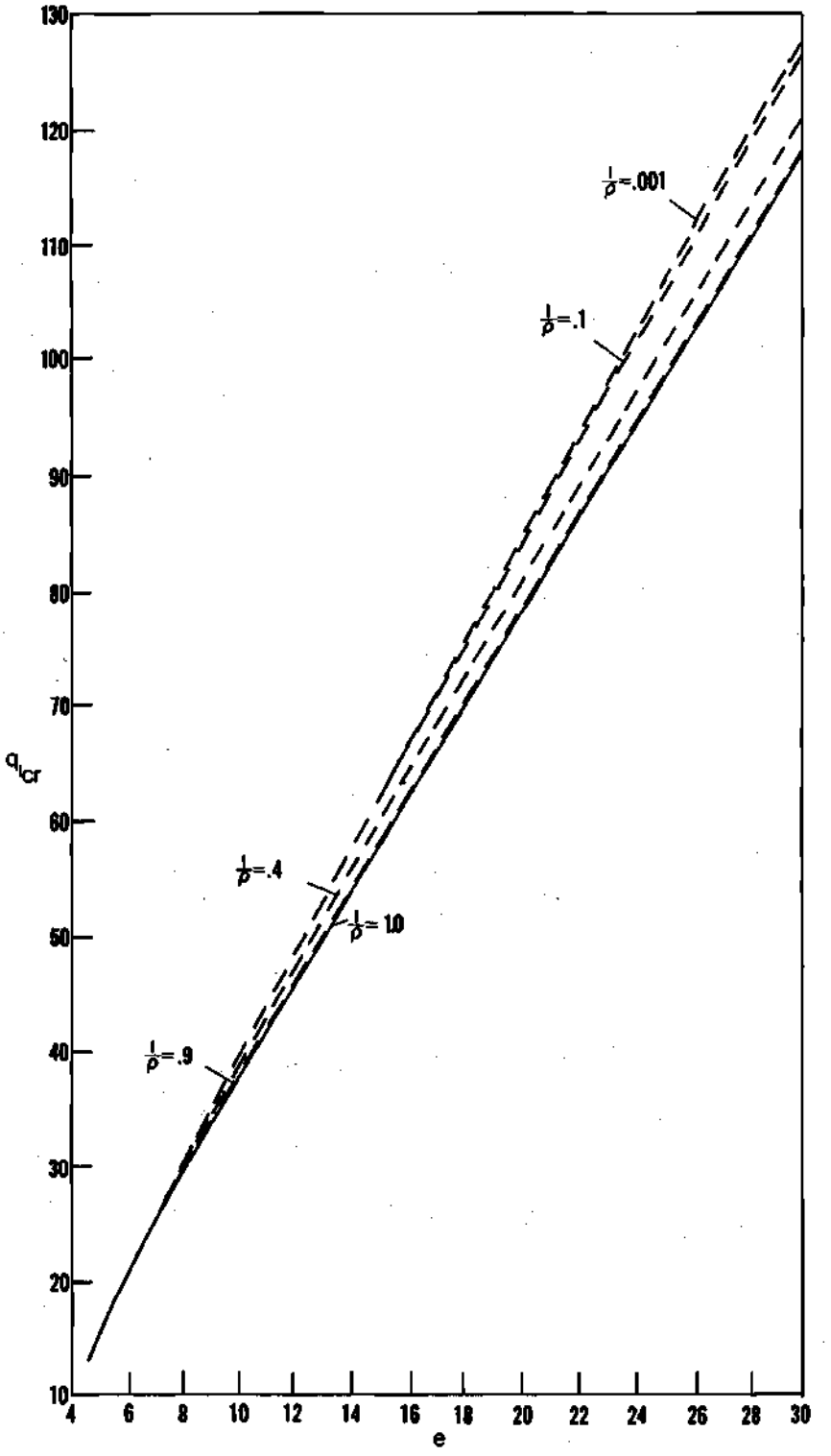

Figure 3.20 Nondimensional Critical Loading versus Initial Rise Parameters, m = 2, n = 1/2.

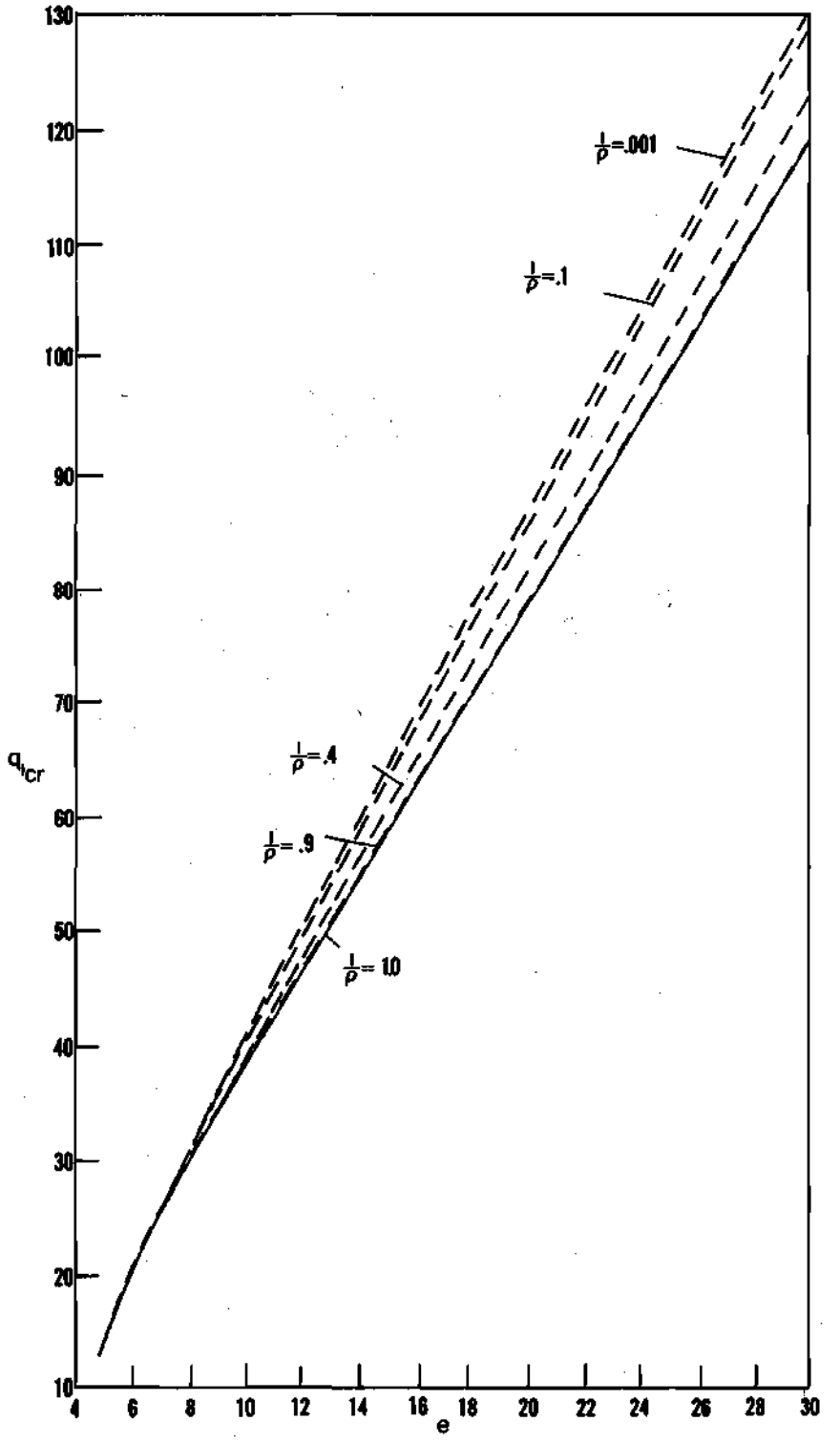

Figure 3.21 Nondimensional Critical Loading versus Initial Rise Parameters, m = 3, n = 1/2.

Table 3.7 Critical Loadings and Initial Rise Parameters Shown in Figure 3.13, $m = 1$, $n = \frac{1}{2}$.

I_1/I_2	e	q_{cr}
1.0	2.00	1.57
	3.00	3.21
	4.00	6.29
	4.69	9.48
0.9	2.02	1.62
	3.00	3.21
	4.00	6.29
	4.69	9.48
0.4	2.22	2.01
	3.00	3.40
	4.00	6.29
	4.84	10.07
0.1	2.46	2.38
	3.00	3.31
	4.00	5.96
	5.24	11.20

Table 3.8 Critical Loadings and Initial Rise Parameters Shown in Figure 3.14, $m = 2$, $n = \frac{1}{2}$.

I_1/I_2	e	q_{cr}
1.0	2.00	1.57
	3.00	3.21
	4.00	6.29
	4.69	9.48
0.9	2.02	1.62
	3.00	3.22
	4.00	6.30
	4.69	9.48
0.4	2.18	2.01
	3.00	3.57
	4.00	6.50
	4.77	10.05
0.1	2.31	2.33
	3.00	3.66
	4.00	6.64
	4.94	10.96
0.001	2.35	2.37
	3.00	3.47
	4.00	6.43
	5.00	11.11

Table 3.9 Critical Loadings and Initial Rise Parameters Shown in Figure 3.15, $m = 3$, $n = \frac{1}{2}$.

I_1/I_2	e	q_{cr}
1.0	2.00	1.57
	3.00	3.21
	4.00	6.29
	4.69	9.48
0.9	2.02	1.62
	3.00	3.22
	4.00	6.29
	4.69	9.48
0.4	2.18	2.02
	3.00	3.62
	4.00	6.59
	4.76	10.08
0.1	2.30	2.34
	3.00	3.62
	4.00	6.59
	4.91	11.03
0.001	2.33	2.40
	3.00	3.69
	4.00	6.66
	4.95	10.99

Table 3.10 Critical Loadings and Initial Rise Parameters Shown in Figure 3.16, m = 1, n = 2.

I_1/I_2	e	$q_{1_{cr}}$
1.0	4.69	12.05
	10.00	37.50
	20.00	78.70
	30.00	119.30
0.9	4.69	12.05
	10.00	37.50
	20.00	78.70
	30.00	119.20
0.4	4.79	12.43
	10.00	37.12
	20.00	77.97
	30.00	117.96
0.1	5.47	14.06
	10.00	35.08
	20.00	74.60
	30.00	113.06
0.001	13.81	33.06
	16.00	44.55
	20.00	61.16
	30.00	98.57

Table 3.11 Critical Loadings and Initial Rise Parameters Shown in Figure 3.17, m = 2, n = 2.

I_1/I_2	e	$q_{1_{cr}}$
1.0	4.69	12.05
	10.00	37.50
	20.00	78.70
	30.00	119.30
0.9	4.69	12.01
	10.00	37.45
	20.00	78.65
	30.00	118.98
0.4	4.70	12.41
	10.00	37.83
	20.00	79.33
	30.00	120.02
0.1	4.92	13.78
	10.00	38.88
	20.00	81.60
	30.00	123.43
0.001	6.46	20.41
	10.00	40.19
	20.00	87.04
	30.00	132.26

Table 3.12 Critical Loadings and Initial Rise Parameters Shown in Figure 3.18, m = 3, n = 2.

I_1/I_2	e	$q_{1_{cr}}$
1.0	4.69	12.05
	10.00	37.50
	20.00	78.70
	30.00	119.15
0.9	4.69	12.05
	10.00	37.51
	20.00	78.78
	30.00	119.18
0.4	4.69	12.45
	10.00	38.02
	20.00	79.71
	30.00	120.55
0.1	4.86	14.04
	10.00	40.19
	20.00	84.25
	30.00	127.40
0.001	5.79	20.65
	10.00	46.50
	20.00	98.89
	30.00	149.86

Table 3.13 Critical Loadings and Initial Rise Parameters Shown in Figure 3.19, $m = 1$, $n = \frac{1}{2}$.

I_1/I_2	e	$q_{1_{cr}}$
1.0	4.69	12.05
	10.00	37.50
	20.00	78.70
	30.00	119.15
0.9	4.69	12.07
	10.00	37.52
	20.00	78.82
	30.00	119.23
0.4	4.84	12.82
	10.00	38.01
	20.00	80.00
	30.00	121.07
0.1	5.24	14.25
	10.00	38.38
	20.00	81.51
	30.00	123.52

Table 3.14 Critical Loadings and Initial Rise Parameters Shown in Figure 3.20, $m = 2$, $n = \frac{1}{2}$.

I_1/I_2	e	$q_{1_{cr}}$
1.0	4.69	12.05
	10.00	37.50
	20.00	78.70
	30.00	119.15
0.9	4.69	12.07
	10.00	37.53
	20.00	78.84
	30.00	119.26
0.4	4.77	12.80
	10.00	38.62
	20.00	81.15
	30.00	122.76
0.1	4.94	13.95
	10.00	40.16
	20.00	84.68
	30.00	128.18
0.001	5.00	14.15
	10.00	40.20
	20.00	84.88
	30.00	128.50

Table 3.15 Critical Loadings and Initial Rise Parameters Shown in Figure 3.21, $m = 3$, $n = \frac{1}{2}$.

I_1/I_2	e	$q_{1_{cr}}$
1.0	4.69	12.05
	10.00	37.50
	20.00	78.70
	30.00	119.15
0.9	4.69	12.07
	10.00	37.55
	20.00	78.87
	30.00	119.32
0.4	4.76	12.83
	10.00	38.81
	20.00	81.52
	30.00	123.33
0.1	4.91	14.04
	10.00	40.76
	20.00	85.88
	30.00	129.97
0.001	4.95	14.28
	10.00	41.10
	20.00	85.35
	30.00	131.05

3.5 Weight Savings

Another objective, in addition to the comparison of critical loadings for constant volume, is to determine the weight savings realized over the uniform geometry structure. Weight savings of a material with the same mass density are determined by finding the ratio of volume for nonuniform stiffness to the volume for uniform stiffness at the same dimensional critical loading and the same dimensional initial rise parameter. Equating dimensional critical loadings ($q^*_{1_{cr}}$), as shown before, one obtains

$$\frac{q_{1nu_{cr}}}{q_{1u_{cr}}} = \left(\frac{1}{\bar{V}}\right)^{\frac{3m-1}{2}}$$

where

$$\bar{V} = \frac{V_{nu}}{V_u} .$$

Equating dimensional initial rise parameters (e^*) one acquires

$$\frac{e_{nu}}{e_u} = \left(\frac{1}{\bar{V}}\right)^{\frac{m-1}{2}}$$

From Ref. [6] the critical loadings for uniform geometry and symmetric and antisymmetric modes, respectively are

$$q_{lu_{cr}} = e_u + \left(\frac{1}{2}\right)\left[(e_u^2 - 4)/3\right]^{\frac{3}{2}}$$

$$q_{lu_{cr}} = e_u + 3\left[e_u^2 - 16\right]^{\frac{1}{2}} \quad .$$

By replacing e_u by e_{nu} and $q_{u_{cr}}$ by functions of e_{nu} one obtains two equations which facilitate the determination of $\bar{V}$ for a complete range of initial rise parameters. The symmetric and antisymmetric mode relations are, respectively

$$\left.\begin{aligned} \bar{V}^{\frac{3m-1}{2}} q_{lnu_{cr}} - \bar{V}^{\frac{m-1}{2}} e_{nu} - \left(\frac{1}{2}\right)\left[(\bar{V}^{m-1} e_{nu}^2 - 4)/3\right]^{\frac{3}{2}} = 0 \\ \bar{V}^{\frac{3m-1}{2}} q_{lnu_{cr}} - \bar{V}^{\frac{m-1}{2}} e_{nu} - 3\left[\bar{V}^{m-1} e_{nu}^2 - 16\right]^{\frac{1}{2}} = 0 \end{aligned}\right\} \quad (34)$$

From these two equations, Equation 34, plots of $\bar{V}$ versus $\frac{1}{\rho}$ are obtained, for n = 2 and $\frac{1}{2}$ and m = 2 and 3, as shown in Figures 3.22 through 3.27. Figures 3.22 through 3.24, for m = 2, correspond to initial rise parameters of 4.20, 10 and 30, respectively. These initial rise parameters are chosen in order to provide knowledge of the entire range of values by considering low, intermediate and high initial rise parameters. For e = 4.20, the maximum weight savings occurs at moderate nonuniformity, corresponding to about five per cent for n = $\frac{1}{2}$ and four per cent for n = 2. As the value of the initial rise parameter increases the maximum weight savings decreases and occurs at extreme nonuniformity, for both n values, as shown in Figures 3.23 and 3.24.

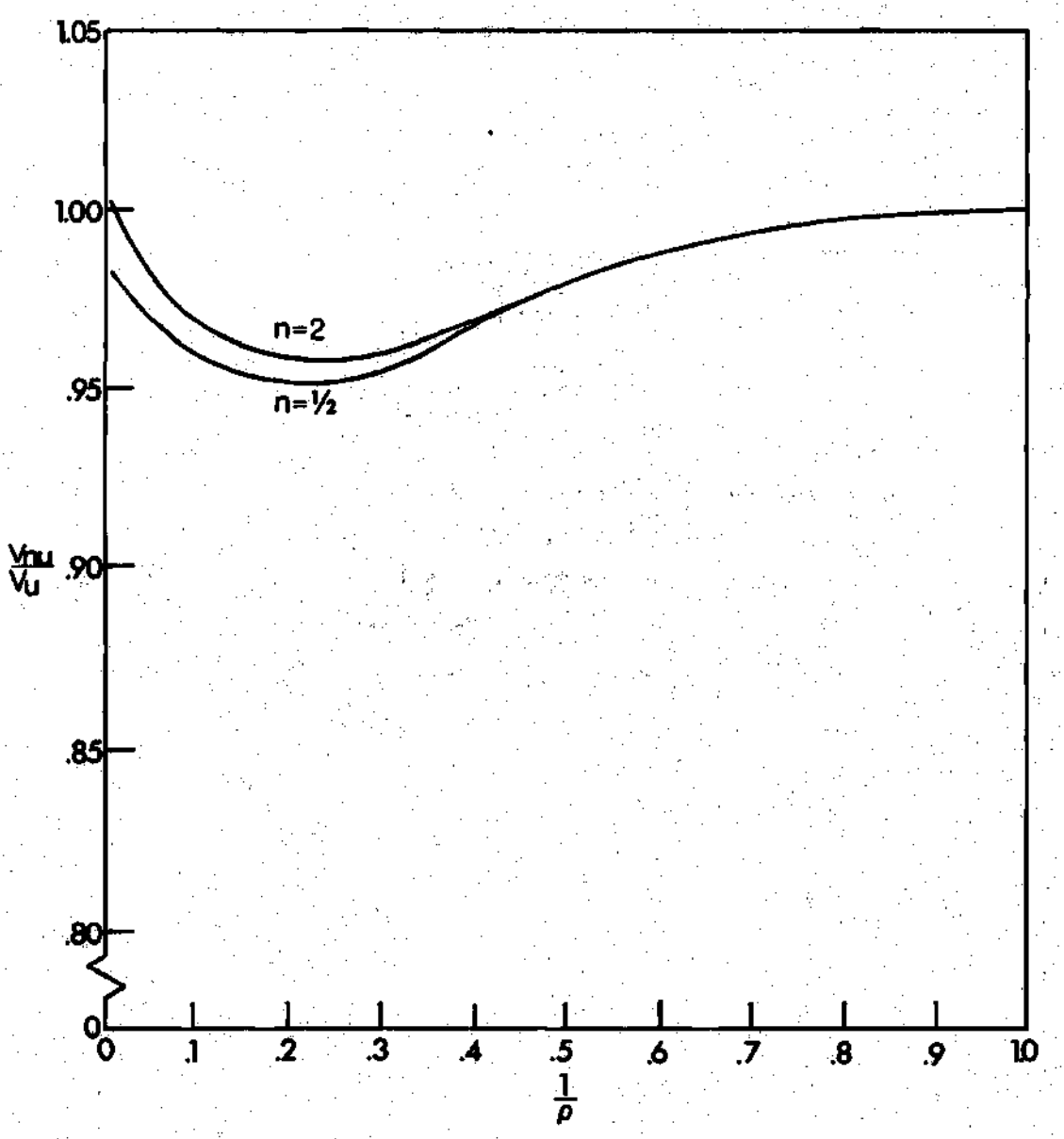

Figure 3.22 Ratio of Nonuniform to Uniform Volume versus the Ratio of Arch End Inertias to Arch Center Inertias, e = 4.20, m = 2, n = 2,1/2.

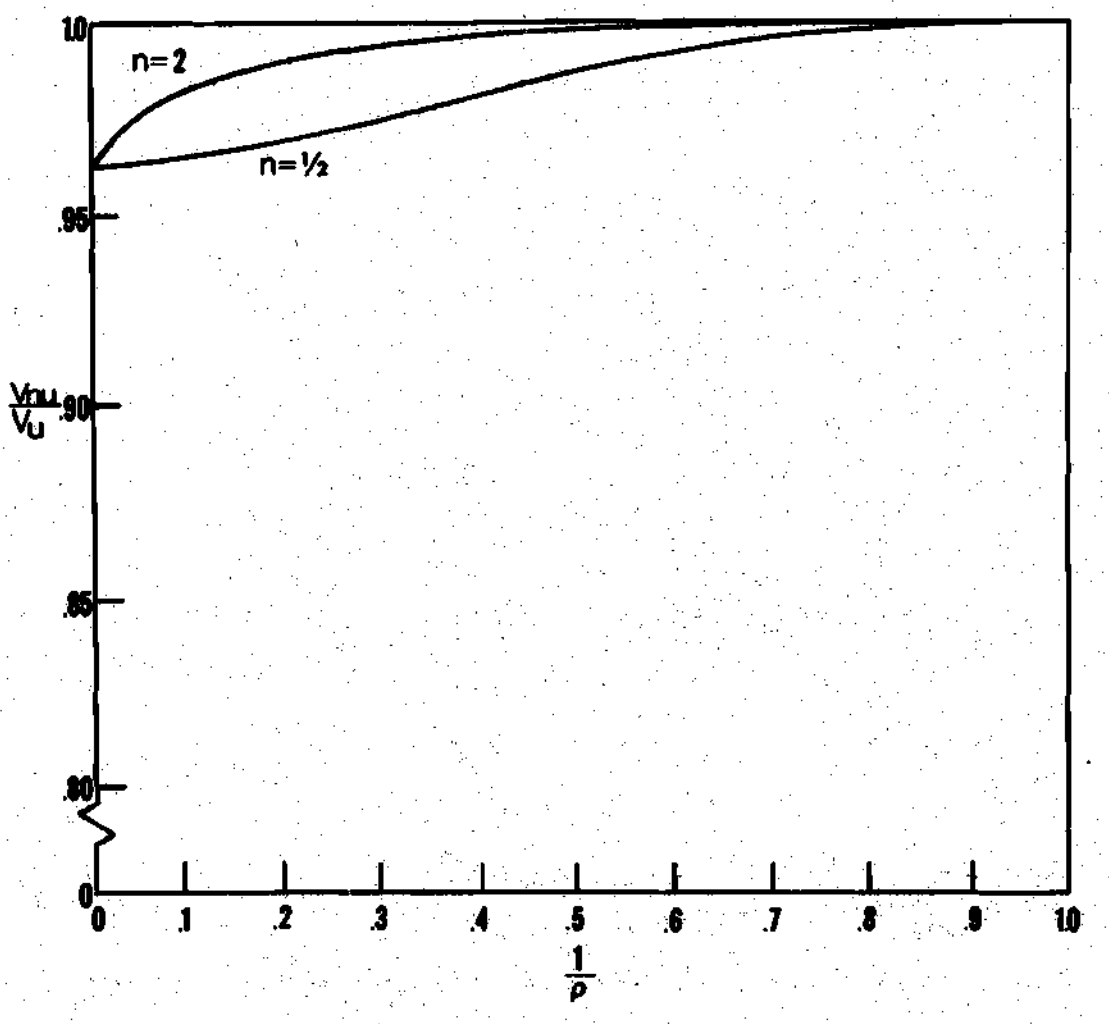

Figure 3.23 Ratio of Nonuniform to Uniform Volume versus the Ratio of Arch End Inertias to Arch Center Inertias, e = 10, m = 2, n = 2,1/2.

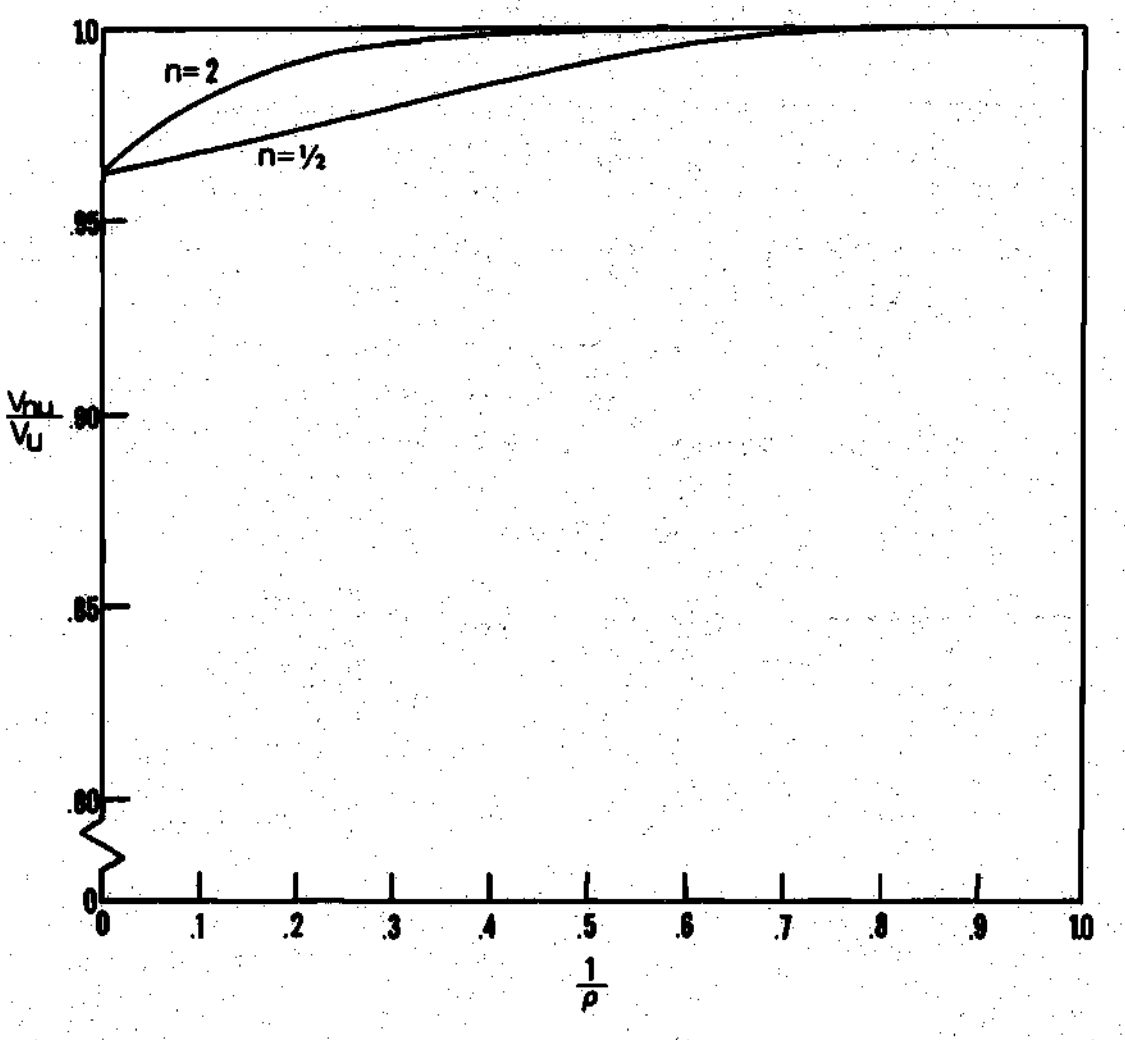

Figure 3.24 Ratio of Nonuniform to Uniform Volume versus the Ratio of Arch End Inertias to Arch Center Inertias, e = 30, m = 2, n = 2,1/2.

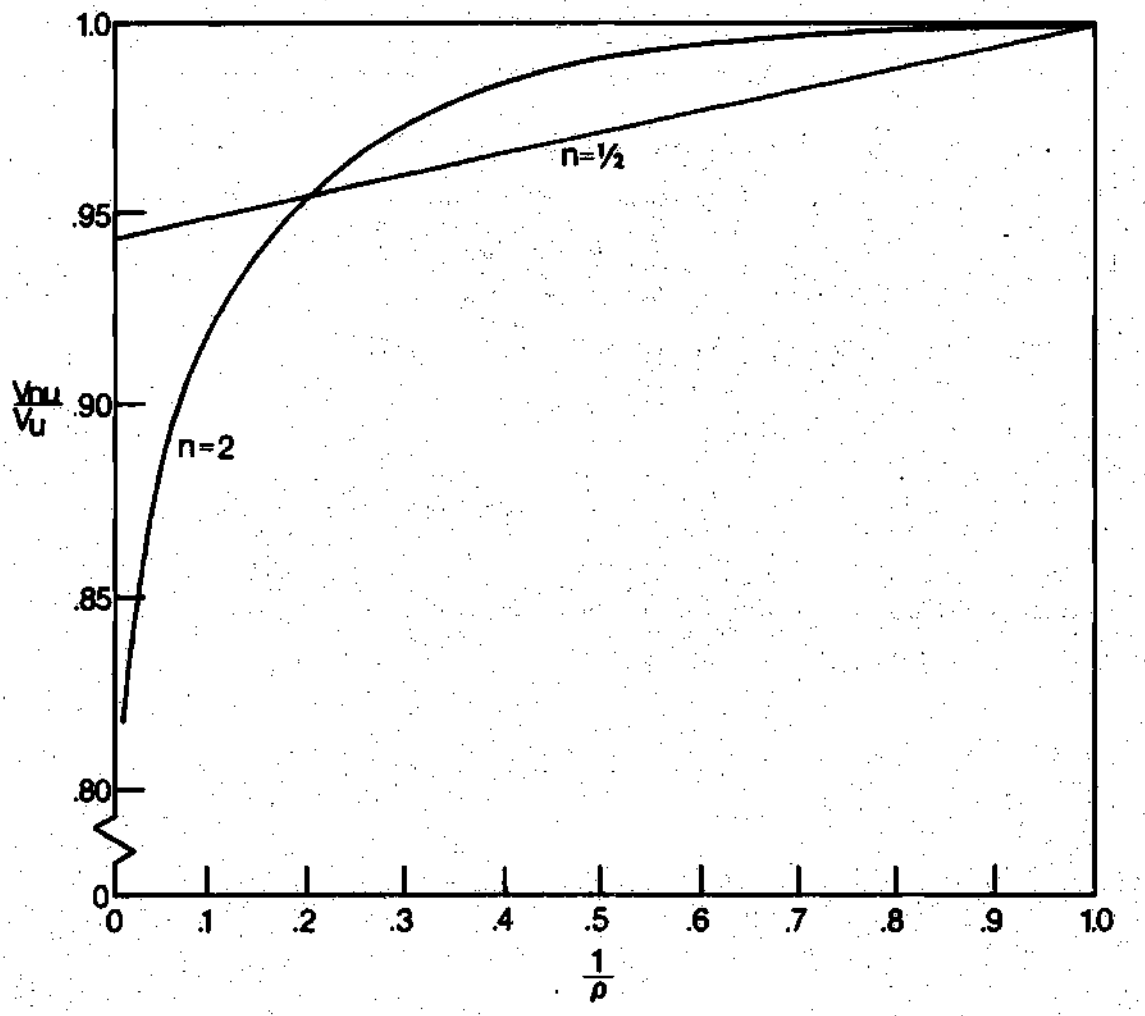

Figure 3.25 Ratio of Nonuniform to Uniform Volume versus the Ratio of Arch End Inertias to Arch Center Inertias, e = 3.485, m = 3, n = 2,1/2.

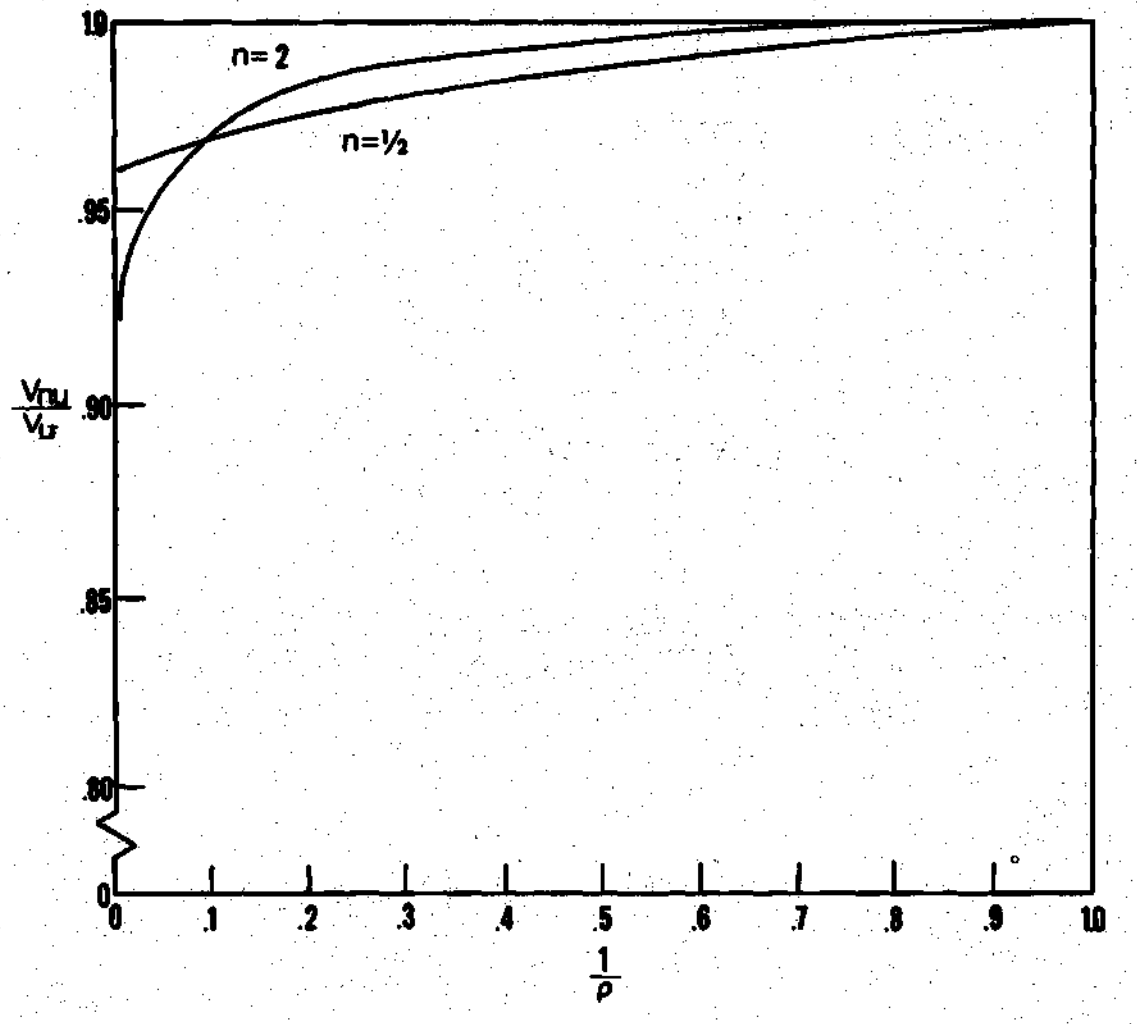

Figure 3.26 Ratio of Nonuniform to Uniform Volume versus the Ratio of Arch End Inertias to Arch Center Inertias, e = 10, m = 3, n = 2,1/2.

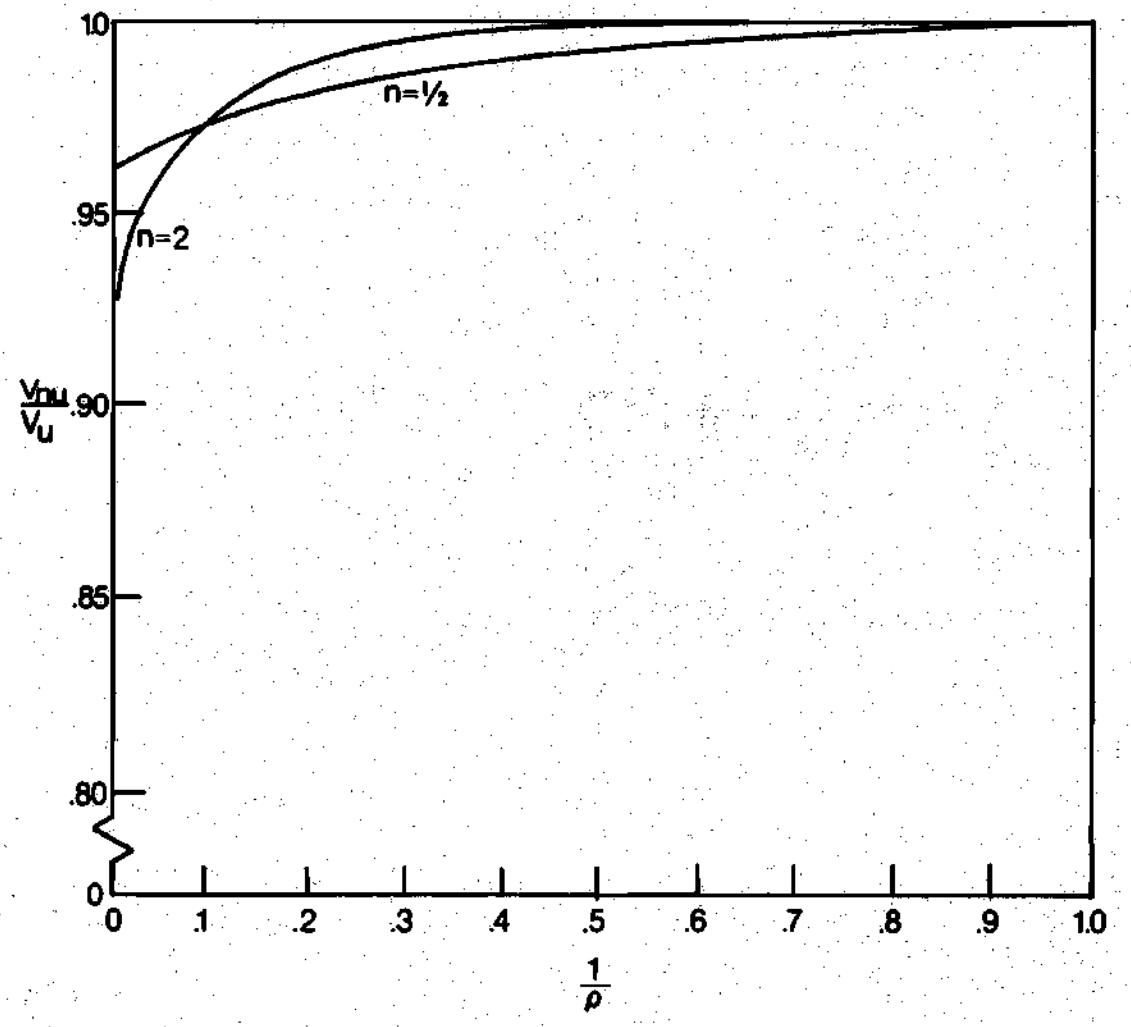

Figure 3.27 Ratio of Nonuniform to Uniform Volume versus the Ratio of Arch End Inertias to Arch Center Inertias, e = 30.0, m = 3, n = 2,1/2.

Weight savings for e = 10 is only slightly better than at e = 30. Figures 3.25 through 3.27 show graphically $\bar{V}$ versus $\frac{1}{\rho}$ for m = 3 and initial rise parameters of 3.485, 10 and 30, respectively. For all initial rise parameters and both n values, the maximum weight savings occurs at extreme nonuniformity. These figures show a proportional decrease in weight savings for increasing initial rise parameters. Also, for m = 3, n = 2 geometries yield greater weight savings than n = $\frac{1}{2}$. The weight savings, for n = 2, varies from about seven per cent to 20 per cent for high to low initial rise parameters.

3.6 Concluding Remarks

The previous results are summarized by certain concluding remarks. First, the approximate technique is quite accurate. For m = 1, the uniform arch is stronger than the nonuniform arch for n = 2 and the opposite is true for n = $\frac{1}{2}$ except for very low initial rise parameters. As m increases, for both n values, the nonuniform arch becomes stronger. The best weight savings occurs at low initial rise parameters. Overall, n = $\frac{1}{2}$ geometries yield the best weight savings for m = 1 and 2. Geometries, for n = 2, yield the best weight savings for m = 3. The maximum weight savings realized for n = 2 is about 20 per cent and about five per cent for n = $\frac{1}{2}$. Finally, it is observed that the trend in weight savings, for the geometries considered, is the same as those realized for the optimum pinned column investigated in Ref. [20].

CHAPTER IV

APPROXIMATE DYNAMIC SOLUTION

4.1 Introduction

The previous quasi-static treatment is sufficient to enable one to calculate critical loadings against snap-through buckling when the loading is applied slowly. Shallow arches with nonuniform stiffness under dynamic loadings with half-sine spatial distributions are investigated herein.

Geometry of the shallow pinned arch consists of an initial half-sine shape where the inertia varies according to $I(x) = I_1\left(\frac{x}{a}\right)^2$. This distribution is chosen since it yields the best weight savings for an arch, with $m = 3$, under a quasi-static loading. A direct solution to the problem is to solve the governing nonlinear differential equations of motion under specified loadings, initial and boundary conditions for the dynamic response of the structure. This procedure is used by Lock[11] and Fulton and Barton[12]. According to this approach the loading is considered to be critical when the motion (transverse displacement) becomes very large. The present method was first employed in Ref. [10] and it was improved in Ref. [6]. It associates critical conditions with characteristics on the total potential surface, and it is based on the fact that the Hamiltonian of the system is constant.

It is shown that a rectangular step loading may cause buckling for specified critical loadings and release times ranging from zero to

infinity. Moreoever, critical values are bracketed between a minimum possible and minimum guaranteed value. This method has been used successfully for uniform geometry. (See Ref. [6] and [29].).

4.2 General Methods

The three cases of dynamic load application considered herein are constant load of finite duration applied suddenly and its two extreme cases when the release time approaches zero and infinity. The order considered is:

1) Load of constant magnitude and infinite duration.
2) The ideal impulse (Dirac-delta function).
3) Load of constant magnitude and finite duration.

The total potential energy for the above cases is a function of the generalized coordinates, initial rise parameter, the magnitude of the applied loading and structural geometry. Static equilibrium positions are easily located on the total potential surface by using the principle of the stationary value of the total potential energy for the two-mode representation. For the shallow arch considered, the above method yields one, three or five static equilibrium points depending on the initial rise parameter and structural geometry. It should be noted that snap-through is not possible for less than three static equilibrium points. Since the total mechanical energy is conserved for a stationary and conservative system, one obtains $T + U_T =$ Constant. If the initial total potential is defined to be zero, then $T + U_T = T_i$ where T_i is the initial kinetic energy which depends on the initial conditions imposed for the corresponding dynamic case

considered above. Critical values can then be bracketed by considering possible paths on the total potential surface.

For the dynamic case of a load of constant magnitude and infinite duration, the initial kinetic energy (T_1) is zero and $T + U_T = 0$. Since the kinetic energy is positive definite, the only possible positions (motion) on the total potential surface correspond to non-negative kinetic energy. Moreover, where U_T is positive there is no possibility of motion. At this point it is advantageous to present relevant definitions, previously defined in Ref. [6], as follows:

Possible Locus: A possible locus on the total potential surface is one which corresponds at every point of the locus to a non-negative kinetic energy.

Unbuckled Motion: Unbuckled motion of the system is defined as any possible locus on the total potential surface which completely encloses only the near equilibrium points.

Buckled Motion: If the possible locus passes through or encloses other equilibrium points, or if the near equilibrium point becomes unstable, then the motion is defined as buckled.

Minimum Possible Critical Loading (MPCL): The least upper bound of loadings for which all possible loci correspond only to unbuckled motion. At the (MPCL) there exists at least one possible locus on the potential surface which the structure can follow to "snap-through".

Minimum Guaranteed Critical Loading (MGCL): The greatest lower bound of loadings for which no possible locus corresponds to unbuckled

motion.

It is possible to investigate the total potential surface as the applied loading increases from zero. At some small loading, q_I, the motion about point A is stable. This is shown in Figure 4.1 for the potential surface consisting of three static equilibrium points and in Figure 4.2 for the case of five static equilibrium points. Where five static equilibrium points exist, there is the possibility of antisymmetric motion. As the loading is increased the total potential surface changes until, at q_{II}, the motion is buckled. See point B in Figure 4.1b and point D in Figure 4.2b. Thus, snap-through may start symmetrically and then exhibit transient antisymmetric motion or it may begin snap-through in an antisymmetric mode. Whichever is the case, the first loading at which snapping can occur is defined as the minimum possible critical loading denoted by (MPCL). For solely symmetric deformation snap-through is guaranteed at the (MPCL). For the possibility of an antisymmetric mode, it is shown that the (MPCL) and the (MGCL) do not coincide. The (MGCL) is determined at q_{IV}, see Figure 4.2d, where the saddle points D and E just coincide with the near stable static equilibrium point A. Hence, for the possibility of an antisymmetric mode one can only bracket the critical loading between the (MPCL) and the (MGCL).

For the ideal impulsive loading the approach is the same as for the load of constant magnitude and infinite duration except for different initial conditions. It is assumed that every material particle is instantaneously accelerated to a finite velocity before any displacement can occur. The applied loading is then released after this

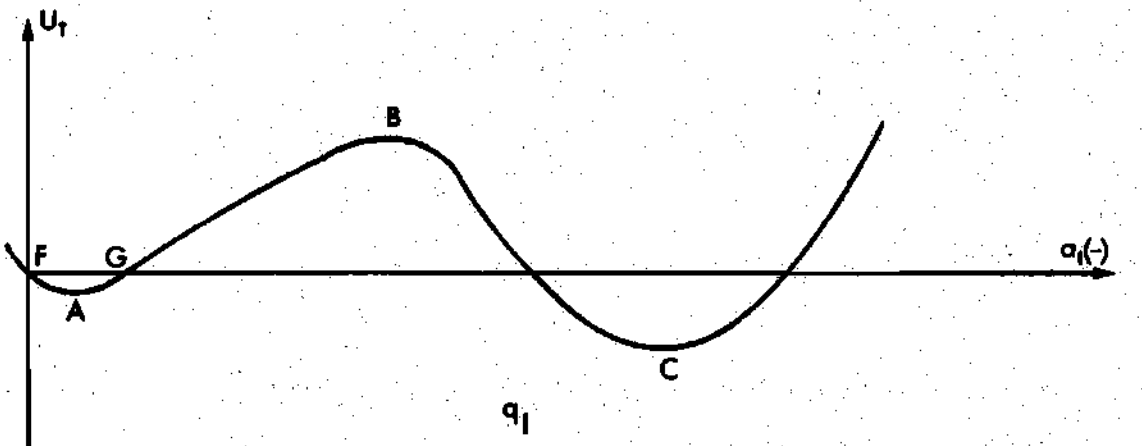

Figure 4.1a

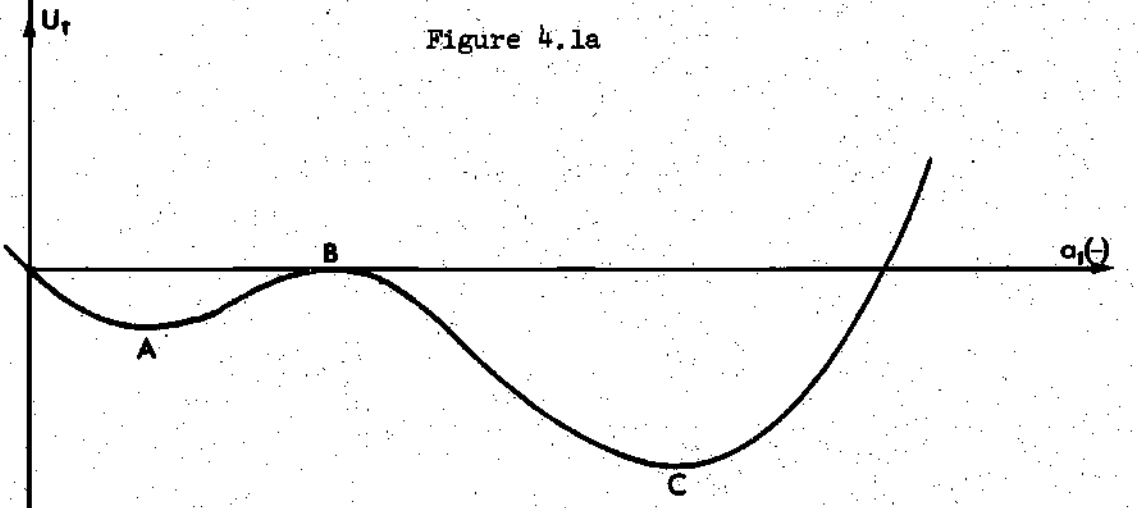

Figure 4.1b

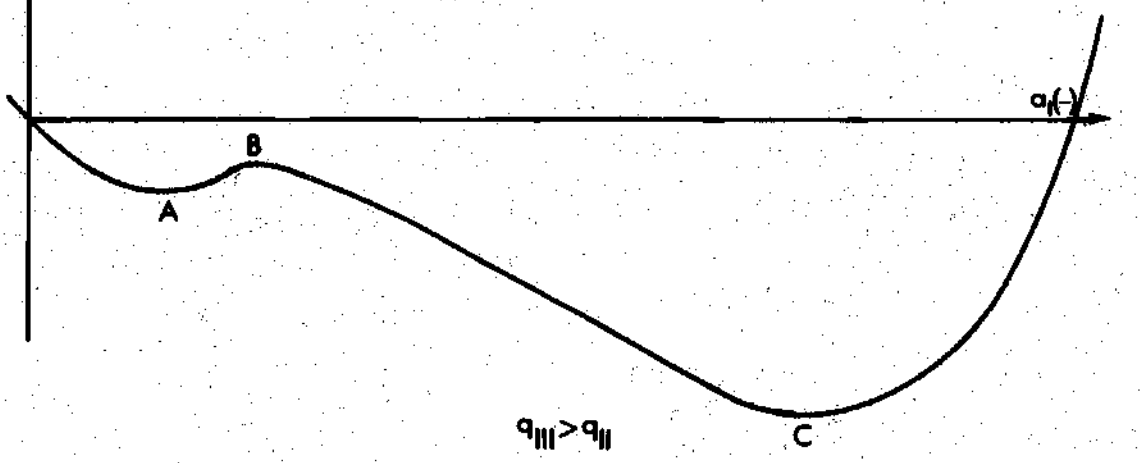

Figure 4.1c

Figure 4.1 Total Potential Curve in the Configuration Space of the Generalized Coordinate a_1.

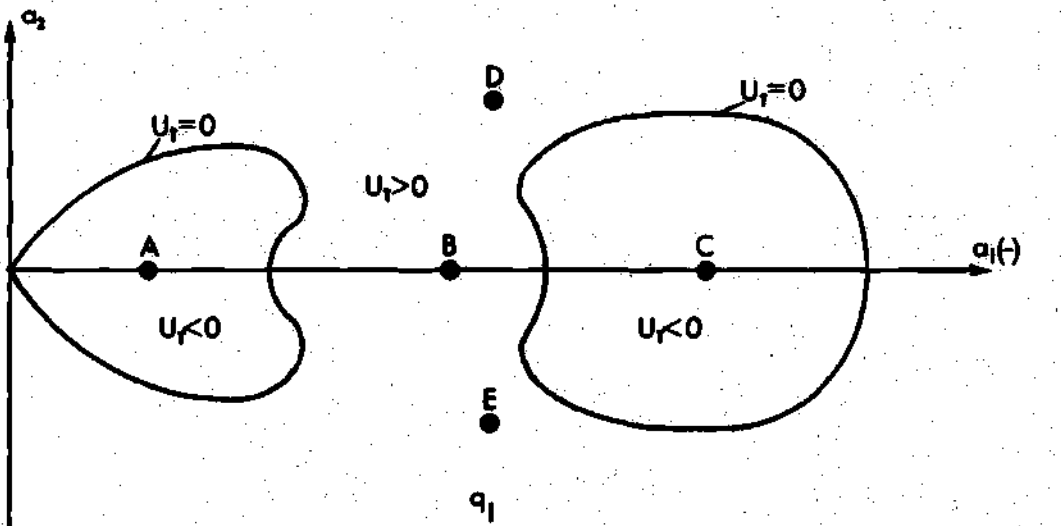

Figure 4.2a

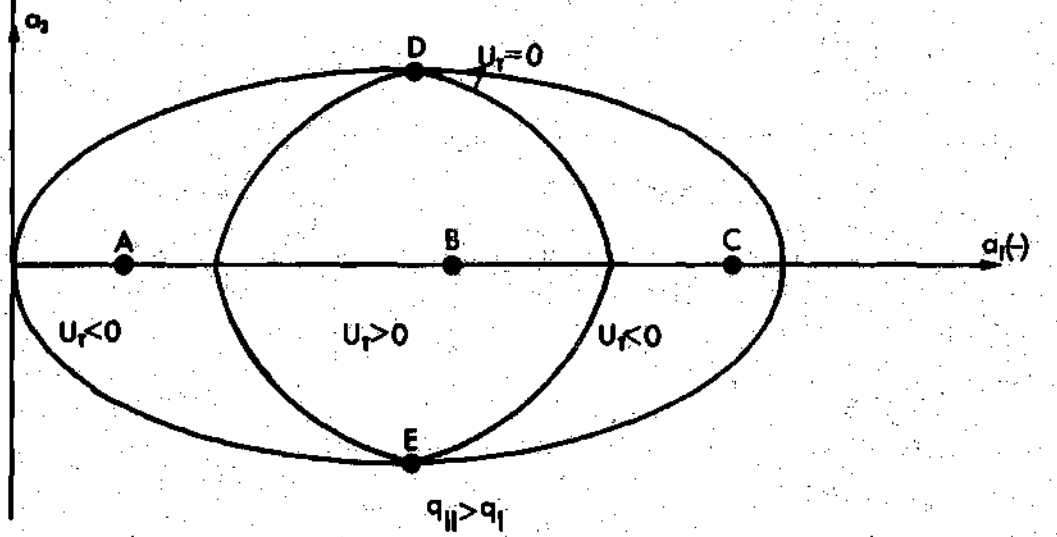

Figure 4.2b

Figure 4.2 Total Potential Contour Lines in the Configuration Space of the Generalized Coordinates a_1 and a_2.

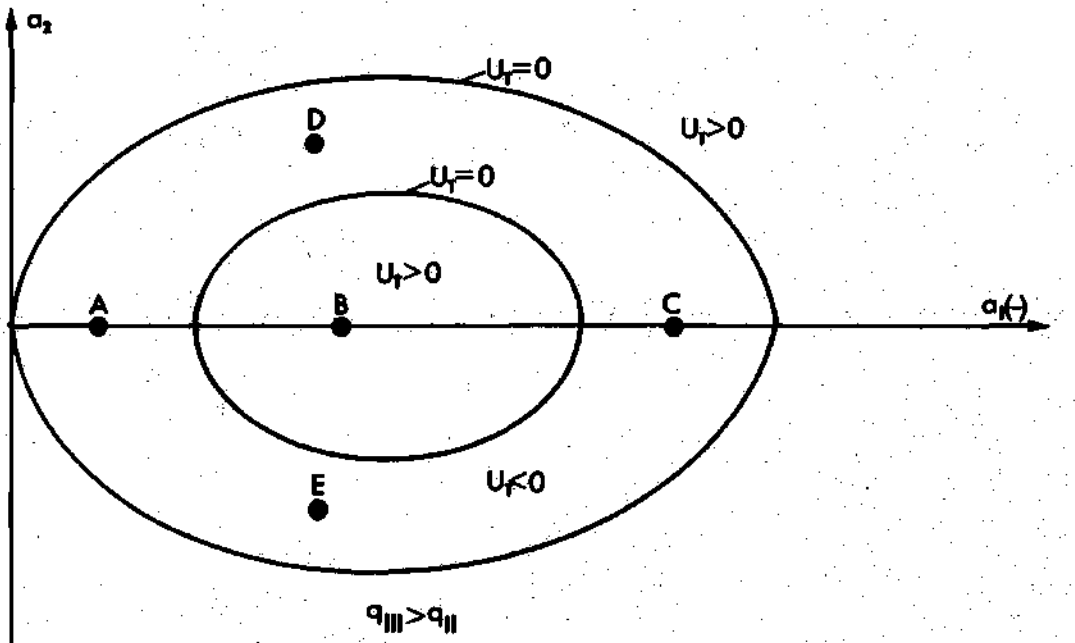

Figure 4.2c

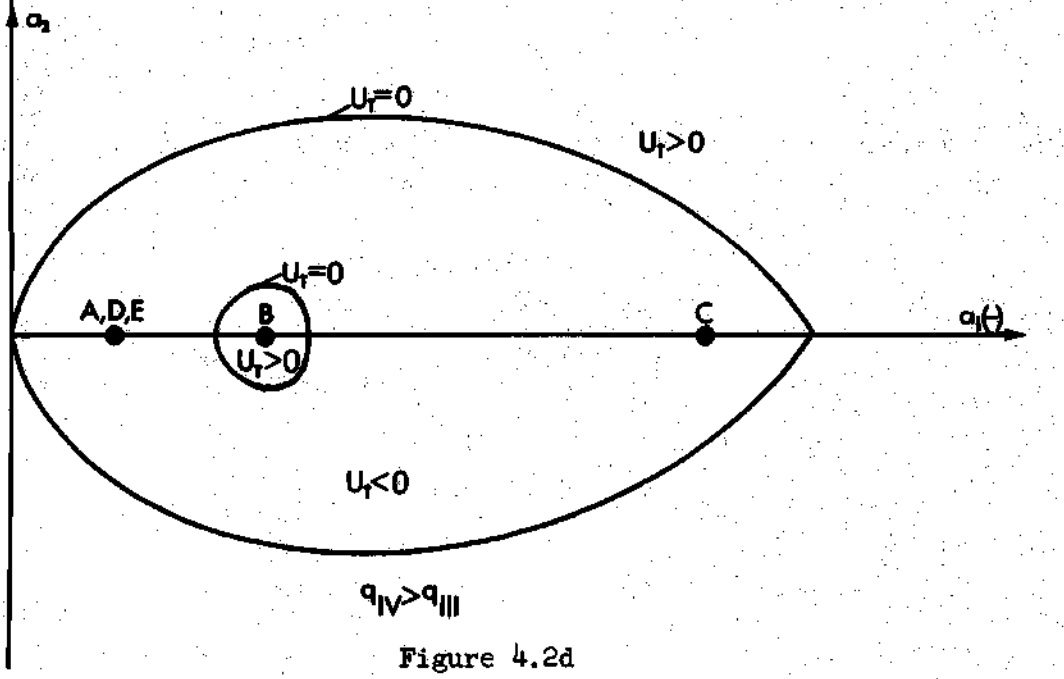

Figure 4.2d

Figure 4.2 Total Potential Contour Lines in the Configuration Space of the Generalized Coordinates a_1 and a_2.

initial condition is reached. This is a close approximation for a blast loading of high decay rate and a short decay time. The initial kinetic energy is related to the initial impulsive energy, and the conservation of mechanical energy is again considered. It is subsequently shown that if a great enough impulse is imparted into the arch initially, snap-through will result for a certain range of initial rise parameters. This value is defined to be the minimum possible critical impulse. The minimum guaranteed critical impulse is determined by finding the initial impulse necessary to cause the structure to overcome the highest potential, namely that of the central unstable equilibrium position.

The critical conditions for the case of a loading of constant magnitude and finite duration consist of a critical time as well as a critical magnitude. A path of steepest descent and most shallow ascent is assumed. This critical path depends on structural geometry, initial rise parameter, and loading magnitude as well as the generalized coordinates. This path is analogous to the one realized by a ball, under constant gravitational force, rolling on such a potential surface. This path is assumed to yield the minimum possible critical values of all possible paths. The constrained equation of motion is solved though integration in closed form over the corresponding path. The critical condition for snap-through is reached when enough kinetic energy is gained, for a given loading, to cause the arch to go to the far zero-load stable equilibrium position. This occurs when the zero-load total potential less the loaded total potential, at the release coordinates, equals the zero-load total potential at its saddle point. This

can easily be seen by again considering conservation of mechanical energy. The critical impulse is the product of the critical loading and the critical release time (T_o).

4.3 Solution

4.3a Load of Constant Magnitude and Infinite Duration

The total potential energy is

$$U_T = \frac{\varphi g_m}{h_m}(r_1^2 - e^2 + 4a_2^2)^2 + \frac{8(\rho^{\frac{1}{2}}-1)^2}{\pi h_m}[(r_1-e)^2\omega - 8a_2^2\psi] + 2q_1(r_1-e)$$

Static equilibrium equations are obtained by using the principle of the stationary value of the total potential which yields

$$\left[r_1^2 + 4a_2^2 - e^2 + \frac{4\omega(\rho^{\frac{1}{2}}-1)^2}{\pi g_m \varphi}\right]r_1 = \frac{4\omega e(\rho^{\frac{1}{2}}-1)^2}{\pi g_m \varphi} - \frac{q_1 h_m}{2g_m \varphi}$$

$$\left[r_1^2 + 4a_2^2 - e^2 - \frac{8\psi(\rho^{\frac{1}{2}}-1)^2}{\pi g_m \varphi}\right]a_2 = 0$$

Again, the existence of three or five equilibrium points depends on structural geometry and the initial rise parameter. For

$$\sqrt{4\omega(\rho^{\frac{1}{2}}-1)^2/g_m\pi\varphi} < e \leq \sqrt{-8\psi(\rho^{\frac{1}{2}}-1)^2/\pi g_m\varphi}$$

there are three static equilibrium points r_{11}, r_{12}, r_{13} corresponding to symmetric buckling and for

$$e \geq \sqrt{-8\psi(\rho^{\frac{1}{2}}-1)^2/\pi g_m\varphi}$$

there are five equilibrium points including antisymmetric mode saddle points. The second subscript on r_1 represents the near, center and far static equilibrium positions, respectively (or r_{11}, r_{12}, r_{13}).

The total potential corresponding to purely symmetric buckling is a function of r_1, e and q_1, where the static equilibrium point $(r_{12},0)$ is unstable (in the small). As discussed previously, the loading increases until snap-through is possible at $(r_{12},0)$ with zero kinetic energy. Due to zero initial conditions the total potential at $(r_{12},0)$ is equal to zero. Thus one obtains

$$q_{1_{cr}} = [g_m(e-r_{12})/\pi h_m][\pi\varphi(r_{12} + e)^2/2 + 4\omega(\rho^{\frac{1}{2}}-1)^2/g_m] . \qquad (35)$$

Since $(r_{12},0)$ is a static equilibrium point, then

$$q_{1_{cr}} = [g_m(e-r_{12})/\pi h_m][2\pi\varphi\ r_{12}(r_{12}+e) + 8\omega(\rho^{\frac{1}{2}}-1)^2/g_m]$$

and the simultaneous solution of these two equations yields both $q_{1_{cr}}$ and r_{12} as follows:

$$\text{MPCL} = \text{MGCL} = -\ [4\zeta/3\pi h_m]\left[\pi g_m\varphi\left(\frac{2\zeta}{3} + e\right)\left(\frac{2\zeta}{3} + 2e\right) + 4\omega(\rho^{\frac{1}{2}}-1)^2\right] \qquad (36)$$

and

$$r_{12} = e + \frac{2\zeta}{3} \quad \text{where} \quad \zeta = -\ 2e + \sqrt{\frac{e^2}{4} - \left[6\omega(\rho^{\frac{1}{2}}-1)^2/\pi g_m\varphi\right]} .$$

For $e \geq \sqrt{-8\psi(\rho^{\frac{1}{2}}-1)^2/\pi g_m\varphi}$ the total potential depends on r_1, a_2, e, and q_1 as well as the structural geometry. The saddle points and

$(r_{12},0)$ are unstable in the small. As discussed previously, when the loading becomes large enough the value of the total potential at the saddle points becomes zero and snapping is possible. See Figure 4.3 for e = 8. A further increase in the load will eventually cause the saddle points to converge on $(r_{11},0)$ where snap-through is guaranteed. See Figure 4.4 for e = 8. Setting the total potential at the saddle points equal to zero one acquires

$$\text{MPCL} = -[2(\rho^{\frac{1}{2}}-1)^2/h_m]\left[2\psi e + \sqrt{-8\psi(\omega+2\psi)(\rho^{\frac{1}{2}}-1)^2/\pi g_m \varphi}\right] \qquad (37)$$

When the near equilibrium position coincides with the saddle points, the solution of the equilibrium equations with this $(r_{11},0)$ yields the MGCL

$$\text{MGCL} = [8(\rho^{\frac{1}{2}}-1)^2/\pi h_m]\left[\omega e - (\omega + 2\psi)\sqrt{8\psi(\rho^{\frac{1}{2}}-1)^2/\pi g_m \varphi}\right] \qquad (38)$$

which is identical to the antisymmetric quasi-static critical load case. The system will snap-through symmetrically when the total potential at the symmetric unstable point equals zero, while it is positive at the antisymmetric saddle points. This occurs when

$$[\pi\varphi g_m \zeta/6(\rho^{\frac{1}{2}}-1)^2][2\zeta/3 + \bar{e}][2\zeta/3 + 2\bar{e}] + \omega[2\zeta/3 + \bar{e}] +$$

$$- (\omega + 2\psi)\sqrt{\bar{e}^2 + 8\psi(\rho^{\frac{1}{2}}-1)^2/\pi g_m \varphi} = 0 \qquad (39)$$

For this case, MGCL is still given by Equation (36).

Minimum possible and minimum guaranteed critical loadings versus initial rise parameters are shown in Figures 4.5 through 4.10, for m = 1, 2 and 3 and a full range of initial rise parameters

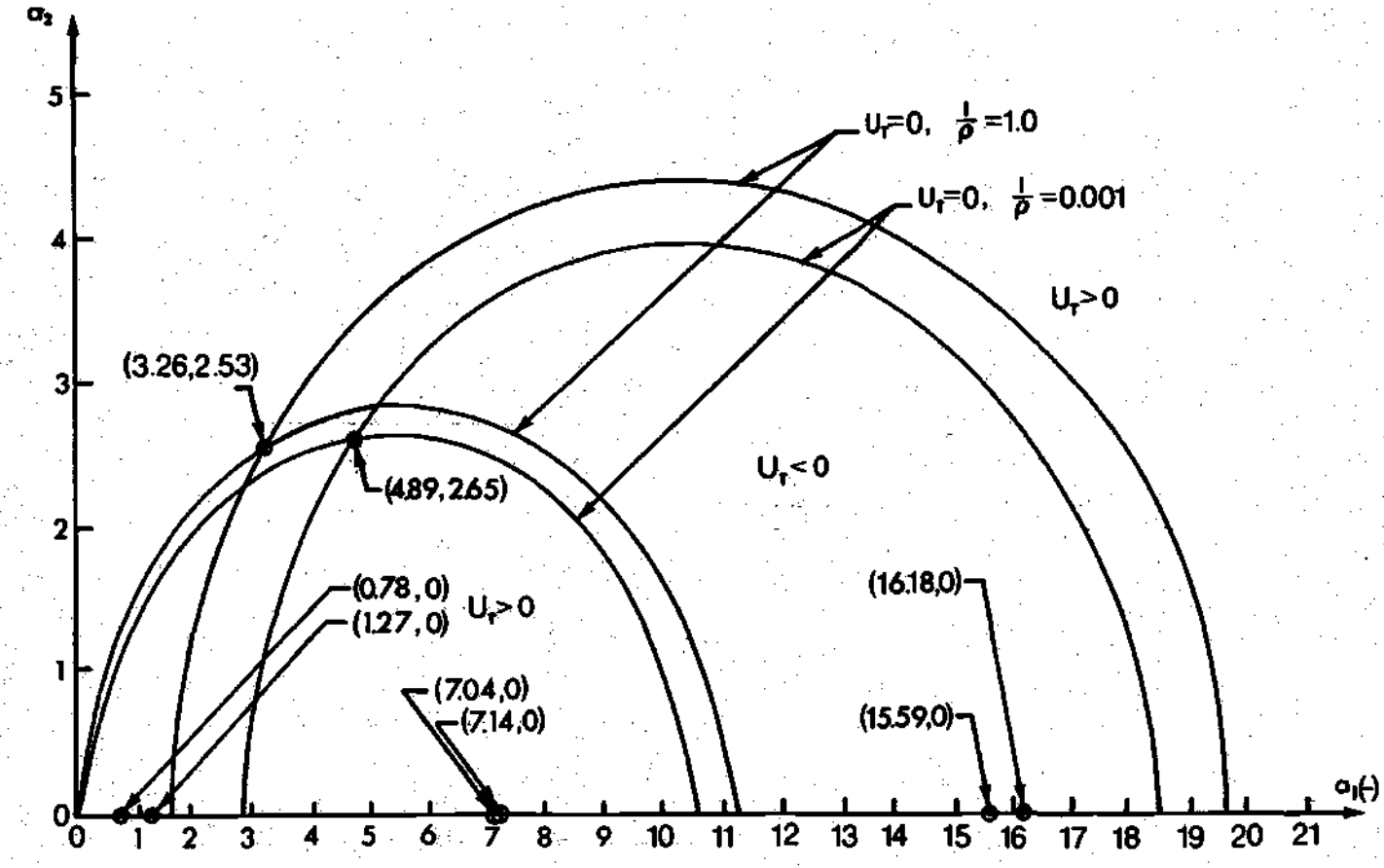

Figure 4.3 Total Potential Contour Lines in the Configuration Space of the Generalized Coordinates a_1 and a_2, $e = 8$, q_{cr} = (MPCL), $m = 3$.

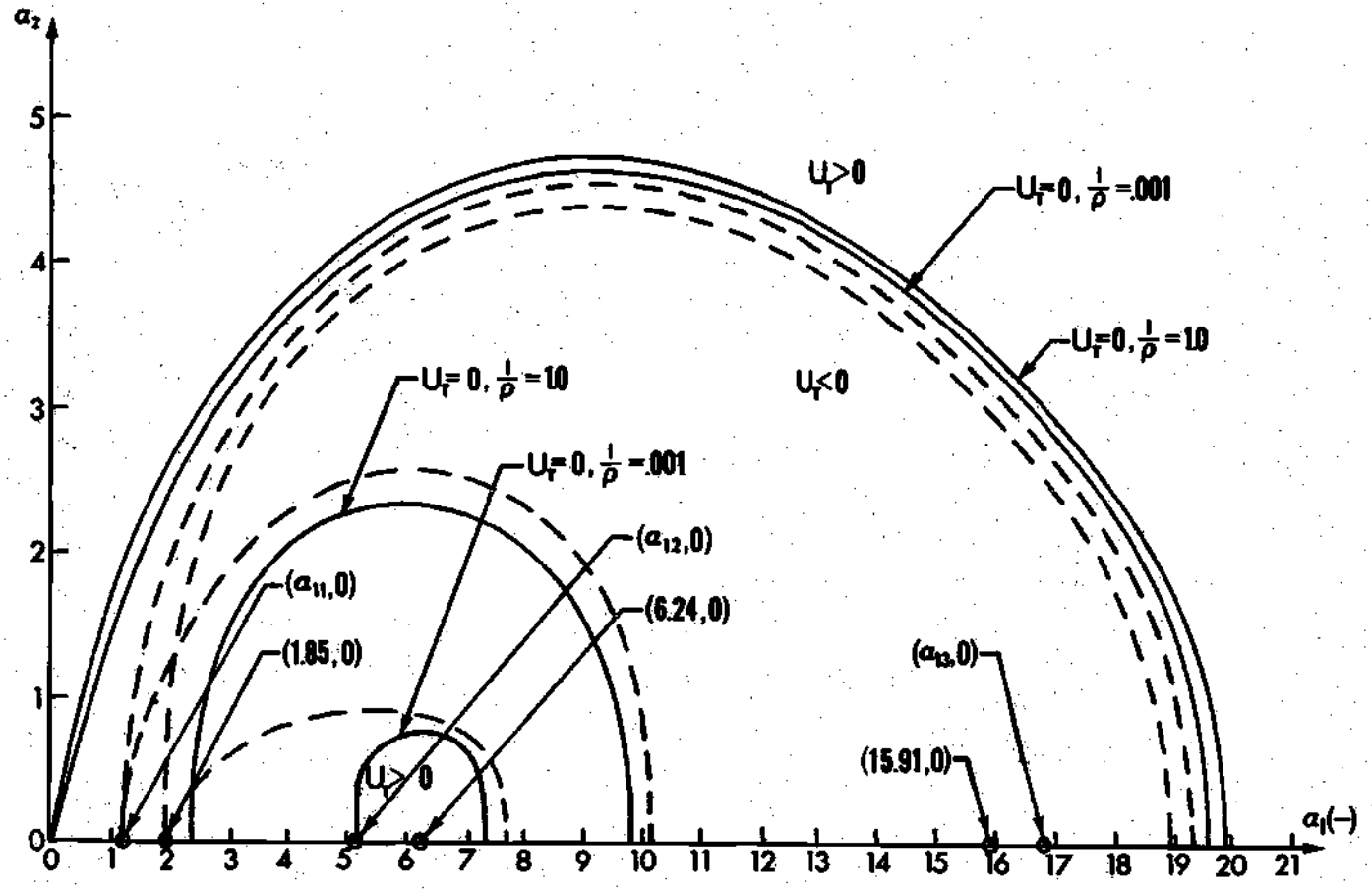

Figure 4.4 Total Potential Contour Lines in the Configuration Space of the Generalized Coordinates a_1 and a_2, e = 8, q_{cr} = (MGCL), m = 3.

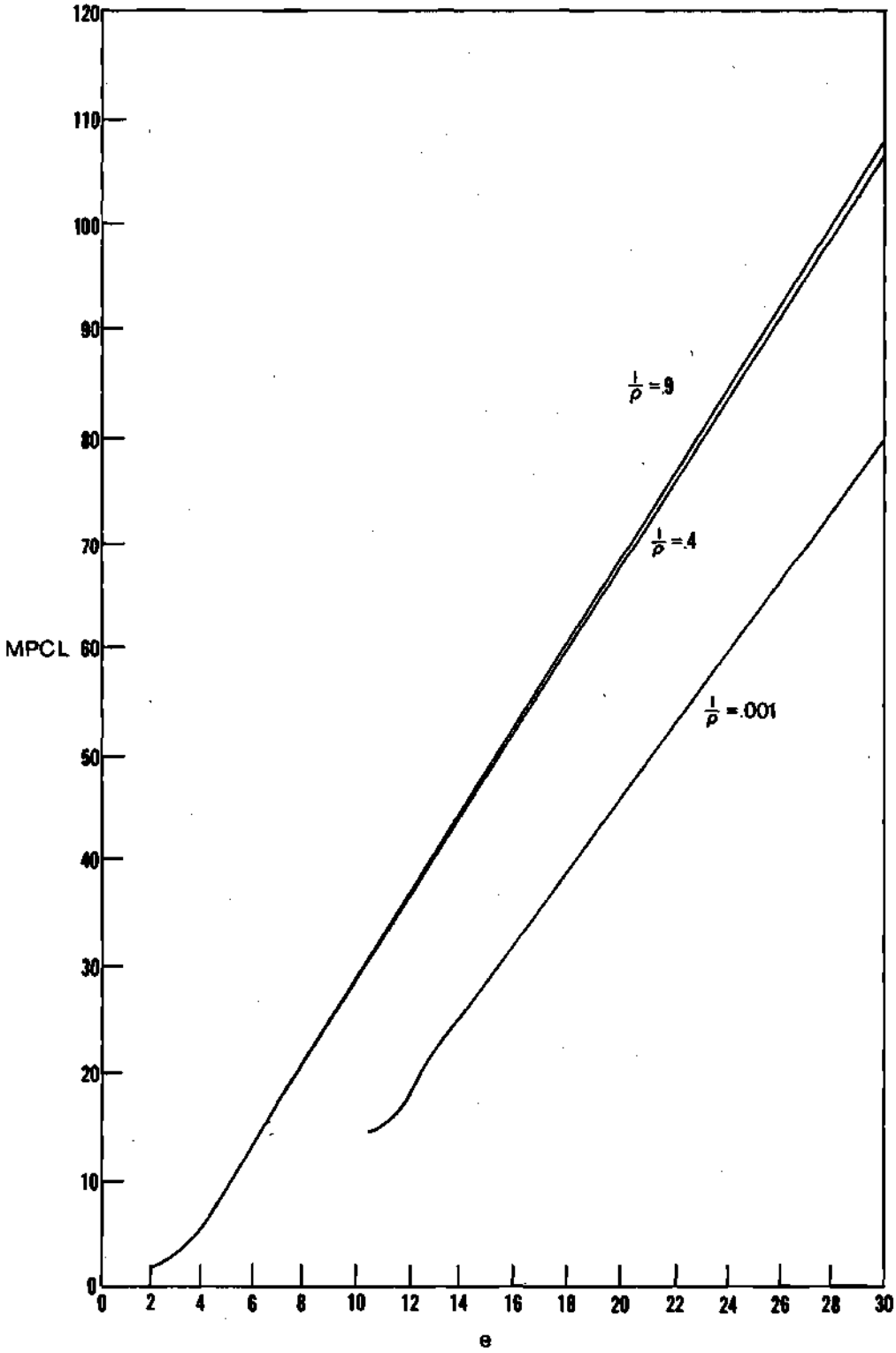

Figure 4.5 Nondimensional Critical Loading versus Initial Rise Parameters, Half-Sine Shape, (MPCL), m = 1.

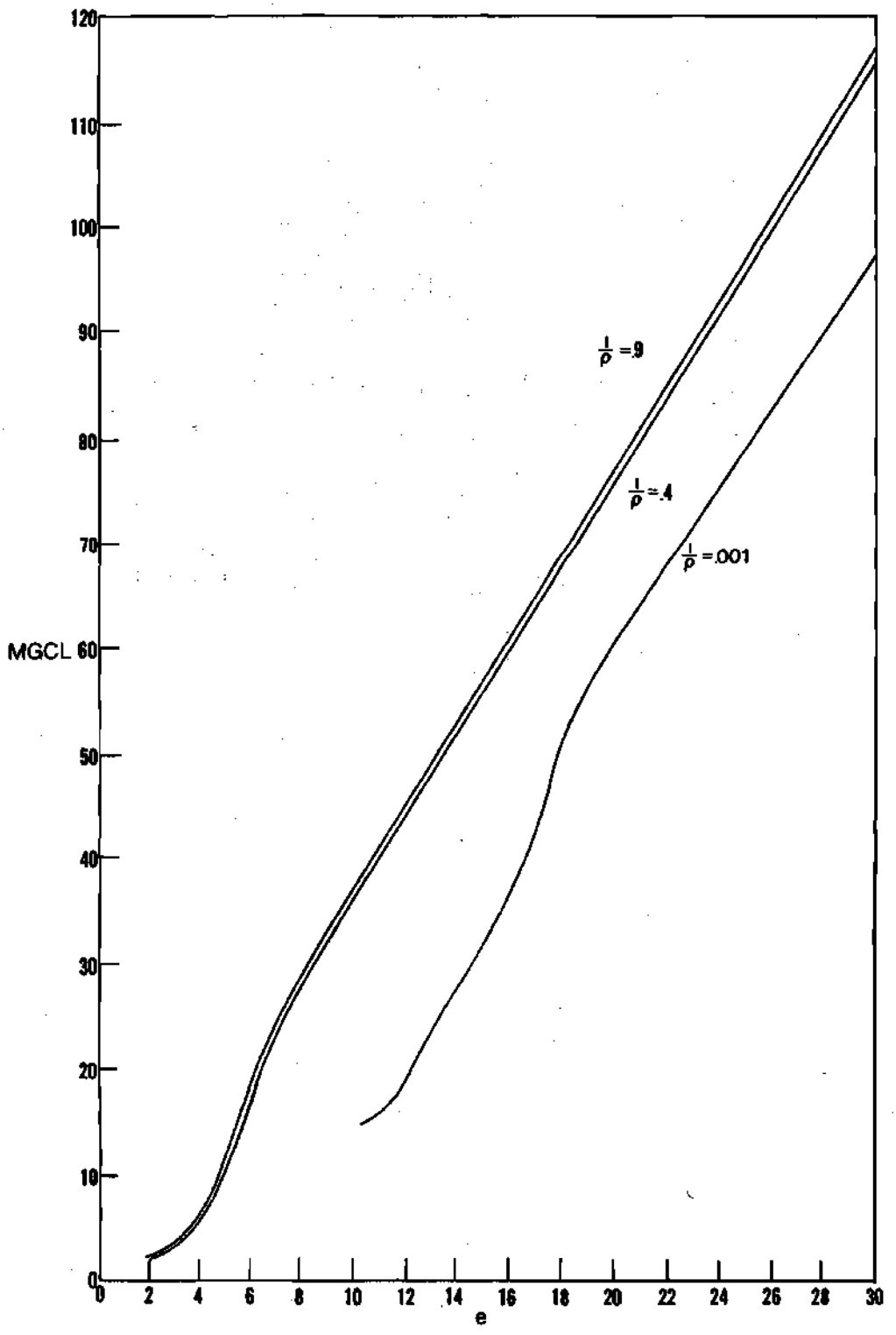

Figure 4.6 Nondimensional Critical Loading versus Initial Rise Parameters, Half-Sine Shape, (MGCL), m = 1.

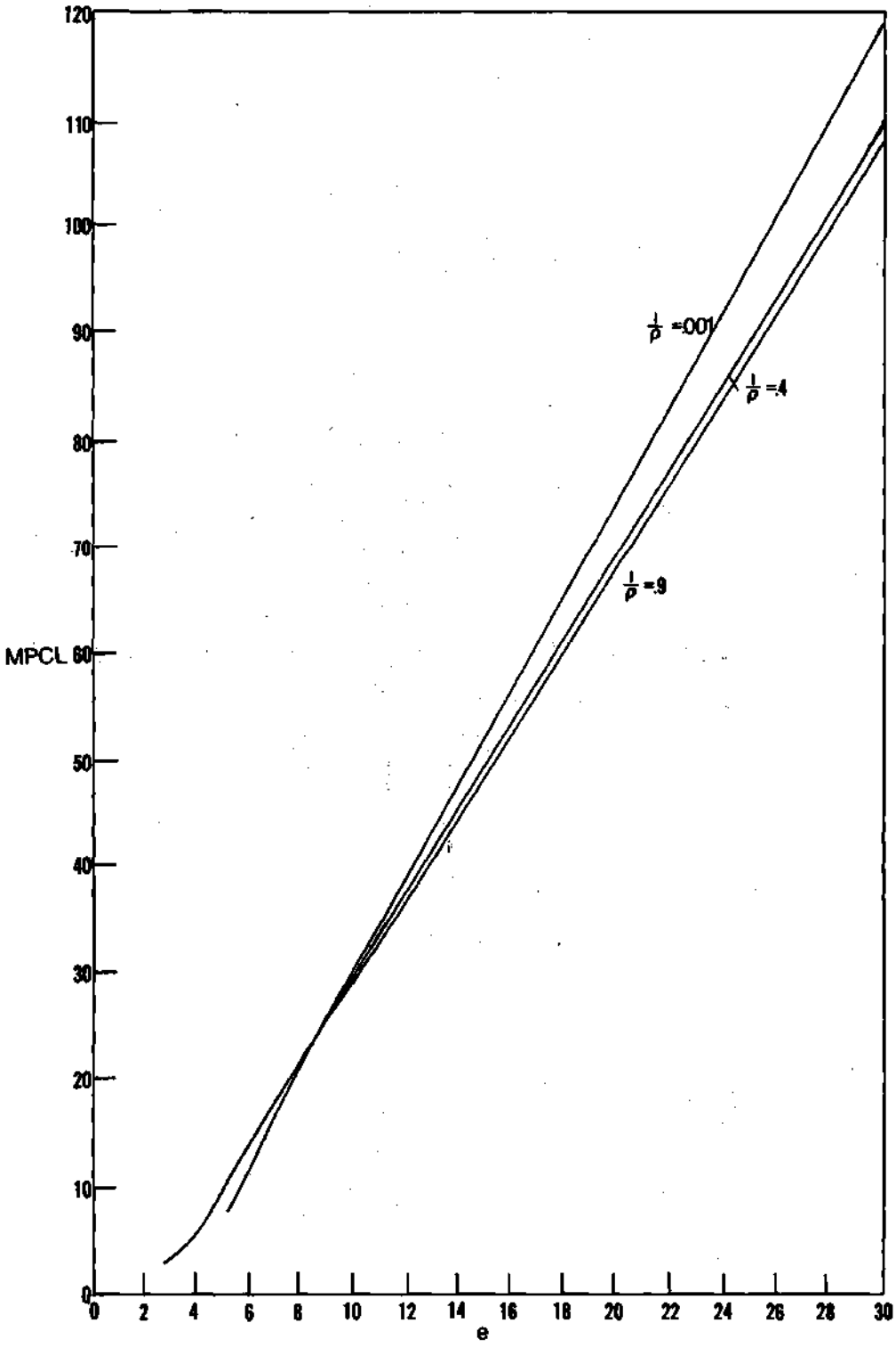

Figure 4.7 Nondimensional Critical Loading versus Initial Rise Parameters, Half-Sine Shape, (MPCL), m = 2.

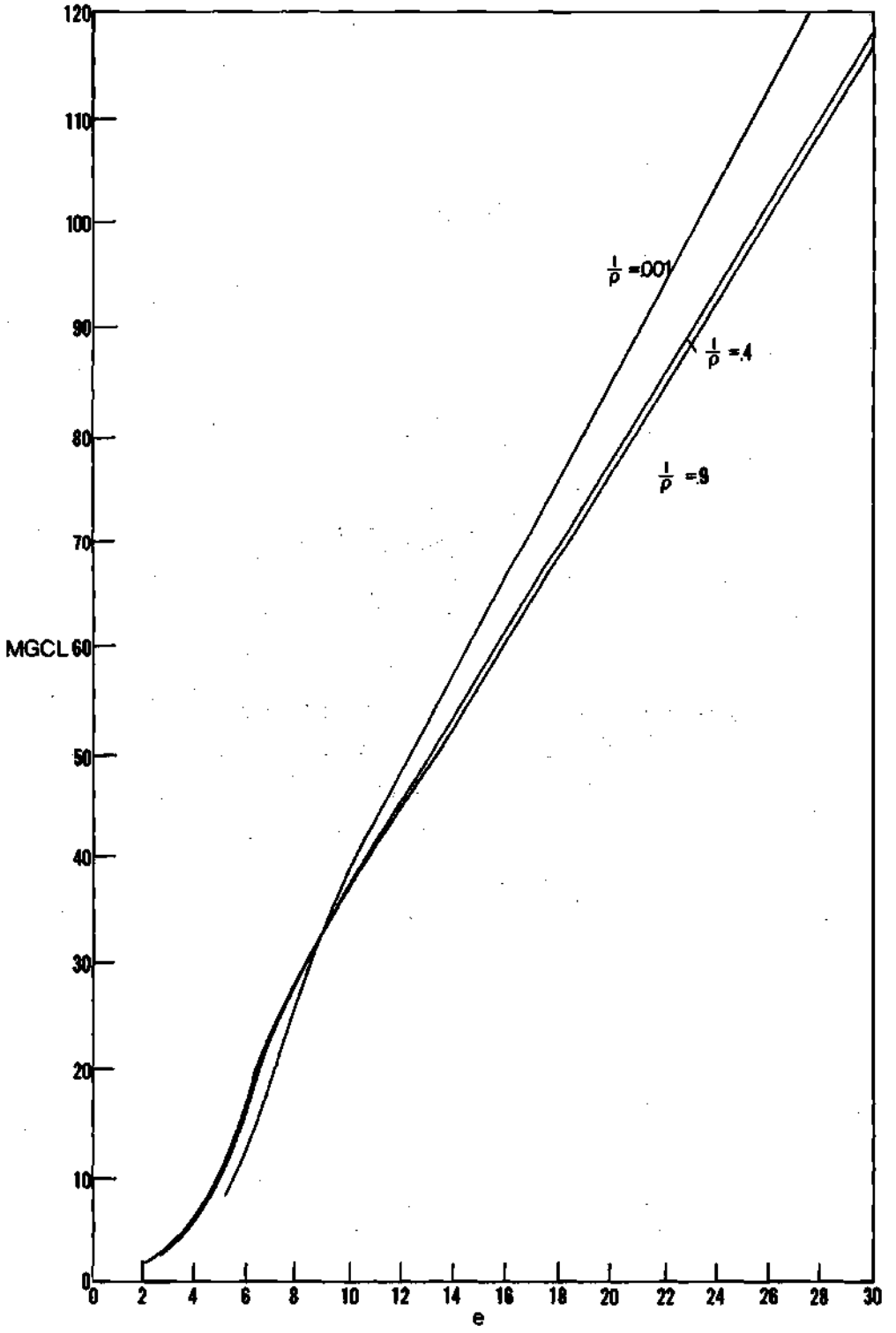

Figure 4.8 Nondimensional Critical Loading versus Initial Rise Parameters, Half-Sine Shape, (MGCL), m = 2.

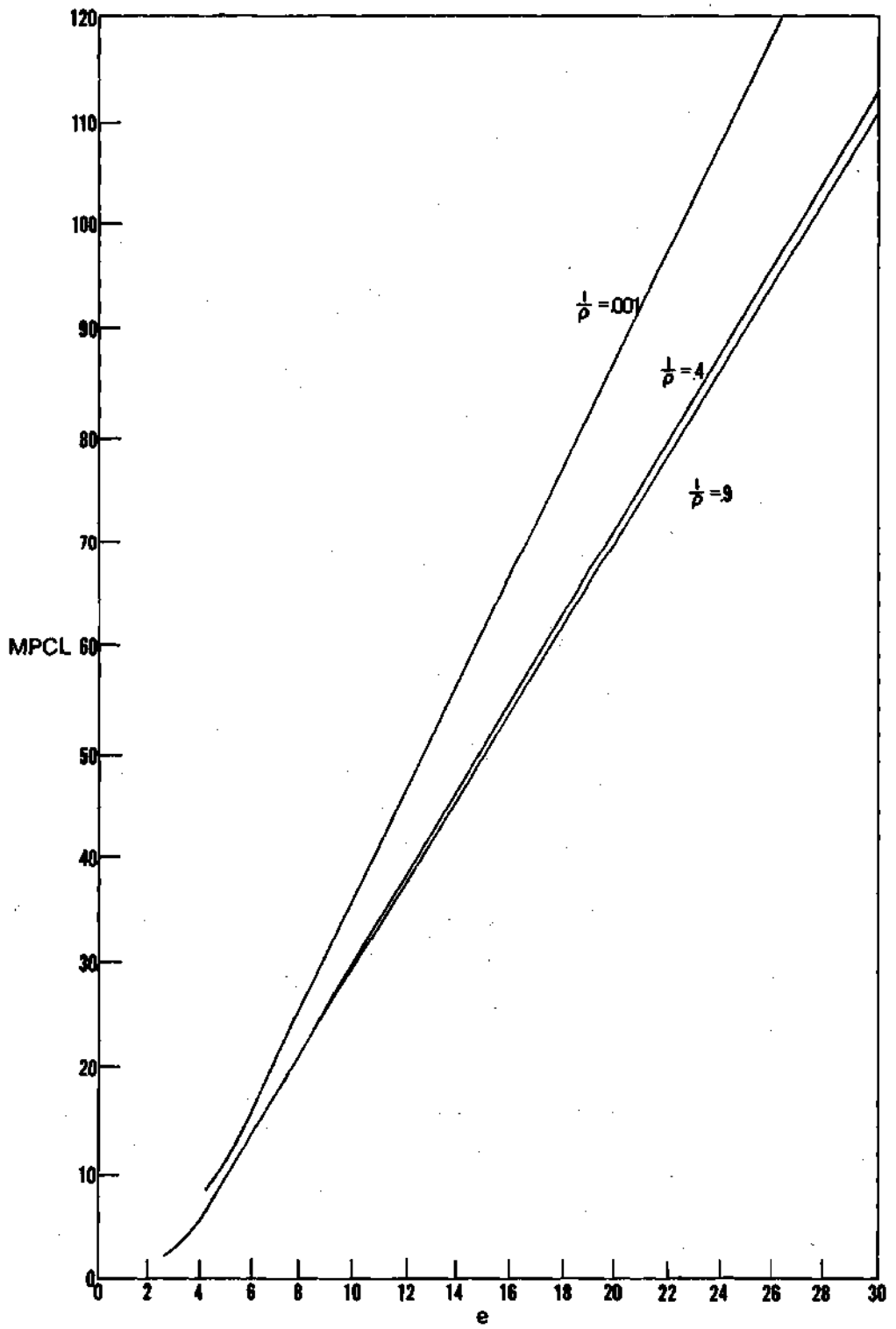

Figure 4.9 Nondimensional Critical Loading versus Initial Rise Parameters, Half-Sine Shape, (MPCL), m = 3.

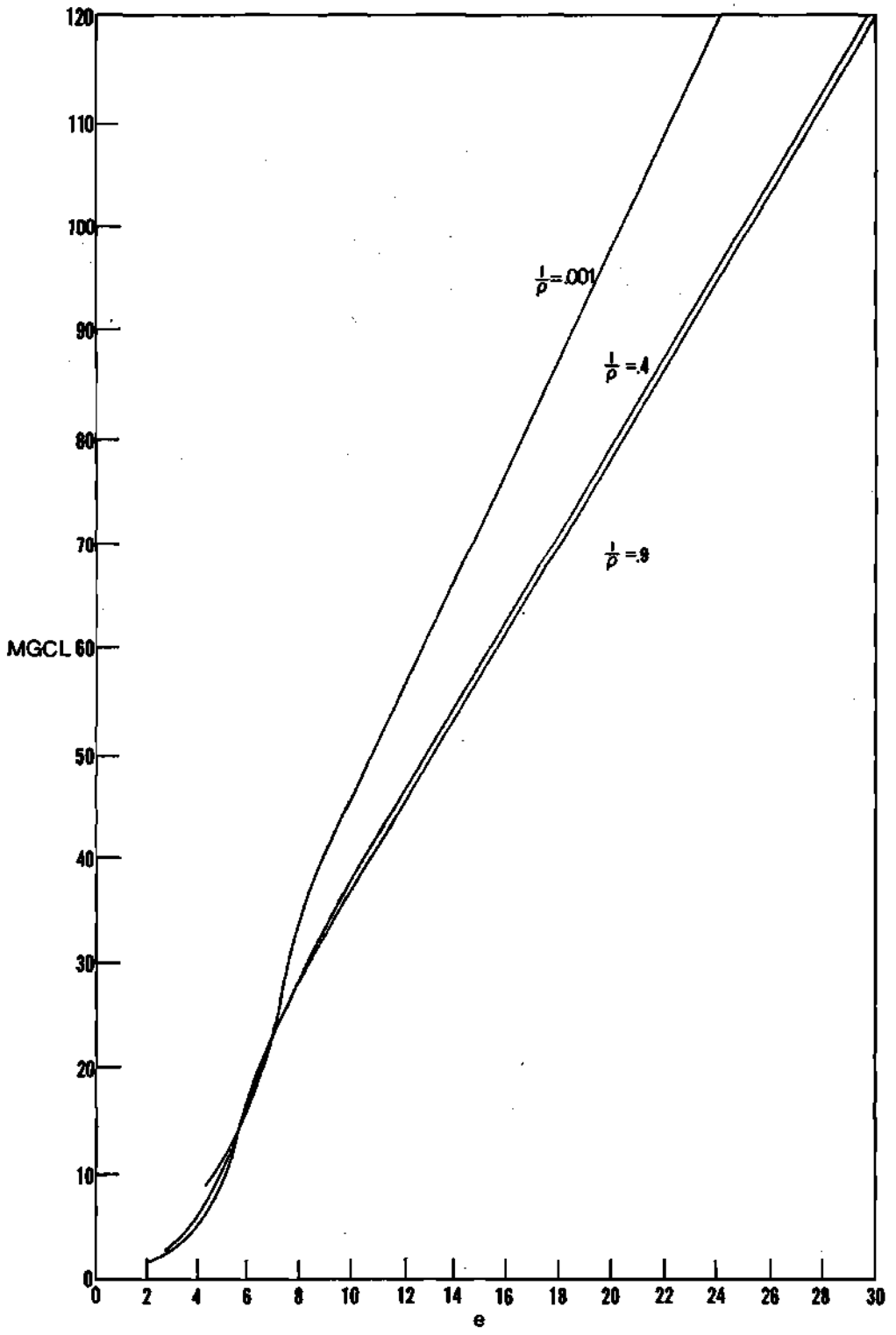

Figure 4.10 Nondimensional Critical Loading versus Initial Rise Parameters, Half-Sine Shape, (MGCL), m = 3.

corresponding to symmetric and antisymmetric buckling. Tables 4.1 and 4.2 give the initial rise parameters corresponding to the limit of applicability of each governing mode. In Figure 4.11 through Figure 4.13 and Tables 4.3 through 4.5, the dynamic ratios versus initial rise parameters, for the minimum possible and the minimum guaranteed critical loadings, are plotted. The dynamic ratios are defined as follows:

$$(DR)_{MP} = MPCL/q_{1_{cr}} \qquad (DR)_{MG} = MGCL/q_{1_{cr}}$$

4.3b Ideal Impulse

For the zero-loading total potential

$$U_T = (2/\pi h_m)\left\{\frac{\pi g_m \varphi}{2}\left[(r_1-e)(r_1+e) + 4a_2^2\right]^2 + 4(\rho^{\frac{1}{2}}-1)^2\left[(r_1-e)^2\omega - 8a_2^2\,\psi\right]\right\}$$

the static equilibrium equations become

$$\left.\begin{aligned}(r_1-e)\left[r_1^2 + e r_1 + 4a_2^2 + 4\omega(\rho^{\frac{1}{2}}-1)^2/\pi g_m\varphi\right] &= 0\\ \left[r_1^2 - e^2 + 4a_2^2 - 8\psi(\rho^{\frac{1}{2}}-1)^2/\pi g_m\varphi\right] a_2 &= 0\end{aligned}\right\} \qquad (40)$$

The first equation yields three possible roots, for $a_2 = 0$, as follows:

$$r_1 = e$$

$$r_1 = \left[-e \pm \sqrt{e^2 - 16(\rho^{\frac{1}{2}}-1)^2\,\omega/\pi g_m\varphi}\right]/2$$

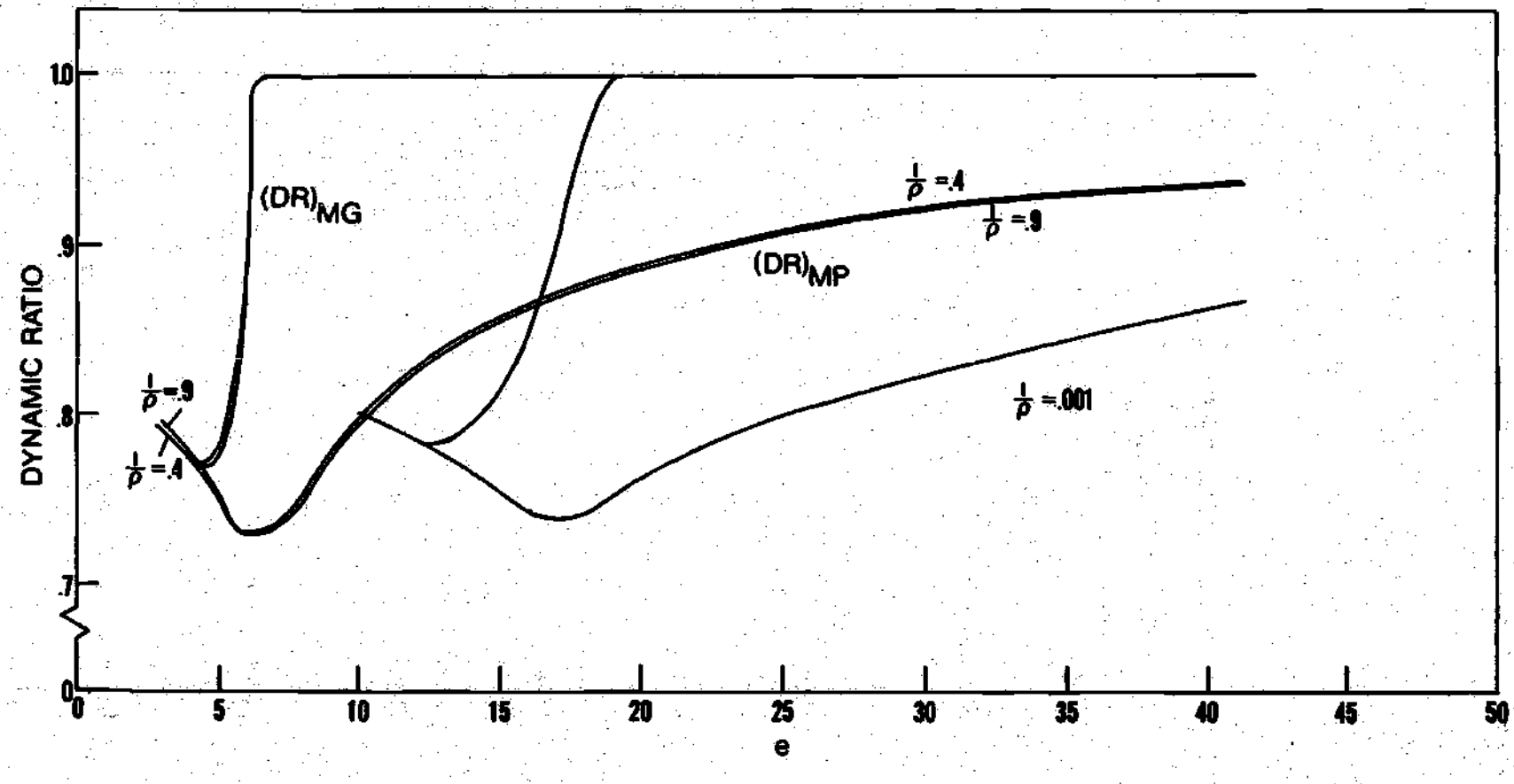

Figure 4.11 Dynamic Ratio versus Nondimensional Initial Rise Parameters, m = 1.

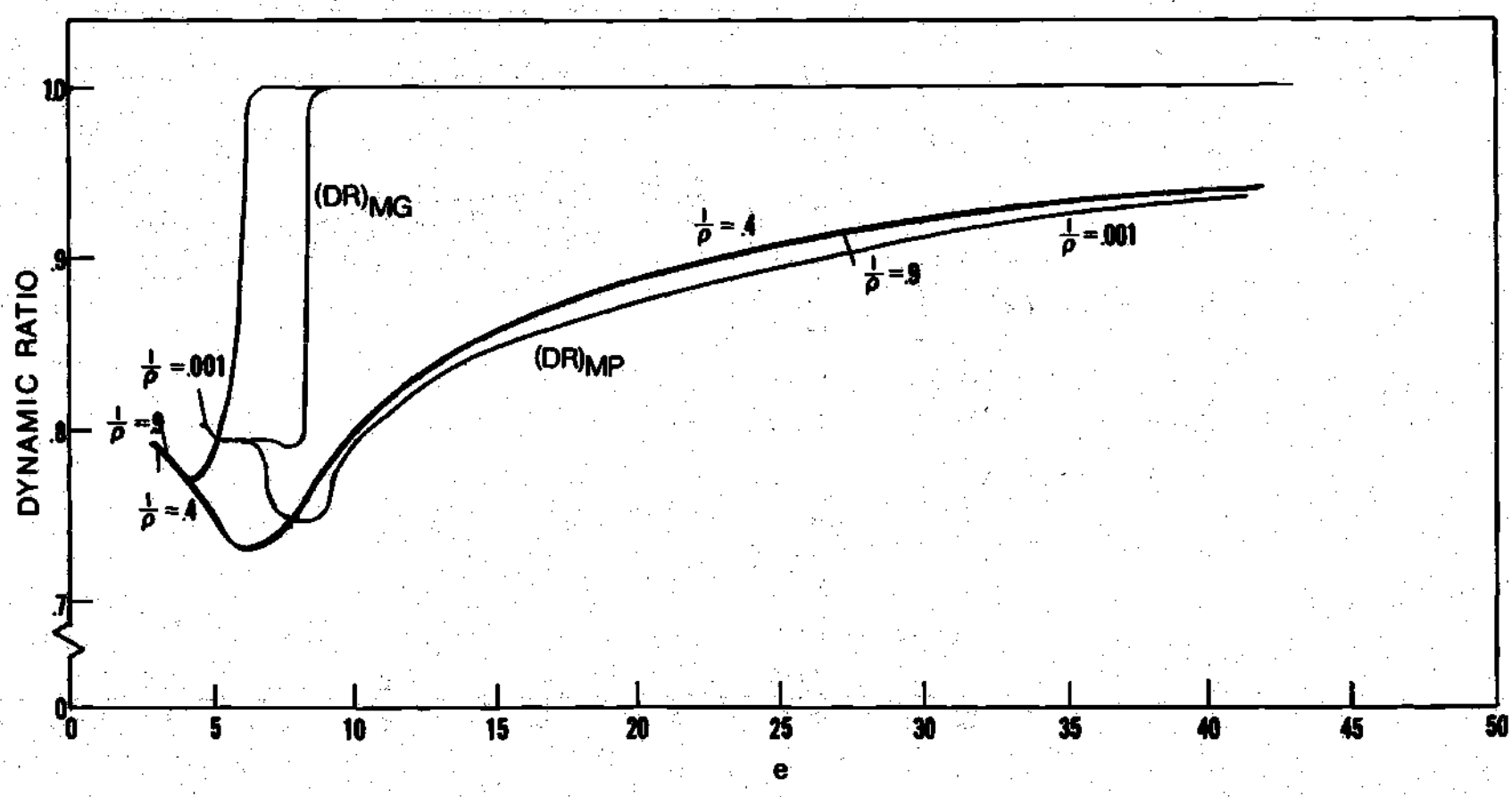

Figure 4.12 Dynamic Ratio versus Nondimensional Initial Rise Parameters, m = 2.

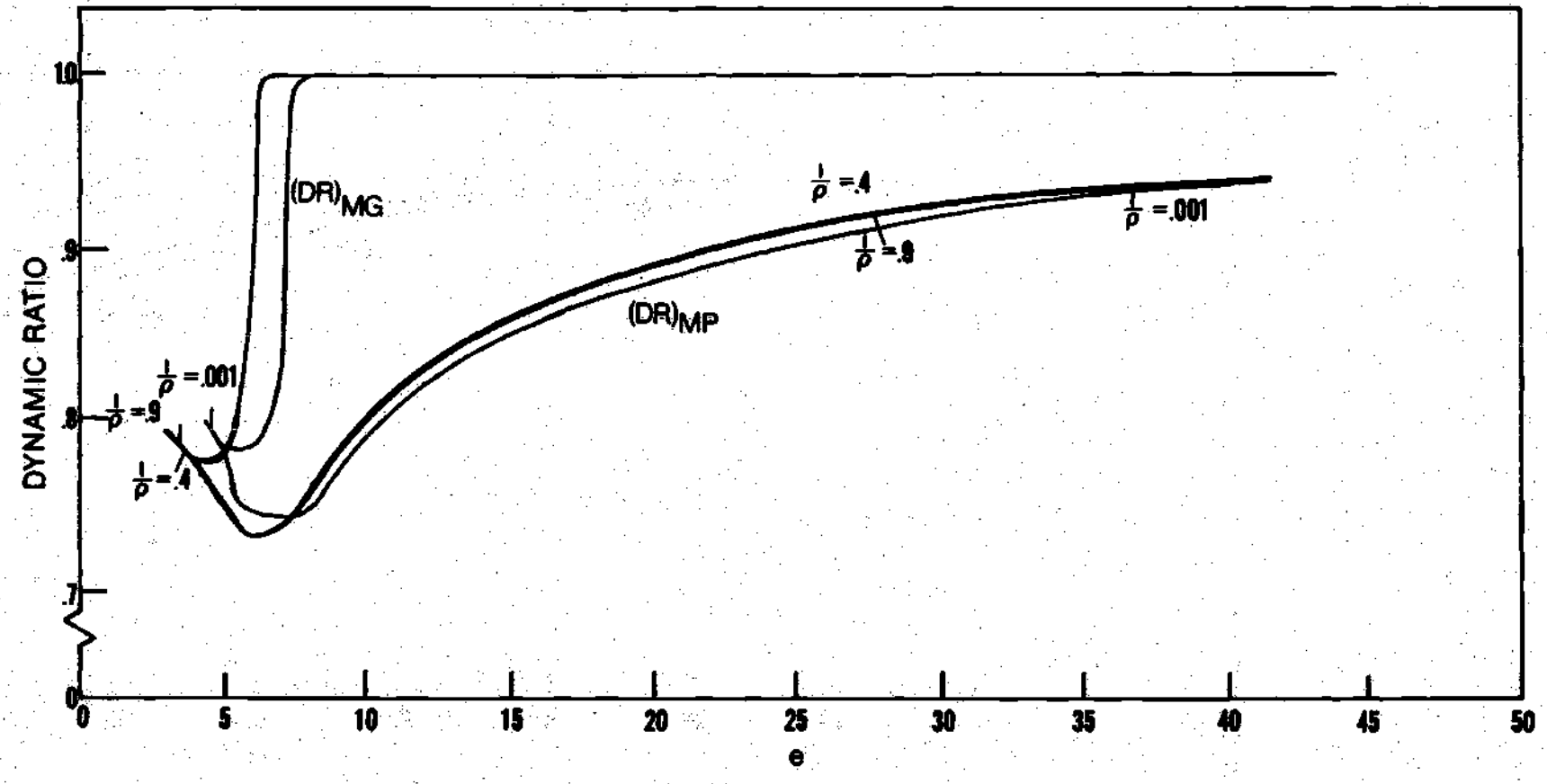

Figure 4.13 Dynamic Ratio versus Nondimensional Initial Rise Parameters, m = 3.

Table 4.1. Initial Rise Parameter Bounds for (MPCL)**
Limit Point Instability, e

I_1/I_2 m =	1	2	3
0.001	10.1842	4.7667	4.2677
	12.2523	5.7347	5.1355
0.400	2.7528	2.7054	2.6996
	4.1183	4.0473	4.0386
0.900	2.4764	2.4756	2.4756
	4.0006	3.9999	3.9970

**The lower limit applies to the (MGCL) as well as the (MPCL).

Table 4.2. Initial Rise Parameter Bound for (MGCL) Antisymmetric Mode Limits.

I_1/I_2 m =	1	2	3
0.001	18.94	8.85	7.92
0.400	6.49	6.40	6.39
0.900	6.36	6.35	6.35

Table 4.3. Dynamic Ratios for the (MPCL), Half-Sine Loading, Initial Half-Sine Shape, m = 1.

I_1/I_2 = .9		I_1/I_2 = .4		I_1/I_2 = .001	
e	$(DR)_{MP}$	e	$(DR)_{MP}$	e	$(DR)_{MP}$
2.476	0.800	2.753	0.800	10.184	0.800
4.001	0.774	3.000	0.790	12.252	0.784
6.000	0.731	4.118	0.777	16.000	0.746
10.000	0.805	6.000	0.734	20.000	0.769
20.000	0.890	10.000	0.806	30.000	0.827
30.000	0.923	20.000	0.891	45.000	0.882
		30.000	0.925		

Table 4.4. Dynamic Ratios for the (MPCL), Half-Sine Loading, Initial Half-Sine Shape, m = 2.

$I_1/I_2 = .9$		$I_1/I_2 = .4$		$I_1/I_2 = .001$	
e	$(DR)_{MP}$	e	$(DR)_{MP}$	e	$(DR)_{MP}$
2.476	0.800	2.753	0.800	10.184	0.800
4.001	0.774	3.000	0.790	12.252	0.784
6.000	0.731	4.118	0.777	16.000	0.746
10.000	0.805	6.000	0.734	20.000	0.769
20.000	0.890	10.000	0.806	30.000	0.827
30.000	0.923	20.000	0.891	45.000	0.882
		30.000	0.925		

Table 4.5. Dynamic Ratios for the (MPCL), Half-Sine Loading, Initial Half-Sine Shape, m = 3.

I_1/I_2 = .9		I_1/I_2 = .4		I_1/I_2 = .001	
e	$(DR)_{MP}$	e	$(DR)_{MP}$	e	$(DR)_{MP}$
2.476	0.808	2.700	0.800	4.268	0.799
3.000	0.795	3.000	0.788	5.000	0.784
4.000	0.793	4.040	0.777	5.136	0.784
6.000	0.732	6.000	0.736	6.000	0.747
10.000	0.806	10.000	0.809	8.000	0.750
20.000	0.891	20.000	0.893	10.000	0.794
30.000	0.925	30.000	0.926	20.000	0.883
				30.000	0.918

The respective zero-loading equilibrium points are given as follows:

i) for $e < \sqrt{16(\rho^{\frac{1}{2}}-1)^2\ \omega/\pi g_m \varphi}$ there exists no far equilibrium point. Hence, oscillations take place about the near stable static equilibrium point (e,0).

ii) for $e \geq \sqrt{-8\ (\rho^{\frac{1}{2}}-1)^2\ \psi/\pi g_m \varphi} < \sqrt{16\omega(\rho^{\frac{1}{2}}-1)^2/\pi g_m \varphi}$ there are five static equilibrium points as follows:

$$r_1 = e \qquad a_2 = 0 \qquad \text{(i)}$$

$$r_1 = \frac{\omega e}{\omega+2\psi} \qquad a_2 = \sqrt{\frac{\psi}{2}\left[\frac{4(\rho^{\frac{1}{2}}-1)^2}{\pi g_m \varphi} + \frac{2(\omega+4\psi)e^2}{(\omega+2\psi)^2}\right]} \qquad \text{(ii)}$$

$$r_1 = \frac{\omega e}{\omega+2\psi} \qquad a_2 = -\sqrt{\frac{\psi}{2}\left[\frac{4(\rho^{\frac{1}{2}}-1)^2}{\pi g_m \varphi} + \frac{2(\omega+4\psi)e^2}{(\omega+2\psi)^2}\right]} \qquad \text{(iii)} \qquad \Big\} (41)$$

$$r_1 = -\frac{e}{2} - \frac{1}{2}\sqrt{e^2 - 16(\rho^{\frac{1}{2}}-1)^2\omega/\pi g_m \varphi} \qquad a_2 = 0 \qquad \text{(iv)}$$

$$r_1 = -\frac{e}{2} + \frac{1}{2}\sqrt{e^2 - 16(\rho^{\frac{1}{2}}-1)^2\omega/\pi g_m \varphi} \qquad a_2 = 0 \qquad \text{(v)}$$

The corresponding expressions for the zero-loading total potentials are

$$
\left.
\begin{aligned}
U_T &= 0 && \text{point i} \\
U_T &= -\frac{16\gamma^2(\rho^{\frac{1}{2}}-1)^2}{\pi h_m}\left[\frac{4(\rho^{\frac{1}{2}}-1)^2}{\pi g_m \varphi}+\frac{2e^2}{\omega+2\gamma}\right] && \text{points ii, iii} \\
U_T &= \frac{g_m\varphi}{8h_m}\left[3e+\sqrt{e^2-16\omega(\rho^{\frac{1}{2}}-1)^2/\pi g_m\varphi}\right]\left[e^2\right. \\
&\qquad \left. -e\sqrt{e^2-16\omega(\rho^{\frac{1}{2}}-1)^2/g_m\pi\varphi+8\omega(\rho^{\frac{1}{2}}-1)^2/\pi g_m\varphi}\right] && \text{point iv} \\
U_T &= \frac{g_m\varphi}{8h_m}\left[3e-\sqrt{e^2-16\omega(\rho^{\frac{1}{2}}-1)^2/\pi g_m\varphi}\right]\left[e^2\right. \\
&\qquad \left. +e\sqrt{e^2-16\omega(\rho^{\frac{1}{2}}-1)^2/g_m\pi\varphi+8\omega(\rho^{\frac{1}{2}}-1)^2/\pi g_m\varphi}\right] && \text{point v}
\end{aligned}
\right\} \quad (42)
$$

Since the initial kinetic energy is nonzero and applied symmetrically at the initial point (e,0), $U_T = 0$, the initial path is the symmetric mode, followed readily by the antisymmetric mode of deformation. One notes that the total potential is positive for points ii through v for all $e \geq \sqrt{16\omega(\rho^{\frac{1}{2}}-1)^2/\pi g_m\varphi}$, where the equilibrium point iv is stable (in the small) and points ii, iii and v are unstable (in the small). Therefore, snap-through is possible for all initial rise parameters in the above range.

As for the case of a loading of constant magnitude and infinite duration, a critical ideal impulse can only be bracketed between upper and lower bounds in accordance with the definition of the MGCI and the

MPCI. Since U_T is zero, then $T + U_T = T_i$. A critical condition is reached when $T = 0$ at the unstable static equilibrium point of lowest potential.

In order to find expressions for the critical impulse, one expresses the ideal impulse in terms of the initial kinetic energy. Denoting by IMP* the impulse per unit mass imparted into the arch by the loading one acquires $\text{IMP}^* \, dm = \left(\frac{\partial w}{\partial t}\right)_i dm$. Neglecting rotary and longitudinal inertia the initial kinetic energy-impulse relationship becomes

$$T_i = \left[4 g_m L^{2\left(\frac{1}{m} - 1\right)} / h_m\right] \left[4 I_1 (\rho^{\frac{1}{2}} - 1)^2 / \alpha L^2\right]^{\frac{1}{m}} C_{\frac{m}{\rho}} (\text{Imp})^2$$

where $\text{IMP}^* = \text{Imp}^* \cos (x - a - L/2) \frac{\pi}{L}$ for the half-sine loading,

$$\text{Imp}^* = \sqrt{P_E \epsilon_E / \sigma A_u} \; \text{Imp}$$

and $C_{\frac{m}{\rho}}$ is a numerical integration constant given as (see Table 4.6)

$$C_{\frac{m}{\rho}} = \left[1/L^{(1+2/m)}\right] \left[\int_a^{a + \frac{L}{2}} x^{\frac{2}{m}} \cos^2\left(x - a - \frac{L}{2}\right)\frac{\pi}{L} \, dx\right]$$

Thus, by relating the initial kinetic energy to the ideal impulse, conservation of mechanical energy yields the following expressions for critical impulses for m = 1, 2 and 3, respectively: (See Figure 4.14 through Figure 4.16)

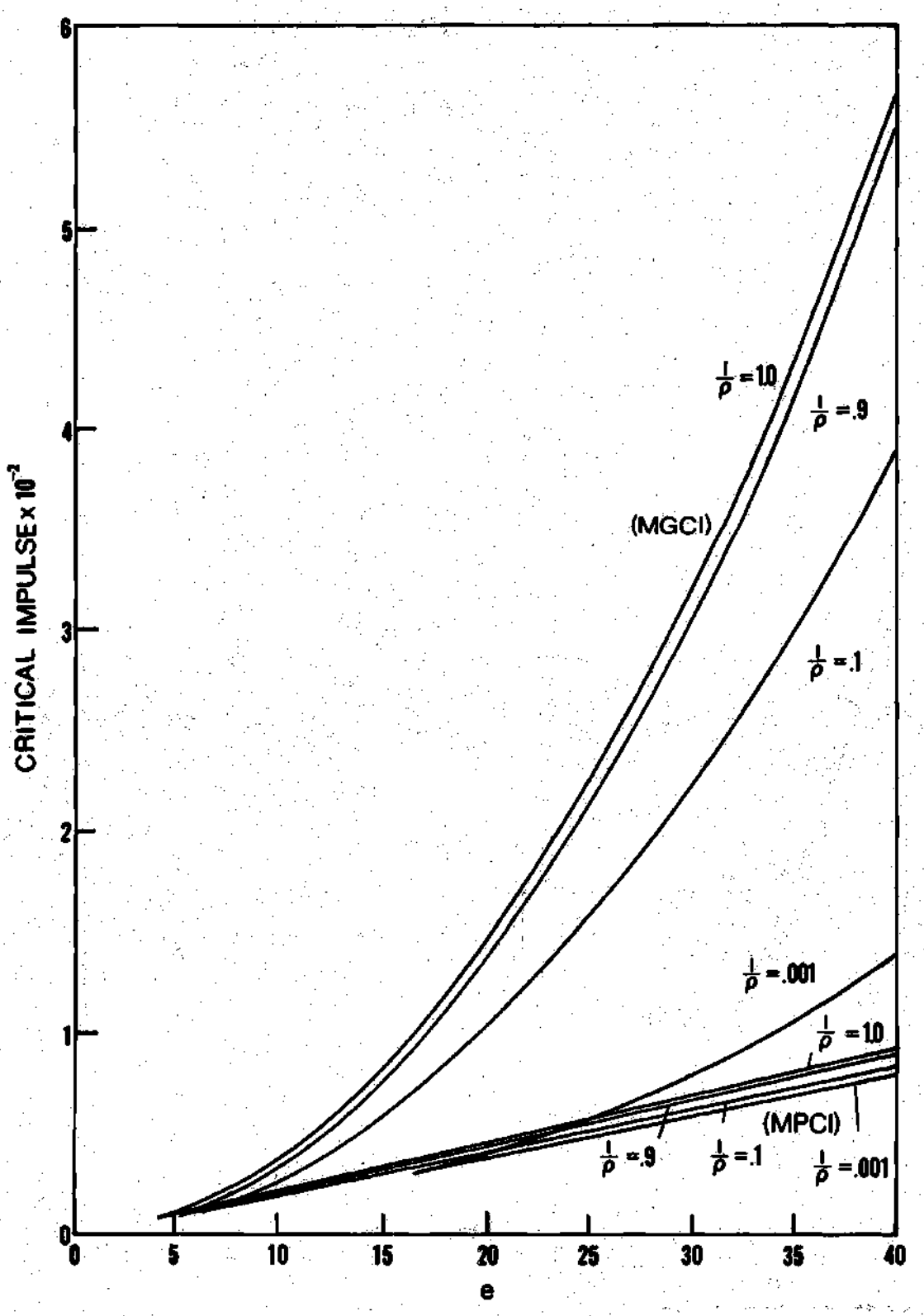

Figure 4.14 Nondimensional Critical Impulse versus Initial Rise Parameters, m = 1.

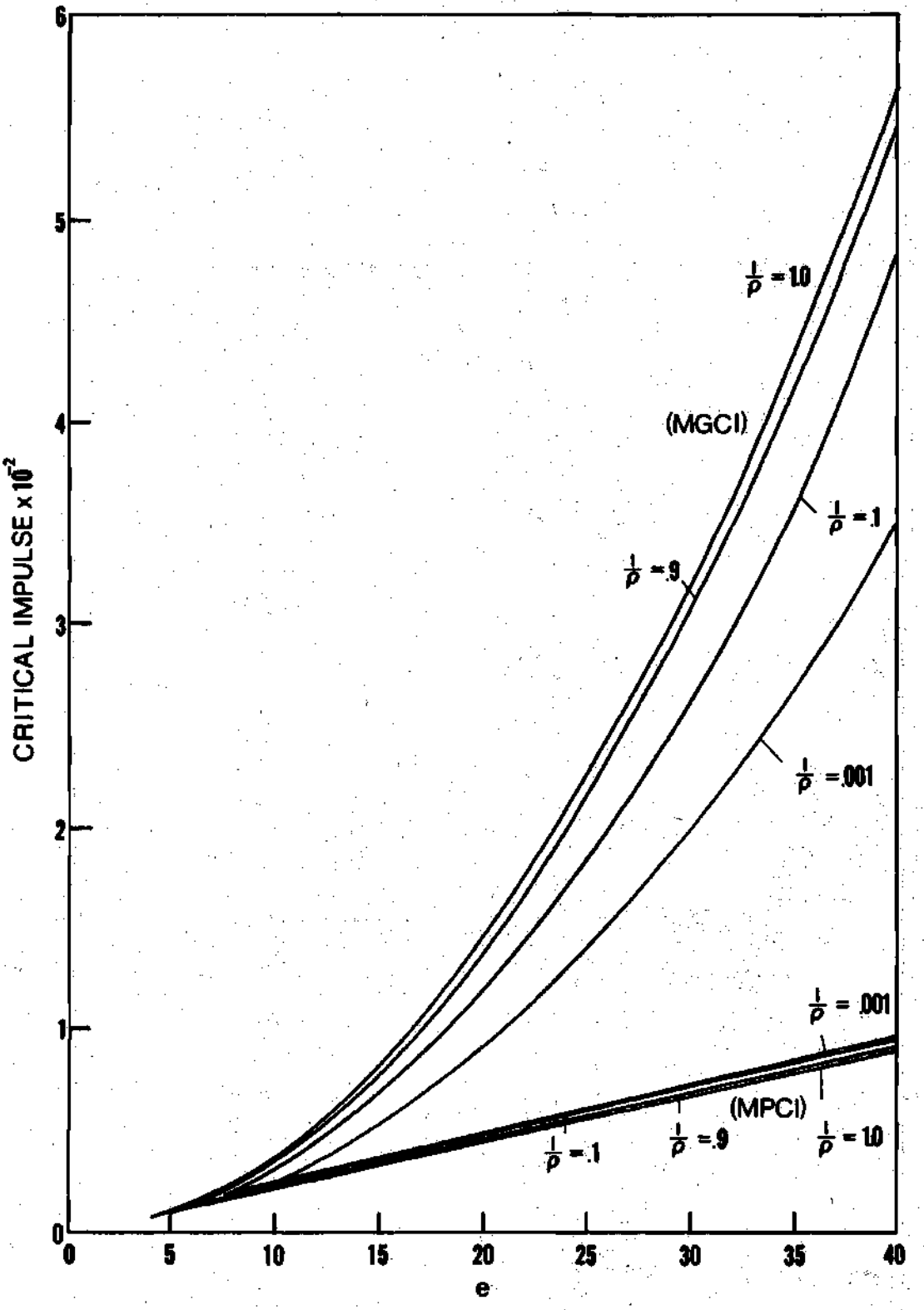

Figure 4.15 Nondimensional Critical Impulse versus Initial Rise Parameters, m = 2.

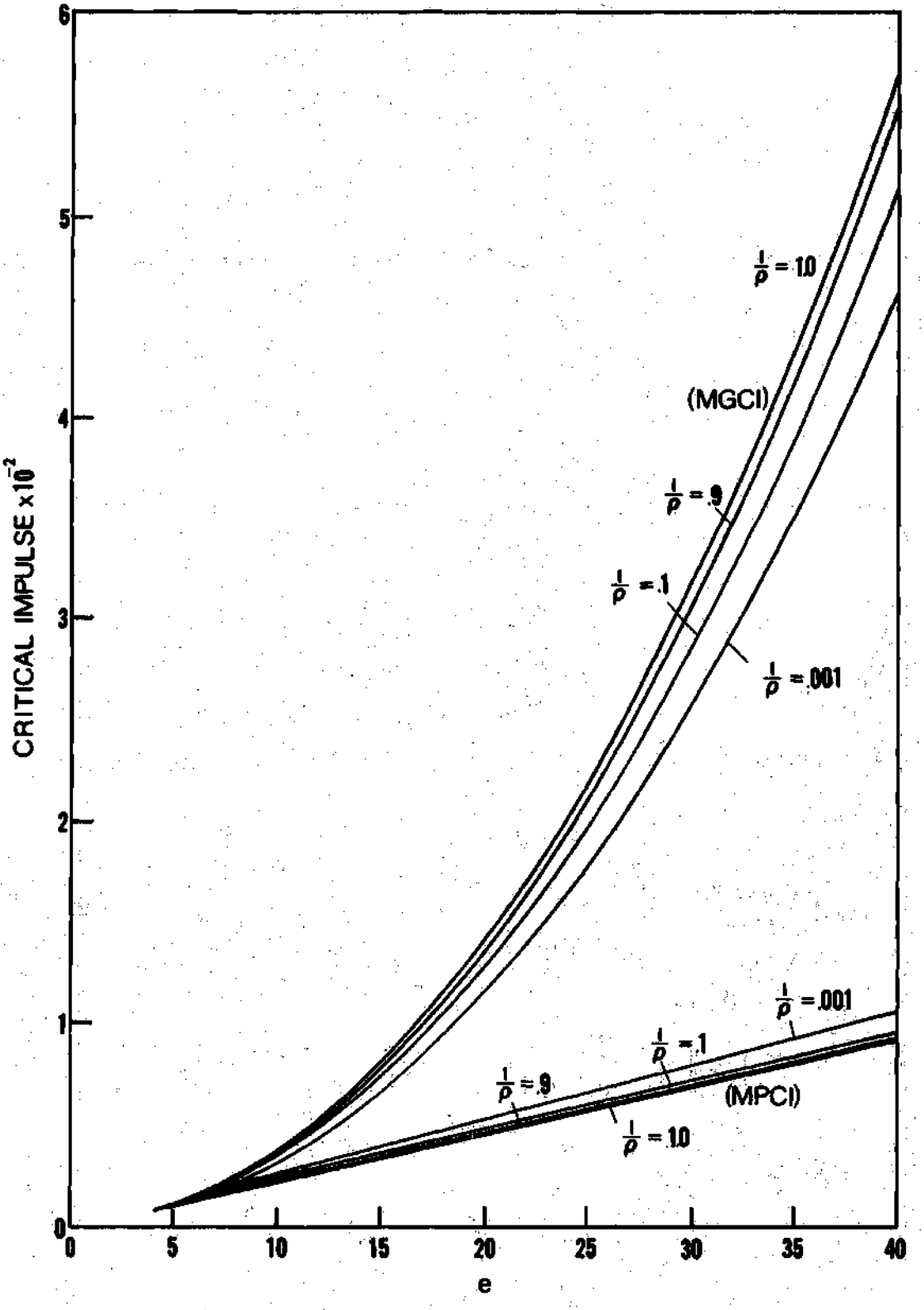

Figure 4.16 Nondimensional Critical Impulse versus Initial Rise Parameters, m = 3.

$$MPCI = \frac{-1}{C_{\frac{1}{2}}^{\frac{1}{2}}} \left(\frac{2}{\pi}\right)^{\frac{1}{2}} \psi\left[-\frac{(e)^2}{\omega+2\psi} - \frac{16(\rho^{\frac{1}{2}}-1)^2}{\pi\rho^{\frac{1}{2}}}\right]^{\frac{1}{2}}, \quad m = 1$$

$$MPCI = \frac{-1}{C_{\frac{1}{2}}^{\frac{1}{2}}} \left(\frac{2}{\pi}\right)^{\frac{1}{2}} 2\psi \frac{(\rho^{\frac{1}{2}}-1)}{(\rho-1)^{\frac{1}{2}}}\left[-\frac{(e)^2}{\omega+2\psi} - \frac{32(\rho^{\frac{1}{2}}-1)^2 \ln\rho^{\frac{1}{2}}}{\pi(\rho-1)}\right]^{\frac{1}{2}}, \quad m = 2$$

$$MPCI = \frac{-1}{C_{\frac{1}{2}}^{\frac{1}{2}}} \left(\frac{2}{\pi}\right)^{\frac{1}{2}} \frac{2^{\frac{2}{3}}5}{3} \psi \frac{(\rho^{\frac{1}{2}}-1)^{\frac{5}{3}}}{(\rho^{\frac{1}{6}}-1)}\left[-\frac{(e)^2}{\omega+2\psi} - \frac{400(\rho^{\frac{1}{6}}-1)(\rho^{\frac{1}{2}}-1)^3}{3\pi(\rho^{\frac{1}{6}}-1)^2}\right]^{\frac{1}{2}}, \quad m = 3$$

$$MGCI = \frac{1}{C_{\frac{1}{2}}^{\frac{1}{2}}} \frac{\rho^{\frac{1}{4}}}{32(\rho^{\frac{1}{2}}-1)}\left[3e - \sqrt{(e)^2 - \frac{(8)(16)\psi(\rho^{\frac{1}{2}}-1)^2}{\pi\rho^{\frac{1}{2}}}}\right]\left[(e)^2\right.$$

$$\left. + e\sqrt{(e)^2 - \frac{(8)(16)\psi(\rho^{\frac{1}{2}}-1)^2}{\pi\rho^{\frac{1}{2}}} + \frac{64\psi(\rho^{\frac{1}{2}}-1)^2}{\pi\rho^{\frac{1}{2}}}}\right]^{\frac{1}{2}}, \quad m = 1$$

$$MGCI = \frac{1}{C_{\frac{1}{2}}^{\frac{1}{2}}} \frac{1}{2^{\frac{1}{2}}(16)(\ln\rho^{\frac{1}{2}})^{\frac{1}{2}}}\left[3e - \sqrt{(e)^2 - \frac{(16)^2\psi(\rho^{\frac{1}{2}}-1)^2\ln\rho^{\frac{1}{2}}}{\pi(\rho-1)}}\right]\left[(e)^2\right.$$

$$+ e\sqrt{(e)^2 - \frac{(16)^2\psi(\rho^{\frac{1}{2}}-1)^2\ell n\rho^{\frac{1}{2}}}{\pi(\rho-1)} + \frac{(16)(8)\psi(\rho^{\frac{1}{2}}-1)^2\ell n\rho^{\frac{1}{2}}}{\pi(\rho-1)}}\Bigg]^{\frac{1}{2}}, \quad m = 2$$

$$\text{MGCI} = \frac{1}{c_{\rho}^{\frac{1}{2}}} \frac{3^{\frac{1}{2}}(\rho^{\frac{1}{2}}-1)^{\frac{1}{6}}}{2^{\frac{1}{3}}(48)(\rho^{\frac{1}{6}}-1)^{\frac{1}{2}}} \Bigg[3e - \sqrt{(e)^2 - \frac{(16)(8)(25)\psi(\rho^{\frac{1}{2}}-1)^3(\rho^{\frac{1}{6}}-1)}{3\pi(\rho^{\frac{5}{6}}-1)^2}}\Bigg](e)^2$$

$$+ e\sqrt{(e)^2 - \frac{(16)(8)(25)\psi(\rho^{\frac{1}{2}}-1)^3(\rho^{\frac{1}{6}}-1)}{3\pi(\rho^{\frac{5}{6}}-1)^2}}$$

$$+ \frac{(25)(64)(\rho^{\frac{1}{2}}-1)^3\psi(\rho^{\frac{1}{6}}-1)}{3\pi(\rho^{\frac{5}{6}}-1)^2}\Bigg]^{\frac{1}{2}}, \quad m = 3$$

4.3c Load of Constant Magnitude and Finite Duration

For this case of constant load and finite duration, snapping is possible for initial rise parameters for which the zero load total potential surface possesses five static equilibrium points (case ii of section 4.3b). Therefore, $e > \sqrt{16(\rho^{\frac{1}{2}}-1)^2\omega/\pi g_m\varphi}$.

To determine the critical load, $q_{1_{cr}}$, and corresponding critical impulse, $q_{1_{cr}} T_o$, one again considers conservation of mechanical energy. This yields

$$U_T^q + T^q = \text{Constant} = 0 \tag{43}$$

for the loaded arch with zero initial potential and velocity. If at

T_o the system is at position (r_{10}, a_{20}), the kinetic energy is $-U_T^q(r_{10}, a_{20})$ because of Equation 43. Also, at T_o, the loading vanishes and

$$U_T^o + T^o = \text{Constant} = U_T^o(r_{10}, a_{20}) + T^o(r_{10}, a_{20}) \tag{44}$$

From physical considerations and Equation 43 one obtains

$$T^o(r_{10}, a_{20}) = T^q(r_{10}, a_{20}) = - U_T^q(r_{10}, a_{20})$$

Therefore, Equation 44 yields

$$U_T^o + T^o = U_T^o(r_{10}, a_{20}) - U_T^q(r_{10}, a_{20}) \tag{45}$$

A critical condition exists when the zero-load saddle point (r_{1S}, a_{2S}) is reached with zero velocity. Thus,

$$U_T^o(r_{1S}, a_{2S}) = U_T^o(r_{10}, a_{20}) - U_T^q(r_{10}, a_{20}).$$

Use of Equations 26 and 42 (points ii or iii) yields an expression that relates the critical load to the release position r_{10} for any structural geometry.

$$q_{1_{cr}}(r_{10}-e) = [16\psi^2(\rho^{\frac{1}{2}}-1)^2/\pi h_m][2(\rho^{\frac{1}{2}}-1)^2/\pi g_m\varphi + e^2/(\omega+2\psi)] \tag{46}$$

In Equation 46 the unknowns are r_{10}, $q_{1_{cr}}$. In addition to Equation 46 one assumes the equation of the path and an equation which comes from integration of the equation of motion along the path, which is approximately given by the following:

$$a_2 = 0,\ \sqrt{e^2 + 8\psi(\rho^{\frac{1}{2}}-1)^2/\pi g_m \varphi} \leq r_1 \leq e$$

$$r_1^2 + 4a_2^2 = e^2 + \frac{8\psi(\rho^{\frac{1}{2}}-1)^2}{\pi g_m \varphi},\quad \frac{\omega e}{\omega+2\psi} \leq r_1 < \sqrt{e^2 + 8\psi(\rho^{\frac{1}{2}}-1)^2/\pi g_m \varphi} \tag{47}$$

(See Figures 4.3, 4.4 and 4.17)

The above path is believed to be a good approximation to the path of steepest descent and shallowest ascent toward the zero load saddle point. For a given load and, $e > \sqrt{16(\rho^{\frac{1}{2}}-1)^2\omega/\pi g_m \varphi}$ the path of motion on the total potential surface can be examined. (See Figure 4.2.) For any load greater than or equal to the MGCL, the path of steepest descent and shallowest ascent is the same as the locus of quasi-static equilibrium positions (See Figure 3.5) since the MGCL is equal to the minimum load at which buckling can occur quasi-statically. (See Figure 4.2d). The range of loading magnitudes between the MPCL and the MGCL is only a small percentage of the over-all range. Since the critical conditions for these loadings are reached near the zero-load saddle point the difference in critical time, when using the path given by Equation 47 versus the path of steepest descent and shallowest ascent, will differ only slightly. This is true for non-uniform as well as uniform geometry. For $I_1/I_2 = 0.001$ the exact anti-symmetric path for the MPCL begins at $r_1 = 6.73$ for $e = 8$. The quasi-static equilibrium ellipse initiates at $r_1 = 6.15$. Both the MPCL and the MGCL paths intersec for non-uniform as well as uniform geometries. Also, as the initial rise parameter increases this discrepancy decreases considerably.

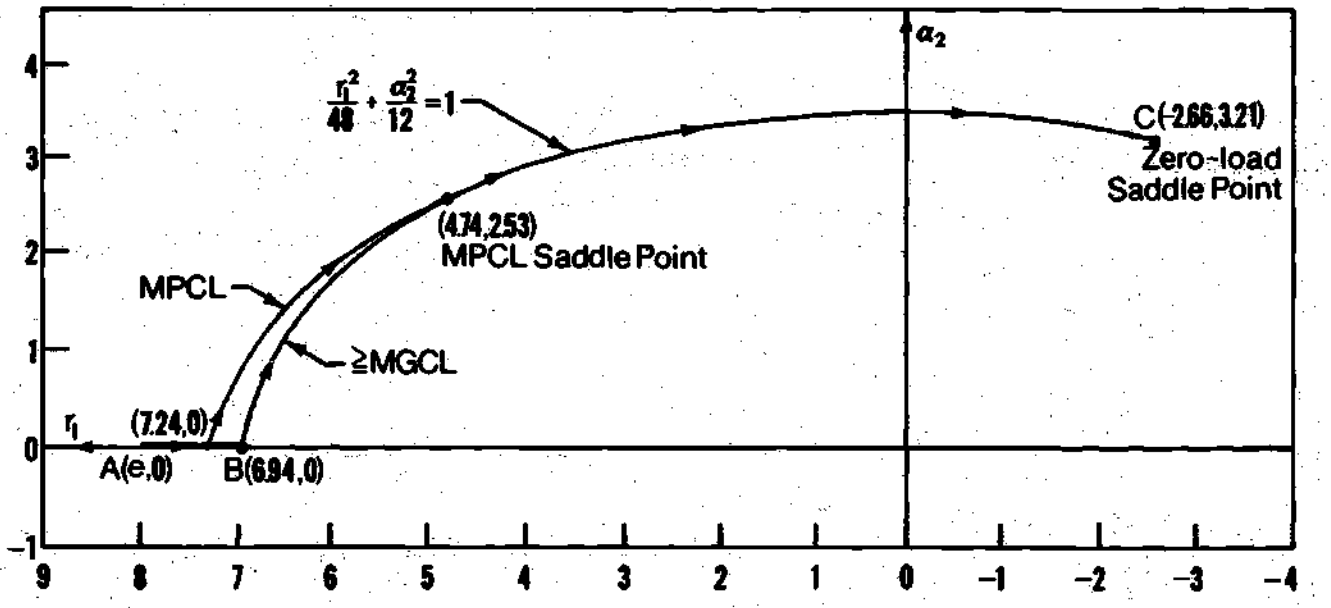

Figure 4.17 Possible Paths in the Configuration Space of the Generalized Coordinates for the Loading of Constant Magnitude and Finite Duration, $e = 8$, $\rho = 1.0$.

The equation of motion along the above path is found by Hamilton's principle with kinetic and potential energies expressed in terms of one independent generalized coordinate (r_1). If Equations 47 are differentiated with respect to time, one obtains

$$\begin{aligned} &\dot{a}_2 = 0 \ , \quad \sqrt{e^2 + 8\psi(\rho^{\frac{1}{2}}-1)^2/\pi g_m \varphi} \le r_1 \le e \\ &r_1\dot{r}_1 + 4a_2\dot{a}_2 = 0 \ , \quad \frac{\omega e}{\omega+2\psi} \le r_1 < \sqrt{e^2 + 8\psi(\rho^{\frac{1}{2}}-1)^2/\pi g_m \varphi} \end{aligned} \tag{48}$$

The coordinate a_2 is eliminated from the second of Equations 48. By using Equations 47. Thus,

$$r_1\dot{r}_1 = 4\dot{a}_2^2\left[e^2 + 8\psi(\rho^{\frac{1}{2}}-1)^2/\pi g_m\varphi - r_1^2\right]$$

The kinetic energy

$$T = (4g_m/h_m)[4I_1(\rho^{\frac{1}{2}}-1)/\alpha L^{2m}]^{\frac{1}{m}}\left[C_{\underline{m}}\dot{r}_1^2 + D_{\underline{m}}\dot{a}_2^2\right] ,$$

where $C_{\underline{m}}$ and $D_{\underline{m}}$ are numerical integration constants given in Tables 4.6 and 4.7, and the total potential, given by Equation 26, become

$$T = (4g_m/h_m)[4I_1(\rho^{\frac{1}{2}}-1)^2/\alpha L^{2m}]^{\frac{1}{m}} C_{\underline{m}}\dot{r}_1^2$$

$$U_T = (g_m\varphi/h_m)(r_1^2-e^2)^2 + [8(\rho^{\frac{1}{2}}-1)^2/\pi h_m](r_1-e)^2\omega + 2q_1(r_1-e)$$

for the AB portion of the path shown in Figure 4.17 and

Table 4.6. Numerical Integration Constants for the Ideal Impulse, $C_{\frac{m}{\rho}}$.

$C_{1/1.111}$	$C_{1/10}$	$C_{1/1000}$
23.0174	0.0875	0.0364
$C_{2/1.111}$	$C_{2/10}$	$C_{2/1000}$
2.3987	0.1456	0.0919
$C_{3/1.111}$	$C_{3/10}$	$C_{3/1000}$
1.12888	0.1737	0.1270

Table 4.7. Numerical Integration Constants for the Load of Constant Magnitude and Finite Duration, $D_{\frac{m}{p}}$.

$D_{1/1.111}$	$D_{1/10}$	$D_{1/1000}$
22.5333	0.0599	0.0198
$D_{2/1.111}$	$D_{2/10}$	$D_{2/1000}$
2.3734	0.1203	0.0666
$D_{3/1.111}$	$D_{3/10}$	$D_{3/1000}$
1.1209	0.1529	0.1020

$$T = [4g_m/h_m][4I_1(\rho^{\frac{1}{2}}-1)^2/\alpha L^{2m}]^{\frac{1}{m}} \dot{r}_1^2[C_{\underline{m}} + D_{\underline{m}} r_1^2/4(R_m-r_1^2)]$$

$$U_T = [64\psi^2(\rho^{\frac{1}{2}}-1)^4/\pi^2 g_m\varphi h_m] + [8(\rho^{\frac{1}{2}}-1)^2/\pi h_m][(r_1-e)^2\omega - 2\psi(R_m-r_1^2)]$$

$$+ 2q_1(r_1-e)$$

for the BC portion of the path. R_m is the square of the r_1 coordinate at point B in Figure 4.17 given by

$$R_m = e^2 + 8\psi(\rho^{\frac{1}{2}}-1)^2/\pi g_m\varphi \ .$$

As the arch becomes more uniform ($\rho \to 1$), the second term above reduces to 16.

With zero initial conditions the equation of motion along path AB reduces to the following:

$$\dot{r}_1 = -\sqrt{\left[\frac{h_m L^2 \alpha^{\frac{1}{m}}}{4^{(1+\frac{1}{m})} g_m C_{\underline{m}} I_1^{\frac{1}{m}} (\rho^{\frac{1}{2}}-1)^{\frac{2}{m}}}\right]\left[-(g_m\varphi/h_m)(r_1^2-e^2)^2\right.}$$

$$\left. - [8\omega(\rho^{\frac{1}{2}}-1)^2/\pi h_m](r_1-e)^2 + 2q_1(e-r_1)\right]$$

This yields the time to reach r_{10} along AB

$$\tau_1 = \sqrt{\frac{4^{\left(1+\frac{1}{m}\right)} g_m C_{\underline{m}}^{\frac{1}{m}} I_1^{\frac{1}{m}} (\rho^{\frac{1}{2}}-1)^{\frac{2}{m}}}{h_m L^2 \alpha^{\frac{1}{m}}}} \int_{r_{10}}^{e} \left\{ \frac{dr_1}{\sqrt{-(g_m\varphi/h_m)(r_1^2-e^2)^2 - [8\omega(\rho^{\frac{1}{2}}-1)^2/\pi h_m][r_1-e]^2 + 2q_{1_{cr}}(e-r_1)}} \right\} \quad (49)$$

and by assuming a value of r_{10} on AB ($e \leq r_{10} \leq \sqrt{R_m}$) one obtains a unique value for $q_{1_{cr}}$ from Equation 46. The critical impulse is then given by the product ($q_{1_{cr}} \tau_1$). By requiring continuity in speed at point B, the equation of motion along BC reduces to the following:

$$\dot{r}_1 = -\sqrt{\begin{aligned} &\{4\alpha^{\frac{1}{m}} L^2 (\rho^{\frac{1}{2}}-1)^2/[I_1 4(\rho^{\frac{1}{2}}-1)^2]^{\frac{1}{m}} \pi g_m\}\{2(\omega+2\Psi)(r_1^2-R_m) \\ &+ [(2q_{1_{cr}} \pi h_m/4(\rho^{\frac{1}{2}}-1)^2) - 4\omega e][r_1 - \sqrt{R_m}]\} \\ &- \{D_{\underline{m}} h_m L^2 \alpha^{\frac{1}{m}}/[4(\rho^{\frac{1}{2}}-1)^2]^{\frac{1}{m}} C_{\underline{m}} g_m I_1^{\frac{1}{m}}\}\{-64\Psi(\rho^{\frac{1}{2}}-1)^4/h_m \pi^2 g_m \varphi \\ &- [8\omega(\rho^{\frac{1}{2}}-1)^2/\pi h_m](e - \sqrt{R_m})^2 + 2q_{1_{cr}}(e - \sqrt{R_m})\} \end{aligned}}$$

continued

$$\Big/ \sqrt{\frac{4R_m \underset{\rho}{C_m} + (\underset{\rho}{D_m} - 4\underset{\rho}{C_m})r_1^2}{r_1^2 - R_m}}$$

which yields

$$\tau_2 = \int_{r_{10}}^{\sqrt{R_m}} \frac{\sqrt{\frac{4R_m \underset{\rho}{C_m} + (\underset{\rho}{D_m} - 4\underset{\rho}{C_m})r_1^2}{r_1^2 - R_m}}\, dr_1}{\sqrt{\begin{aligned} &\{4\alpha^{\frac{1}{m}} L^2(\rho^{\frac{1}{2}}-1)^2/[I_1 4(\rho^{\frac{1}{2}}-1)^2]^{\frac{1}{m}} \pi g_m\}\{2(\omega+2\psi)(r_1^2-R_m) \\ &+ [(2q_{1_{cr}} \pi h_m/4(\rho^{\frac{1}{2}}-1)^2 - 4\omega e][r_1 - \sqrt{R_m}]\} \\ &- \{\underset{\rho}{D_m} h_m L^2 \alpha^{\frac{1}{m}}/[4(\rho^{\frac{1}{2}}-1)^2]^{\frac{1}{m}} \underset{\rho}{C_m} g_m I_1^{\frac{1}{m}}\}\{-64\psi(\rho^{\frac{1}{2}}-1)^4/h_m \pi^2 g_m \varphi \\ &- [8\omega(\rho^{\frac{1}{2}}-1)^2/\pi h_m](e - \sqrt{R_m})^2 + 2q_{1_{cr}}(e - \sqrt{R_m})\} \end{aligned}}} \qquad (50)$$

and by assuming a value of r_{10} on BC $\left(\sqrt{R_m} < r_{10} \leq \frac{\omega e}{\omega+2\psi}\right)$ Equation 46 yields a unique value for $q_{1_{cr}}$. If r_{10} is less than the value at point C in Figure 4.17, τ_2 is calculated by integration from $[\omega e/(\omega+2\psi)]$ to $\sqrt{R_m}$ in Equation 50 where $[\omega e/(\omega+2\psi)]$ is r_{10} at the zero-load saddle point, point C, and $q_{1_{cr}} > q_c$ where $q_{1_{cr}}$ at point C is given by

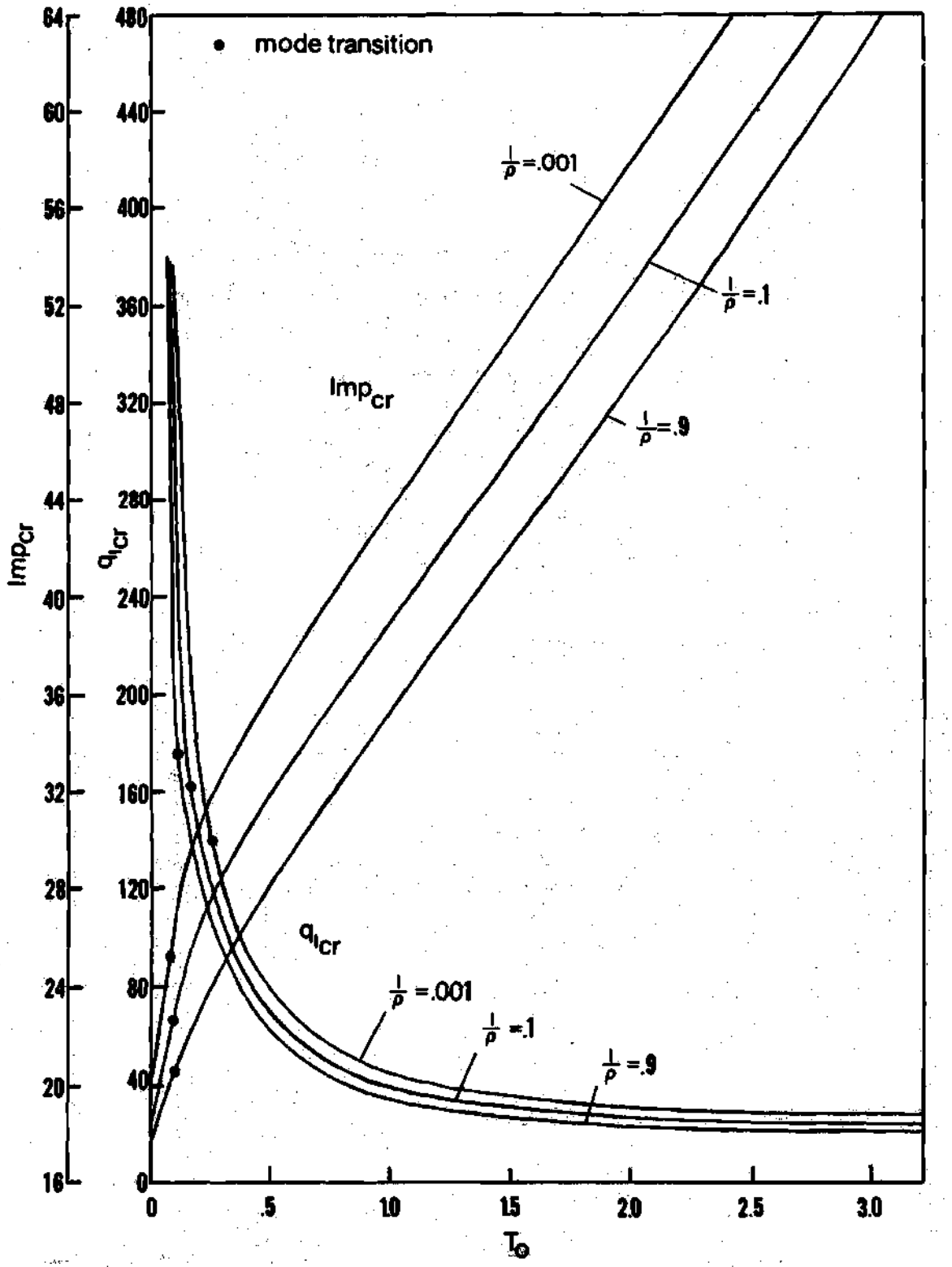

Figure 4.18 Critical Conditions for the Loading of Constant Magnitude and Finite Duration, e = 8, m = 3.

$$q_c = - [8\psi(\rho^{\frac{1}{2}}-1)^2/\pi h_m e][e^2 + 2(\rho^{\frac{1}{2}}-1)^2(\omega+2\psi)/\pi g_m \varphi] \quad .$$

The time to reach point B (τ_1) is determined from Equation 49 where the limits of integration are from A to B or e to $\sqrt{-8\psi(\rho^{\frac{1}{2}}-1)^2/\pi g_m \varphi}$, respectively. Finally, the time to reach r_{10} on BC is

$$T_o = \tau_1 + \tau_2$$

and the critical impulse at r_{10} is the product of the critical loading and the release time ($q_{1_{cr}} T_o$).

The calculations are carried out by a UNIVAC 1108 computer and are shown graphically in Figure 4.18 for e = 8 and m = 3.

4.4 Concluding Remarks

The previous results, for all three dynamic cases, are established for a complete range of initial rise parameters and nonuniformity parameters. The salient results are summarized by certain concluding remarks. First, the nonuniform geometry results approach those of the uniform geometry arch. See Refs. [6,29]. For m=1, the uniform arch carries the highest loadings and impulses for all initial rise parameters. For m=2, the load and impulse carrying capability is increased with increasing nonuniformity. This increase is approximately 10 per cent maximum increase for the loading of constant magnitude and infinite duration and the ideal impulse except for very low initial rise parameters in the case of the loading of constant magnitude and infinite duration. For m=3, critical loadings increase with

increasing nonuniformity. The maximum increase is approximately 30 per cent for the loading of constant magnitude and infinite duration and 20 per cent for the ideal impulse. For the loading of constant magnitude and finite duration it is noted that, for small release times, the load carrying capability is increased considerably over the uniform geometry arch, well above that realized for infinite time duration. It is obviously seen that for this case, m=3 is the best material configuration. Also, for the loading of constant magnitude and finite duration, as the critical release times approach zero the critical impulses approach the minimum possible critical impulse for $1/\rho = .9$, .1 and .001. As the critical release times become large, the critical loadings approach the minimum possible critical loadings for $1/\rho = .9$, .1 and .001. Finally, through this analysis it is demonstrated that for m=2 and 3 the optimum arch for minimum weight or maximum load carrying capability must correspond to some nonuniform distribution of stiffness.

CHAPTER V

OPTIMALITY CONDITIONS

5.1 Introduction

Optimization of structures and structural components is presently a wide field of interest. A host of diverse mechanical models are being investigated. The objective of optimal design varies depending on the mission requirements of the particular configuration. For a structural configuration the objective might be minimum cost, minimum weight, or maximum load carrying capability. Depending upon the presence and type of additional side requirements, such as some fixed geometric properties (size, shape, etc.) or limitations on stresses and deflections, it is possible that, by satisfying one objective, another one is also satisfied (i.e. duality between minimum weight and cost, etc.).

In any structural optimization problem one must clearly specify the design objective and the geometric and behavioral constraints. The geometric constraints are usually associated with space requirements such as lengths or areas. The behavioral constraints are associated with the response of the structure to the applied loadings. Limitations on maximum stress or maximum deflections are examples of behavioral constraints. All constraints can be classified as equality or inequality constraints. For certain constraints such as the shape of each structural element, the same problem must be investigated for

various values of the parameters such as changing the exponential value in the relation $I(x) = \alpha A^m(x)$ for the column, beam and the arch.

In this chapter it is intended to determine the conditions that must be satisfied in order to achieve a maximum strength design. The statement of the optimization problem is as follows: Given a shallow arch of specified volume, initial shape, and length find the distribution of stiffness such that the critical load (at snap-through) is a maximum. No attempt is made in this thesis to find the desired stiffness distribution.

5.2 Critical Conditions by Trefftz'[30] Criterion

Before it is possible to determine the conditions that lead to the optimum stiffness distribution, one must first obtain the objective function.

Since the objective in the optimization problem is maximization of the critical load (snap-through), the expression for the critical loading in terms of the structural geometry must be derived. This is accomplished by making use of the Trefftz criterion which is based on setting the first variation of the second variation of the total potential equal to zero (Refs. [31,32]). In order to obtain the expression for q_{cr}, one must first start with the total potential, then determine the first and second variations of the total potential with respect to the nondimensionalized displacements, and finally obtain the first variation of the second variation. The vanishing of the first variation of the total potential leads to the equilibrium equations and proper boundary conditions. Finally, the equilibrium equations and the stationary

(Euler-Lagrange equation) condition of the second variation are combined to obtain the expression for the objective function.

Letting $\eta(\xi) = \tilde{w}(\xi)$ and $u(\xi) = \tilde{u}(\xi)$ in Equation 20 for the total potential energy, one acquires

$$U_T[\tilde{u},\tilde{w}] = (1/2\pi)\left\{ \int_{\frac{\pi a}{L}}^{\frac{\pi}{L}(a+L)} [2\tilde{u} + (\tilde{w}')^2 - (\tilde{w}_o')^2]d\xi \right\}^2 / \int_{\frac{\pi a}{L}}^{\frac{\pi}{L}(a+L)} \frac{d\xi}{\bar{A}(\xi)}$$

$$+ (2/\pi) \int_{\frac{\pi a}{L}}^{\frac{\pi}{L}(a+L)} \bar{I}(\xi)[\tilde{w}'' - \tilde{w}_o'']^2 d\xi \qquad (53)$$

$$+ (4/\pi) \int_{\frac{\pi a}{L}}^{\frac{\pi}{L}(a+L)} q(\xi)[\tilde{w} - \tilde{w}_o]d\xi$$

where

$$\bar{I}(\xi) = \frac{I(\xi)}{I_u}, \quad \bar{A}(\xi) = \frac{A(\xi)}{A_u}, \quad (\ )' = \frac{d(\ )}{d\xi}$$

To acquire $\hat{U}_T[\tilde{u} + \epsilon_1\bar{\beta}(\xi), \tilde{w} + \epsilon_2\gamma(\xi)]$ now use $\hat{u} = \tilde{u} + \epsilon_1\bar{\beta}(\xi)$ and $\hat{w} = \tilde{w} + \epsilon_2\ \gamma(\xi)$ where $\hat{u}$ and $\hat{w}$ make up all possible functions to be considered and $\tilde{u}$ and $\tilde{w}$ are those particular $\hat{u}$ and $\hat{w}$ making U_T an extremum. Furthermore, $\gamma(\xi)$ and $\bar{\beta}(\xi)$ are admissible functions of ξ and ϵ_1 and ϵ_2 are as small as one chooses in order to stay chose to $\tilde{u}$ and $\tilde{w}$ i.e. to only get relative extremum. Thus,

$$\mathcal{V}_T[\tilde{u} + \epsilon_1\bar{\beta}(\xi), \tilde{w} + \epsilon_2\gamma(\xi)]$$

$$= \left(\frac{1}{2\pi}\right)\left\{\int_{\frac{\pi a}{L}}^{\frac{\pi(a+L)}{L}} \left[2(\tilde{u} + \epsilon_1\bar{\beta})' + (\tilde{w} + \epsilon_2\gamma)'^2 - (\tilde{w}_o')^2\right]d\xi\right\}^2 \Big/ \int_{\frac{\pi a}{L}}^{\frac{\pi}{L}(a+L)} \frac{d\xi}{\bar{A}(\xi)}$$

$$+ \left(\frac{2}{\pi}\right)\int_{\frac{\pi a}{L}}^{\frac{\pi}{L}(a+L)} \bar{I}(\xi)[(\tilde{w} + \epsilon_2\gamma)'' - \tilde{w}_o'']^2 d\xi$$

$$+ \left(\frac{4}{\pi}\right)\int_{\frac{\pi a}{L}}^{\frac{\pi}{L}(a+L)} q(\xi)(\tilde{w} + \epsilon_2\gamma - \tilde{w}_o)d\xi$$

$$= \left(\frac{1}{2\pi}\right)\left\{\int_{\frac{\pi a}{L}}^{\frac{\pi}{L}(a+L)} [2\tilde{u}' + (\tilde{w}')^2 - (\tilde{w}_o')^2]d\xi\right\}^2 \Big/ \int_{\frac{\pi a}{L}}^{\frac{\pi}{L}(a+L)} \frac{d\xi}{\bar{A}(\xi)}$$

$$+ \left(\frac{2}{\pi}\right)\int_{\frac{\pi a}{L}}^{\frac{\pi}{L}(a+L)} \bar{I}(\xi)[\tilde{w}'' - \tilde{w}_o'']^2 d\xi + \left(\frac{4}{\pi}\right)\int_{\frac{\pi a}{L}}^{\frac{\pi}{L}(a+L)} q(\xi)[\tilde{w} - \tilde{w}_o]d\xi$$

$$+ \left(\frac{2}{\pi}\right)\left\{\int_{\frac{\pi a}{L}}^{\frac{\pi}{L}(a+L)} [2\tilde{u}' + (\tilde{w}')^2 - (\tilde{w}_o')^2]d\xi\right\}\left\{\int_{\frac{\pi a}{L}}^{\frac{\pi}{L}(a+L)} \bar{\beta}'d\xi \Big/ \int_{\frac{\pi a}{L}}^{\frac{\pi}{L}(a+L)} \frac{d\xi}{\bar{A}(\xi)}\right\}\epsilon_1$$

$$+ \frac{4}{\pi}\left[\left\{\int_{\frac{\pi a}{L}}^{\frac{\pi}{L}(a+L)} \left[\bar{u}' + \frac{1}{2}(\tilde{w}')^2 - \frac{1}{2}(\tilde{w}_o')^2\right]d\xi\right\}\left\{\int_{\frac{\pi a}{L}}^{\frac{\pi}{L}(a+L)} \tilde{w}'\gamma'd\xi\right.\right.$$

$$\int_{\frac{\pi a}{L}}^{\frac{\pi}{L}(a+L)} \frac{d\xi}{\bar{A}(\xi)} \Bigg\} + \int_{\frac{\pi a}{L}}^{\frac{\pi}{L}(a+L)} \bar{I}(\xi)[\tilde{w}''' - \tilde{w}_o''']\gamma'' d\xi + \int_{\frac{\pi a}{L}}^{\frac{\pi}{L}(a+L)} q(\xi)\gamma d\xi \Bigg] \epsilon_2$$

$$+ \frac{4}{\pi}\Bigg[\Bigg\{\int_{\frac{\pi a}{L}}^{\frac{\pi}{L}(a+L)} \left[\bar{u}' + \tfrac{1}{2}(\tilde{w}')^2 - \tfrac{1}{2}(\tilde{w}_o')^2\right] d\xi\Bigg\}\Bigg\{\int_{\frac{\pi a}{L}}^{\frac{\pi}{L}(a+L)} (\gamma')^2 d\xi \Big/$$

$$\int_{\frac{\pi a}{L}}^{\frac{\pi}{L}(a+L)} \frac{d\xi}{\bar{A}(\xi)} \Bigg\} + \int_{\frac{\pi a}{L}}^{\frac{\pi}{L}(a+L)} \bar{I}(\xi)[\gamma'']^2 d\xi \Bigg] \epsilon_2^2$$

$$+ \frac{4}{\pi}\Bigg[\Bigg\{\int_{\frac{\pi a}{L}}^{\frac{\pi}{L}(a+L)} [\epsilon_1 \bar{\beta}' + \epsilon_2 \tilde{w}'\gamma'] d\xi\Bigg\}^2 \Big/ \int_{\frac{\pi a}{L}}^{\frac{\pi}{L}(a+L)} \frac{d\xi}{\bar{A}(\xi)}\Bigg] + \mathcal{O}(\epsilon_i^3) \qquad (54)$$

Define

$$\hat{U}_T - U_T \equiv \Delta U_T \equiv U_T^{(1)}[\tilde{w}, \gamma, \epsilon_2, \tilde{u}, \bar{\beta}, \epsilon_1] + U_T^{(2)}[\tilde{u}, \bar{\beta}, \epsilon_1^2, \tilde{w}, \gamma, \epsilon_2^2] + \mathcal{O}(\epsilon_i^3) \qquad (55)$$

where the superscripts (1,2,3) denote the order of the variation.

One can conclude that

$$U_T^{(1)} = \frac{4}{\pi}\Bigg\{\int_{\frac{\pi a}{L}}^{\frac{\pi}{L}(a+L)} \left[\tilde{u}' + \tfrac{1}{2}(\tilde{w}')^2 - \tfrac{1}{2}(\tilde{w}_o')^2\right] d\xi\Bigg\}$$

$$\cdot \Bigg\{\int_{\frac{\pi a}{L}}^{\frac{\pi}{L}(a+L)} \bar{\beta}'\, d\xi \Big/ \int_{\frac{\pi a}{L}}^{\frac{\pi}{L}(a+L)} \frac{d\xi}{\bar{A}(\xi)}\Bigg\} \epsilon_1$$

$$+\frac{4}{\pi}\left[\left\{\int_{\frac{\pi a}{L}}^{\frac{\pi}{L}(a+L)}\left[\tilde{u}' + \tfrac{1}{2}(\tilde{w}')^2 - \tfrac{1}{2}(\tilde{w}_o')^2\right]d\xi\right\}\left\{\int_{\frac{\pi a}{L}}^{\frac{\pi}{L}(a+L)} \tilde{w}'\gamma' d\xi\right/\right.$$

$$\left.\int_{\frac{\pi a}{L}}^{\frac{\pi}{L}(a+L)} \frac{d\xi}{\bar{A}(\xi)}\right\} + \int_{\frac{\pi a}{L}}^{\frac{\pi}{L}(a+L)} \bar{I}(\xi)[\tilde{w}'' - \tilde{w}_o'']\gamma'' d\xi \qquad \Big\} (56)$$

$$\left. + \int_{\frac{\pi a}{L}}^{\frac{\pi}{L}(a+L)} q(\xi)\gamma d\xi\right] e_2$$

$$U_T^{(2)} = \frac{4}{\pi}\left[\left\{\int_{\frac{\pi a}{L}}^{\frac{\pi}{L}(a+L)}\left[\tilde{u}' + \tfrac{1}{2}(\tilde{w}')^2 - \tfrac{1}{2}(\tilde{w}_o')^2\right]d\xi\right\}\left\{\int_{\frac{\pi a}{L}}^{\frac{\pi}{L}(a+L)} (\gamma')^2 d\xi\right/\right.$$

$$\left.\int_{\frac{\pi a}{L}}^{\frac{\pi}{L}(a+L)} \frac{d\xi}{\bar{A}(\xi)}\right\} + \int_{\frac{\pi a}{L}}^{\frac{\pi}{L}(a+L)} \bar{I}(\xi)[\gamma'']^2 d\xi \qquad \Big\} (57)$$

$$\left. \right] e_2^2$$

$$+\frac{4}{\pi}\left[\left\{\int_{\frac{\pi a}{L}}^{\frac{\pi}{L}(a+L)} [e_1\bar{\beta}' + e_2\tilde{w}'\gamma']d\xi\right\}^2 \Big/ \int_{\frac{\pi a}{L}}^{\frac{\pi}{L}(a+L)} \frac{d\xi}{\bar{A}(\xi)}\right]$$

By the principle of the stationary value of the total potential, equilibrium is characterized by the vanishing of the first variation $(U_T^{(1)})$.

Let

$$\bar{P} = -\int_{\frac{\pi a}{L}}^{\frac{\pi}{L}(a+L)} \left\{\frac{1}{2}\left[(\tilde{w}')^2 - (\tilde{w}_o')^2\right]\right\} d\xi \Big/ \int_{\frac{\pi a}{L}}^{\frac{\pi}{L}(a+L)} \frac{d\xi}{\bar{A}(\xi)}$$

where

$$\bar{P} = \frac{\left(\frac{L}{\rho}\right)^2 Q}{\pi^2 E A_u}, \qquad \rho^2 = I_u/A_u \qquad \text{and} \qquad \int_{\frac{\pi a}{L}}^{\frac{\pi}{L}(a+L)} \tilde{u}'\, d\xi = 0 .$$

Thus, integration by parts of $U_T^{(1)}$ yields

$$\left.\begin{aligned}
\left(\frac{\pi}{4}\right) U_T^{(1)}[\tilde{w}, \gamma, \epsilon_2, \tilde{u}, \bar{\beta}, \epsilon_1] = 0 = \epsilon_2 \int_{\frac{\pi a}{L}}^{\frac{\pi}{L}(a+L)} &\{[\bar{I}(\xi)(\tilde{w}''-\tilde{w}_o'')]'' \\
&+ [\bar{P}\tilde{w}']' + q(\xi)\}\gamma d\xi + \epsilon_1 \int_{\frac{\pi a}{L}}^{\frac{\pi}{L}(a+L)} \bar{P}'\bar{\beta} d\xi + \epsilon_1 \bar{P}\bar{\beta}\Big|_{\frac{\pi a}{L}}^{\frac{\pi}{L}(a+L)} \\
&+ \epsilon_2 \bar{I}(\xi)[\tilde{w}''-\tilde{w}_o'']\gamma'\Big|_{\frac{\pi a}{L}}^{\frac{\pi}{L}(a+L)} \\
&- \epsilon_2\{\bar{P}\,\tilde{w}' + [\bar{I}(\xi)(\tilde{w}''-\tilde{w}_o'')]'\}\gamma\Big|_{\frac{\pi a}{L}}^{\frac{\pi}{L}(a+L)}
\end{aligned}\right\} \qquad (58)$$

The above contains both the equilibrium equations and the associated

boundary conditions. The equilibrium equations and the associated boundary conditions become [in terms of $\eta(\xi)$ and $u(\xi)$]

$$
\left.
\begin{array}{ll}
\bar{P}' = 0 & \\
\left[\bar{I}(\xi)(\eta'' - \eta_o'')\right]'' + \bar{P}\,\eta'' + q(\xi) = 0 & \\
\text{and at } \xi = \frac{\pi a}{L} \text{ or } \frac{\pi(a+L)}{L} & \\
\qquad \text{either} & \qquad \text{or} \\
\bar{P} = 0 & u = 0 \\
\bar{I}(\xi)(\eta'' - \eta'') = 0 & \eta' = 0 \\
\left[\bar{I}(\xi)(\eta'' - \eta_o'')\right]' + \bar{P}\,\eta' = 0 & \eta = 0
\end{array}
\right\} \qquad (59)
$$

Next, the method of determining the stability or instability of the prebuckled configuration is considered. The fundamental state of equilibrium is stable, when the second variation is positive definite. Therefore, when the buckling load is reached, the second variation becomes positive semi-definite, and the minimum value of the second variation is zero for some non-zero virtual displacement. Trefftz [30] observed that for the second variation to possess a non-trivial minimum the first variation of the second variation must vanish for certain non-zero values of the virtual displacements. For convenience one forms a new functional $H[\tilde{w},\gamma]$ which is nothing more than $U_T^{(2)}$ with the elimination of $\bar{B}$ from the second variation due to immovable end supports.

$$\left(\frac{\pi}{4\epsilon_2^2}\right)H[\tilde{w},\gamma] = \int_{\frac{\pi a}{L}}^{\frac{\pi}{L}(a+L)} \left\{ \bar{I}(\xi)(\gamma'')^2 - \bar{P}(\gamma')^2 \right.$$

$$\left. + \tilde{w}'\left(\frac{\int_{\frac{\pi a}{L}}^{\frac{\pi}{L}(a+L)} \tilde{w}'\gamma' d\xi}{\int_{\frac{\pi a}{L}}^{\frac{\pi}{L}(a+L)} \frac{d\xi}{\bar{A}(\xi)}} \right)\gamma' \right\} d\xi \qquad (60)$$

Introducing $\hat{\gamma} = \gamma + \epsilon_3\theta$, as before, and defining $\hat{H} - H = H^{(1)} + H^{(2)}$ + higher order terms, one requires the vanishing of $H^{(1)}$ for the second variation to possess a nontrivial minimum.

$$\left(\frac{\pi}{4\epsilon_2^2}\right)H^{(1)} = \epsilon_3 \int_{\frac{\pi a}{L}}^{\frac{\pi}{L}(a+L)} \left\{ 2\bar{I}(\xi)\gamma''\theta'' - 2\bar{P}\gamma'\theta' + \tilde{w}'\left(\frac{\int_{\frac{\pi a}{L}}^{\frac{\pi}{L}(a+L)} \tilde{w}'\theta' d\xi}{\int_{\frac{\pi a}{L}}^{\frac{\pi}{L}(a+L)} \frac{d\xi}{\bar{A}(\xi)}} \right)\gamma' \right.$$

$$+\tilde{w}'\left(\frac{\int_{\frac{\pi a}{L}}^{\frac{\pi}{L}(a+L)}\tilde{w}'\gamma'd\xi}{\int_{\frac{\pi a}{L}}^{\frac{\pi}{L}(a+L)}\frac{d\xi}{\bar{A}(\xi)}}\right)\theta'\Bigg\}d\xi \qquad (61)$$

Integration by parts of the internal integrals, and setting $H^{(1)}$ equal to zero yields

$$0=\int_{\frac{\pi a}{L}}^{\frac{\pi}{L}(a+L)}\Bigg\{2\bar{I}\,\gamma''\theta''-2\bar{P}'\gamma'\theta'+\tilde{w}'\left(\frac{\tilde{w}'\theta\Big|_{\frac{\pi a}{L}}^{\frac{\pi}{L}(a+L)}-\int_{\frac{\pi a}{L}}^{\frac{\pi}{L}(a+L)}\tilde{w}''\theta d\xi}{\int_{\frac{\pi a}{L}}^{\frac{\pi}{L}(a+L)}\frac{d\xi}{A}}\right)\gamma'$$

$$+\tilde{w}'\left(\frac{\tilde{w}'\gamma\Big|_{\frac{\pi a}{L}}^{\frac{\pi}{L}(a+L)}-\int_{\frac{\pi a}{L}}^{\frac{\pi}{L}(a+L)}\tilde{w}''\gamma d\xi}{\int_{\frac{\pi a}{L}}^{\frac{\pi}{L}(a+L)}\frac{d\xi}{A}}\right)\theta'\Bigg\}d\xi$$

Due to kinematic boundary conditions, γ is zero at the arch ends. Hence, θ is zero there also. Thus, the above integral becomes

$$0=\int_{\frac{\pi a}{L}}^{\frac{\pi}{L}(a+L)}\Bigg\{2\bar{I}\gamma''\theta''-2\bar{P}\gamma'\theta'-\tilde{w}'\left(\frac{\int_{\frac{\pi a}{L}}^{\frac{\pi}{L}(a+L)}\tilde{w}''\theta d\xi}{\int_{\frac{\pi a}{L}}^{\frac{\pi}{L}(a+L)}\frac{d\xi}{A}}\right)\gamma'$$

$$- \tilde{w}' \left(\frac{\int_{\frac{\pi a}{L}}^{\frac{\pi}{L}(a+L)} \tilde{w}'' \gamma d\xi}{\int_{\frac{\pi a}{L}}^{\frac{\pi}{L}(a+L)} \frac{d\xi}{\bar{A}}} \right) \theta' \Bigg\} d\xi$$

Integration by parts again yields (with $\gamma = \theta = 0$ at the boundaries)

$$0 = 2\bar{I}\gamma''\theta' \Big|_{\frac{\pi a}{L}}^{\frac{\pi}{L}(a+L)}$$

$$+ \int_{\frac{\pi a}{L}}^{\frac{\pi}{L}(a+L)} \{2[\bar{I}\,\gamma'']'' + 2[\tilde{P}\gamma']'\}\theta d\xi$$

$$+ \int_{\frac{\pi a}{L}}^{\frac{\pi}{L}(a+L)} \left\{ \tilde{w}'' \left(\frac{\int_{\frac{\pi a}{L}}^{\frac{\pi}{L}(a+L)} \tilde{w}'' \theta d\xi}{\int_{\frac{\pi a}{L}}^{\frac{\pi}{L}(a+L)} \frac{d\xi}{\bar{A}}} \right) \gamma + \tilde{w}'' \left(\frac{\int_{\frac{\pi a}{L}}^{\frac{\pi}{L}(a+L)} \tilde{w}'' \gamma d\xi}{\int_{\frac{\pi a}{L}}^{\frac{\pi}{L}(a+L)} \frac{d\xi}{\bar{A}}} \right) \theta \right\} d\xi \quad (62)$$

Rearranging terms in the next to last integral one obtains the Euler-Lagrange equation and the associated boundary conditions for arbitrary variations [in terms of $\gamma(\xi)$ and $\eta(\xi)$]

$$[\bar{I}(\xi)(\gamma'')]'' + P\gamma'' + \eta''\frac{\int_{\frac{\pi a}{L}}^{\frac{\pi}{L}(a+L)} \eta''\gamma d\xi}{\int_{\frac{\pi a}{L}}^{\frac{\pi}{L}(a+L)} \frac{d\xi}{\bar{A}(\xi)}} = 0 \tag{63}$$

at $\xi = \frac{\pi a}{L}$ and $\frac{\pi(a+L)}{2}$

$$\left.\begin{array}{cc} \text{either} & \text{or} \\ \bar{I}(\xi)\gamma'' = 0 & \gamma' = 0 \\ & \text{and } \gamma = 0 \end{array}\right\} \tag{64}$$

Through this approach it is clear that the bifurcation or limit point critical load and corresponding primary path (symmetric response) positions are established through the simultaneous solution of Equations 59 and 63 subject to their respective boundary conditions.

It is observed that for the case of limit point stability (top-of-the-knee buckling) one may assume that $\gamma(\xi) = c\eta(\xi)$, where c is an arbitrary small constant, provided that $\eta(\xi) = e \sin \xi$, and combine the two governing equations, Equations 59 and 63, into one. First, Equation 63 becomes

$$[\bar{I}(\xi)\eta'']'' + \bar{P}\eta'' + \eta'' \frac{\int_{\frac{\pi a}{L}}^{\frac{\pi}{L}(a+L)} \eta''\eta d\xi}{\int_{\frac{\pi a}{L}}^{\frac{\pi}{L}(a+L)} \frac{d\xi}{\bar{A}(\xi)}} = 0 \qquad (65)$$

Next, subtraction of Equation 63 from Equation 65 yields

$$q_{cr}(\xi) = [\bar{I}(\xi)\eta_o'']'' + \eta'' \int_{\frac{\pi a}{L}}^{\frac{\pi}{L}(a+L)} \eta''\eta d\xi \Big/ \int_{\frac{\pi a}{L}}^{\frac{\pi}{L}(a+L)} \frac{d\xi}{\bar{A}(\xi)} \qquad (66)$$

This equation is used in the next section to formulate an optimality criterion against top-of-the-knee snap-through buckling.

5.4 Formulation of the Optimality Criterion

In order to maximize the critical loading for the constant volume equality constraint one must form an augmented functional containing the ancillary condition

$$\int_{\frac{\pi a}{L}}^{\frac{\pi}{L}(a+L)} \bar{A}(\xi)d\xi = \frac{\tilde{V}}{\pi}$$

Since $\bar{I}(\xi) = \bar{A}^m(\xi)$, the new augmented functional becomes (for the total order)

$$\lambda \equiv \int_{\frac{\pi a}{L}}^{\frac{\pi}{L}(a+L)} q_{cr}(\xi)d\xi - \lambda_1 \int_{\frac{\pi a}{L}}^{\frac{\pi}{L}(a+L)} [\bar{A}(\xi) - \tilde{V}]d\xi$$

or

$$\lambda = \int_{\frac{\pi a}{L}}^{\frac{\pi}{L}(a+L)} \left\{ [\bar{A}^m(\xi)\eta_o'']'' + \eta'' \left(\int_{\frac{\pi a}{L}}^{\frac{\pi}{L}(a+L)} \eta''\eta d\xi \Big/ \int_{\frac{\pi a}{L}}^{\frac{\pi}{L}(a+L)} \frac{d\xi}{\bar{A}(\xi)} \right) \right.$$

$$\left. - \lambda_1(\bar{A}(\xi) - \tilde{V}) \right\} d\xi \qquad (67)$$

where λ_1 is a Lagrange multiplier.

Extremization of λ with respect to $\bar{A}(\xi)$ leads to the optimality condition. Since $\hat{\bar{A}} \equiv \bar{A} + \epsilon\mu$ and

$$[\bar{A}^m(\xi)\eta_o'']'' = m(m-1)\bar{A}^{m-2}(\xi)\ \eta_o'' + 2m\ \bar{A}^{m-1}\ \eta_o''' + \bar{A}^m\ \eta_o'''' \qquad (68)$$

one acquires

$$\lambda^{(1)}[\bar{A}, \eta, \epsilon] = 0 = \epsilon \int_{\frac{\pi a}{L}}^{\frac{\pi}{L}(a+L)} \left\{ m\bar{A}^{(m-1)}\eta_o'''' + 2m(m-1)\bar{A}^{(m-2)}\ \eta_o''' \right.$$

$$+ m(m-1)(m-2)\bar{A}^{(m-3)}\ \eta_o'' + \eta'' \left(\int_{\frac{\pi a}{L}}^{\frac{\pi}{L}(a+L)} \eta''\eta d\xi \right) \left(\int_{\frac{\pi a}{L}}^{\frac{\pi}{L}(a+L)} \frac{d\xi}{\bar{A}^2} \right) /$$

$$\left. \left(\int_{\frac{\pi a}{L}}^{\frac{\pi}{L}(a+L)} \frac{d\xi}{\bar{A}} \right)^2 - \lambda_1 \right\} \mu(\xi)d\xi \qquad (69)$$

Assuming that the functional has an extremum joining the variable end points and since the functional has an extremum compared to all admissible functions, it certainly has an extremum for those admissible functions with a vanishing value at the end points, i.e. fixed end points. Therefore, the above function, $\bar{A}(\xi)$, is a solution to the Euler-Lagrange equation and the necessary condition, $\lambda^{(1)} = 0$, reduces to the vanishing of the associated boundary conditions. No associated boundary conditions exist for this problem since there are no first order functions of $\bar{A}(x)$ in λ. See Ref. [33] for further details. Thus one acquires the integrodifferential equation

$$m\bar{A}^{(m-1)}\eta_o''' + 2m(m-1)\bar{A}^{(m-2)}\eta_o''' + m(m-1)(m-2)\bar{A}^{(m-3)}\eta_o''$$

$$+ \eta'\left(\int_{\frac{\pi a}{L}}^{\frac{\pi}{L}(a+L)} \eta''\eta d\xi\right)\left(\int_{\frac{\pi a}{L}}^{\frac{\pi}{L}(a+L)} \frac{d\xi}{\bar{A}^2}\right) \Big/ \left(\int_{\frac{\pi a}{L}}^{\frac{\pi}{L}(a+L)} \frac{d\xi}{\bar{A}}\right)^2 = \lambda_1 \tag{70}$$

as the optimality condition, where λ_1 is a constant. This equation is only valid where $\bar{A}(\xi)$ is not prescribed. A constraint such as

$$\int_{\frac{\pi a}{L}}^{\frac{\pi}{L}(a+L)} \lambda_2(\xi)[\bar{A}(\xi) - (A_o + p^2(\xi))]d\xi$$

could have been used to facilitate the task of preventing the cross-sectional area from becoming smaller than an allowable minimum A_o.

An optimum design is achieved by satisfying the equilibrium

equation simultaneously with the optimality condition subject to the constant volume constraint. One possible approach is the finite element displacement method used successfully for the column in Ref. [20].

CHAPTER VI

CONCLUDING REMARKS AND RECOMMENDATIONS

Representation of deflections of the low arch by both symmetric and antisymmetric modes is shown to be very accurate by comparisons with the exact solution whenever possible and by comparing the limiting value of nonuniform geometry ($1/\rho \to 1$) to that achieved for uniform geometry. It is shown that, as for the uniform geometry case, the mode of buckling is symmetric for a low range of initial rise parameters. For higher initial rise parameters, which consist of the largest percentage, the antisymmetric mode governs. Furthermore, if only the symmetric mode is considered the analysis overpredicts the buckling loads and impulses for sufficiently high initial rise parameters. It is seen that snap-through is possible for dynamic and quasi-static loadings depending on the nonuniformity and the initial rise parameter. Furthermore, critical dynamic loadings and impulses are bracketed between upper and lower bounds.

Overall, $m = 3$ yields the best material distribution of the cross-sectional area. For quasi-static loadings, $n = 2$ and $m = 3$ yield the highest critical loadings or the best weight savings corresponding to approximately 20 per cent for extreme nonuniform geometry. Thus, $n = 2$ is used to distribute the inertia for the dynamic cases considered. Geometry, for $m = 3$, shows approximately 20 per cent increase in impulse carrying capability for the ideal impulse and

approximately 30 per cent increase in load carrying capability for the loading of constant magnitude and infinite duration. For the loading of constant magnitude and finite duration, the load carrying capability is increased considerably, for small release times, well above that realized for the infinite time duration case.

The optimality criteria are shown to be quite nonlinear and no closed form solution seems possible. A possible solution might be obtained by the finite element displacement method as is illustrated in the literature for the optimum column.[20]

The optimality condition for bifurcation (asymmetric snap-through) instability should be formulated. The optimum shape against bifurcation buckling could be different than that corresponding to limit point instability. The optimum inertia shape is expected to be similar to that of the column problem.[21,22] Furthermore, the approach used herein to establish optimality criteria for the low arch exhibiting snap-through is believed to provide a method for future investigations of a general class of such structures.

The results obtained herein for m equals three are applicable to long shallow panels where the same applied loading is independent of the longitudinal direction and with the same boundary conditions along the straight edges. This is accomplished by using $E/(1-\nu^2)$ in place of Young's modulus, and considering the constant base as unity.

It is believed that studies for different boundary conditions will be important in selecting an optimum shape and in determining the effect on the critical buckling load. Investigations of geometric, material and loading imperfections are also worthy of consideration.

Antisymmetric geometric imperfections may cause a significant decrease in load carrying capability as well as an alteration of the optimum shape. Study of material inhomogenity and anisotropy, such as a laminated arch, is also recommended. Furthermore, the critical loadings and critical impulses for snap-through and the optimum shape may differ considerably for loadings applied antisymmetrically.

APPENDIX

SPECIALIZATION OF THE CRITICAL LOADING FOR UNIFORM STIFFNESS DISTRIBUTION

The uniform geometry shallow arch with pinned immovable ends and an initial half-sine shape under a half-sine quasi-static loading is now investigated. The complete series $\bar{\eta}(\xi) = \bar{\eta}_o + \sum_1^\infty a_n \sin n\xi$ is employed where $r_1 = a_1 + e$. Due to geometry and loading one requires the following:

$$\bar{\eta}_o = e \sin \xi$$

$$\bar{I}(\xi) = 1.0$$

$$\bar{A}(\xi) = 1.0$$

$$q_{cr} = q_{1_{cr}} \sin \xi$$

According to Equation 66 the expression for the critical loading becomes

$$q_{cr} = \bar{\eta}_o'''' + \bar{\eta}''' \int_{\frac{\pi a}{L}}^{\frac{\pi}{L}(a+L)} \bar{\eta}''' \bar{\eta} d\xi \Big/ \int_{\frac{\pi a}{L}}^{\frac{\pi}{L}(a+L)} d\xi$$

and substitution of the above series into q_{cr} leads to

$$q_{1_{cr}} \sin \xi = e \sin \xi + \frac{1}{\pi}\left(r_1 \sin \xi + \sum_2^\infty n^2 a_n \sin n\xi\right)\left[\int_{\frac{\pi a}{L}}^{\frac{\pi}{L}(a+L)} \left(r_1 \sin \xi + \sum_2^\infty n^2 a_n \sin n\xi\right)\left(r_1 \sin \xi + \sum_2^\infty a_n \sin n\xi\right) d\xi\right]$$

By performing the indicated integrations this expression becomes

$$q_{1_{cr}} \sin \xi = e \sin \xi + \frac{1}{2}\left[r_1^2 + \sum_2^\infty n^2 a_n^2\right]\left[r_1 \sin \xi + \sum_2^\infty n^2 a_n \sin n\xi\right]$$

Since each mode is independent the above equation is satisfied if the following set is satisfied.

$$q_{1_{cr}} = e + \frac{r_1}{2}\left[r_1^2 + \sum_2^\infty n^2 a_n^2\right] \qquad \text{(i)}$$

$$\left.\begin{aligned} 2\left[r_1^2 + \sum_2^\infty n^2 a_n^2\right] a_2 &= 0 \\ \left(\frac{2}{2}\right)\left[r_1^2 + \sum_2^\infty n^2 a_n^2\right] a_3 &= 0 \\ \vdots \quad \vdots \quad \vdots \quad \vdots \quad \vdots \end{aligned}\right\} \qquad \text{(ii)}$$

Equations ii imply that either all the a_i's (i=2,3,...) are zero or $(r_1^2 + n^2 a_n^2)$ vanishes. The only possible way that the latter can be true is for each independent mode to be zero which is trivial. Thus, all the generalized coordinates other than r_1 are zero, and the solution to i and ii is

$$q_{1_{cr}} = e + \frac{r_1^3}{2} \quad \text{or} \quad \mathfrak{T}_{cr} \equiv -\frac{r_1^3}{2} \qquad \text{(iii)}$$

and

$$a_n = 0 , \qquad n = 2,3,4,\cdots,\infty \tag{iii}$$

The solution for the critical buckling loading, for the limit point, is obtained by solving set (iii) with the two equilibrium equations (Ref. [6])

$$\frac{1}{4}(r_1^2 - e^2 + n^2 a_n^2) r_1 + r_1 = \bar{q} = e - q_1 \tag{iv}$$

Equation iv for symmetric snap-through ($a_n = 0$; limit point) becomes

$$\frac{1}{4}(r_1^2 - e^2) r_1 + r_1 = \bar{q} \tag{v}$$

Equation v and iii reduce to $r_1[4 - e^2 + 3r_1^2] = 0$. Since $r_1 \neq 0$, $r_{1_{cr}} = \sqrt{(e^2 - 4)/3}$. Thus

$$\bar{q}_{cr} = -\frac{1}{2}[(e^2 - 4)/3]^{3/2} \tag{vi}$$

for the limit point or top-of-the-knee buckling.

REFERENCES

1. Marguerre, K., "Die Durchschlagskraft eines Schwach Gekrummten Balken," Sitz Berlin Math. Gess., 37, 1938, p. 92.

2. Timoshenko, S. P., "Buckling of Curved Bars with Small Curvature," Journal of Appl. Mech., Vol. 2, 1935, p. 92.

3. Biezeno and Grammel, Engineering Dynamics, Vol. 2, "Elastic Problems of Single Machine Elements," 1956, pp. 369-411.

4. Kaplan, A. and Fung, Y. C., "Buckling of Low Arches or Curved Beams of Small Curvature," NACA TN 2840, Washington, 1952.

5. Gjelsvik, A., and Bodner, S. R., "The Energy Criterion and Snap Buckling of Arches," Journal of the Eng. Mech. Div., Proceedings of the ASCE, EM 5, 1962, p. 87.

6. Simitses, G. J., "Dynamic Snap-Through Buckling of Low Arches and Shallow Spherical Caps," Ph.D. Dissertation, Dept. of Aeronautics and Astronautics, Stanford University, June 1965.

7. Schreyer, H. L., and Masur, E. F., "Buckling of Shallow Arches," Journal of the Eng. Mech. Div., Proceedings of the ASCE, Vol. 92, 1966, p. 1.

8. Dickie, J. F. and Broughton, P., "Stability Criteria for Shallow Arches," Journal of the Eng. Mech. Div., Proceedings of the ASCE, June 1971, pp. 951-965.

9. Hsu, C. S., Kuo, C. T., and Lee, S. S., "On the Final States of Shallow Arches on Elastic Foundations Subjected to Dynamical Loads," Journal of Appl. Mech., Vol. 35, Series E, No. 4, Dec. 1968, pp. 713-723.

10. Hoff, N. J., and Bruce, V. G., "Dynamic Analysis of the Buckling of Laterally Loaded Flat Arches," Journal of Math. and Phys., Vol. XXXII, No. 4, Jan. 1954, pp. 276-288.

11. Lock, M. H., "Snapping of a Shallow Sinusoidal Arch Under a Step Pressure Load," AIAA, July, 1966, Vol. 4, No. 7, pp. 1249-1256.

12. Fulton, R. E. and Barton, F. W., "Dynamic Buckling of Shallow Arches," Journal of the Eng. Mech. Div., Proceedings of the ASCE, June 1971, pp. 865-876.

13a. Clausen, Bull. Phys.-Math. Acad, St. Petersburgh, Vol. 9, 1851, pp. 368-379.

13b. Nicolais, E. L., Bull. Polytech. Inst., St. Petersburgh, Vol. 8, 1907, p. 205.

13c. Blasius, H., Z. Math. u. Physik, Vol. 62, 1914, pp. 182-197.

14. Keller, J. B., "The Shape of the Strongest Column," Archive of Rational Mechanics and Analysis, Vol. 5, 1960, pp. 275-285.

15. Tadjbakhah, I. and Keller, J. B., "Strongest Columns and Isoperimetric Inequalities for Eigenvalues," Journal of Applied Mechanics, Vol. 29, 1962, pp. 159-164.

16. Keller, J. B., and Niordson, F. I., "The Tallest Column," Journal of Math. and Mech., Vol. 16, No. 5, 1966, pp. 433-445.

17. Taylor, J. E., "The Strongest Column: An Energy Approach," Journal of Appl. Mech., Vol. 34, No. 2, 1967, pp. 486-487.

18. Salinas, D., "On Variational Formulations for Optimal Structural Design," Ph.D. Dissertation, Univ. of California, Los Angeles, 1968.

19. Prager, W. and Taylor, J. E., "Problems of Optimal Structural Design," Journal of Appl. Mech., Vol. 35, 1968, pp. 102-106.

20. Simitses, G. J., Kamat, M. P. and Smith, C. V., "The Strongest Column by the Finite Element Method," AIAA, Vol. 11, No. 9, Sept. 1973, p. 1231; also AIAA Paper No. 72.141.

21. Wu, C. H., "The Strongest Circular Arch-A Perturbation Solution," Journal of Appl. Mech., Vol. 35, No. 3, Trans. ASME, Vol. 90, Series E, Sept. 1968, pp. 476-480.

22. Budiansky, B., Frauenthal, J. C. and Hutchinson, J. W., "On Optimal Arches," Journal of Appl. Mech., Vol. 36, 1969, pp. 880-882.

23. Niordson, F. I. and Pederson, P., "A Review of Optimal Structural Design," 13th International Congress of Theoretical and Applied Mechanics, Moscow, USSR, August 1972.

24. Wasiutynski, Z., and Brandt, A., "The Present State of Knowledge in the Field of Optimum Design of Structures," Applied Mech. Rev., Vol. 16, No. 5, 1963, pp. 341-350.

25. Sheu, C. Y. and Prager, W., "Recent Developments in Optimal Structural Design," Applied Mech. Rev., Vol. 21, No. 10, 1968, pp. 985-992.

26. Reissner, E., "On Transverse Vibrations of Thin Shallow Elastic Shells," Quarterly of Appl. Math., Vol. 13, 1965, pp. 169-176.

27. Sanders, J. L., "An Improved First Approximation Theory for Thin Shells," NASA, Technical Report R-24, 1959.

28. Timoshenko, S. P., and Gere, J. M., Theory of Elastic Stability, McGraw-Hill Book Co., Inc., New York, 1961, pp. 125-132.

29. Simitses, G. J., "Dynamic Snap-Through Buckling of Shallow Spherical Caps," Proceedings of the AIAA/ASME 7th Structures and Materials Conference, April 18-20, 1966, pp. 112-124. Also AIAA J., Vol. 5, p. 1019, 1967.

30. Trefftz, E., "Zur Theorie der Stabilitat des Elastischen Gleichgewichts," Zeitschrift fur Angewandte Mathematik und Mechanik, Vol. 13, 1933, pp. 160-165.

31. Dym, C. L. and Shames, I. H., Solid Mechanics: A Variational Approach, McGraw-Hill Book Co., Inc., New York, 1972.

32. Wempner, G., Mechanics of Solids, McGraw-Hill Book Co., Inc., New York, 1973.

33. Gelfand, I. M., and Fomin, S. V., Calculus of Variations, Prentice-Hall Book Co., Inc., Englewood Cliffs, N. J., 1963.

VITA

Ira Hammes Rapp was born in Charlotte, North Carolina, on April 12, 1948. He received his Bachelor's Degree in Civil Engineering, with honors, from The Citadel in June, 1970. He subsequently worked as a civil engineering consultant in Atlanta, Georgia, and later joined the Graduate Division of the Georgia Institute of Technology in the School of Engineering Science and Mechanics on an N.D.E.A. Fellowship. After receiving the Master's Degree in 1971, he was successful in attaining the John Hertz Fellowship for the remainder of his study towards the Doctor's Degree.